Insights of Mixing on the Assembly of DNA Nanoparticles

Manda S. Williams

A dissertation submitted in partial fulfillment
of the requirements for the degree of
Doctor of Philosophy

University of Washington
2013

Reading Committee

Paul Yager (Chair)
James Bryers
Xiaohu Gao

Program Authorized to Offer Degree: Bioengineering

University of Washington

Abstract

Insights of Mixing on the Assembly of DNA Nanoparticles

Manda S. Williams

Chair of the Supervisory Committee:

Paul Yager
Professor & Hunter & Dorothy Simpson Endowed Chair in Bioengineering

Department of Bioengineering

Size is a crucial parameter in the delivery of nanoparticle therapeutics, affecting mechanisms such as tissue delivery, clearance, and cellular uptake. The morphology of nanoparticles is dependent both upon chemistry and the physical process of assembly. Polyplexes, a major class of non-viral gene delivery vectors, are conventionally prepared by vortex mixing, resulting in non-uniform nanoparticles and poor reproducibility. Better understanding and control of the physical process of assembly, and mixing in particular, will produce polyplexes of a more uniform and reliable size, optimizing their efficiency for laboratory and clinical use.

"Mixing" is the reduction of length scale of a system to accelerate diffusion until a uniform concentration is achieved. Vortex mixing is poorly characterized and sensitive to protocols.

Microfluidic systems are notable for predictable fluid behavior, and are ideal for analyzing and controlling the physical interaction of reagents on the microscale, realm where mixing occurs. Several microdevices for the preparation of DNA polyplexes are explored here. Firstly, the staggered herringbone mixer, a chaotic advection micromixer, is used to observe the effects of mixing time on nanoparticle size. Next, a novel device to surround the reagent flows with a sheath of buffer, preventing interaction with the walls and confining the complexation to a zone of lower, less variable shear and residence time, is used to demonstrate the role of shear in nanoparticle assembly. Lastly, uneven diffusion between ion pairs produces a small separation of charge at fluid interfaces; this short-lived electric field has a significant impact on the transport of DNA over the time scales of mixing and complexation. The effects of common buffers on the transport of DNA are examined for possible applications to mixing and complexation. These three investigations demonstrate the importance of the physical process in polyplex assembly, and indicate several important considerations in the development of new protocols and devices.

Table of Contents

Abbreviations and Definitions

AFM	Atomic Force Microscopy
CD	Convection-Diffusion
CFD	Computational Fluid Dynamics
CV	Coefficient of Variation, $\mathrm{CV} = \sigma/\mu$
DLS	Dynamic Light Scattering
FEM	Finite Element Method
GHK	Goldman-Hodgkins-Katz equation
LJP	Liquid Junction Potential
NS	Navier-Stokes
N/P	ratio of PEI nitrogen to DNA phosphate
PDI	Polydispersity Index, $\mathrm{PDI} = \sigma^2/Z_D$
PDMS	Polydimethylsiloxane
PEI	Polyethylenimine
PEG	Polyethylene glycol
SFD	Sheath Flow Device
SHM	Staggered Herringbone Mixer
TEM	Transmission Electron Microscopy
oligo	A nucleic acid oligomer (< 100 bp)
erf	the error function
μ	mean
σ	standard deviation
υ	dynamic viscosity, 1 x 10^{-3} Pa·s for water
x	horizontal axis, orthogonal to primary flow (length, mm or m)
y	horizontal axis along mixer length, primary axis of flow (length, μm or m)
z	vertical axis, orthogonal to primary flow (length, μm or m)

u	linear flow rate along channel length (y, m/s)
v	linear flow rate across channel width (x, m/s)
w	channel width (along x axis, μm or m)
h	height of main channel (along z axis, exclusive of grooves, μm or m)
l	mixer length (along y axis), in cycles (SHM)
d	length per mixer cycle (SHM)
a	distance in the x-z plane, orthogonal to fluid interface
p(n=m)	probability that a variable, n, is equal to a value, m
P(n<m)	cumulative probability that a variable, n, is less than a value, m
δ	mean thickness of the fluid core (SFD, μm)
L	a characteristic length used for calculation of dimensionless groups (m)
L_d	diffusion length (m)
$\hat{L}_d$	mean diffusion length, $\hat{L}_d = \sqrt{2Dt}$ (m)
L_i	minimum distance from a fluid element to the interface (m)
t_{mix}	mixing time, CV ≤ 0.1 or I ≥ 0.9I_{max} (s)
t_{res}	residence time (s)
Re	Reynolds number, Re = $\frac{Lu\rho}{\nu}$, in which L = h
Pe	Péclet number, Pe = $\frac{Lu}{D}$, in which L = w/2 (SHM, T-sensor device), L = δ/2 (SFD)
Da	Damköhler number for a 2nd order reaction, relative to t_{mix}, Da = $\frac{kcL_d^2}{D}$

Table of Figures

Table of Equations

Background

Context

Nanomedicine

One of the fastest growing fields of the past two decades, nanotechnology, the study of matter only 1 nm – 250 nm in length scale, has significant potential in the field of medicine. The small size of nanoparticles (Figure 1) allows relatively fast transport, reactivity, and tissue access, and properties different from those of the bulk material. Current nanomedicine encompasses two major areas: diagnostics and therapeutics.

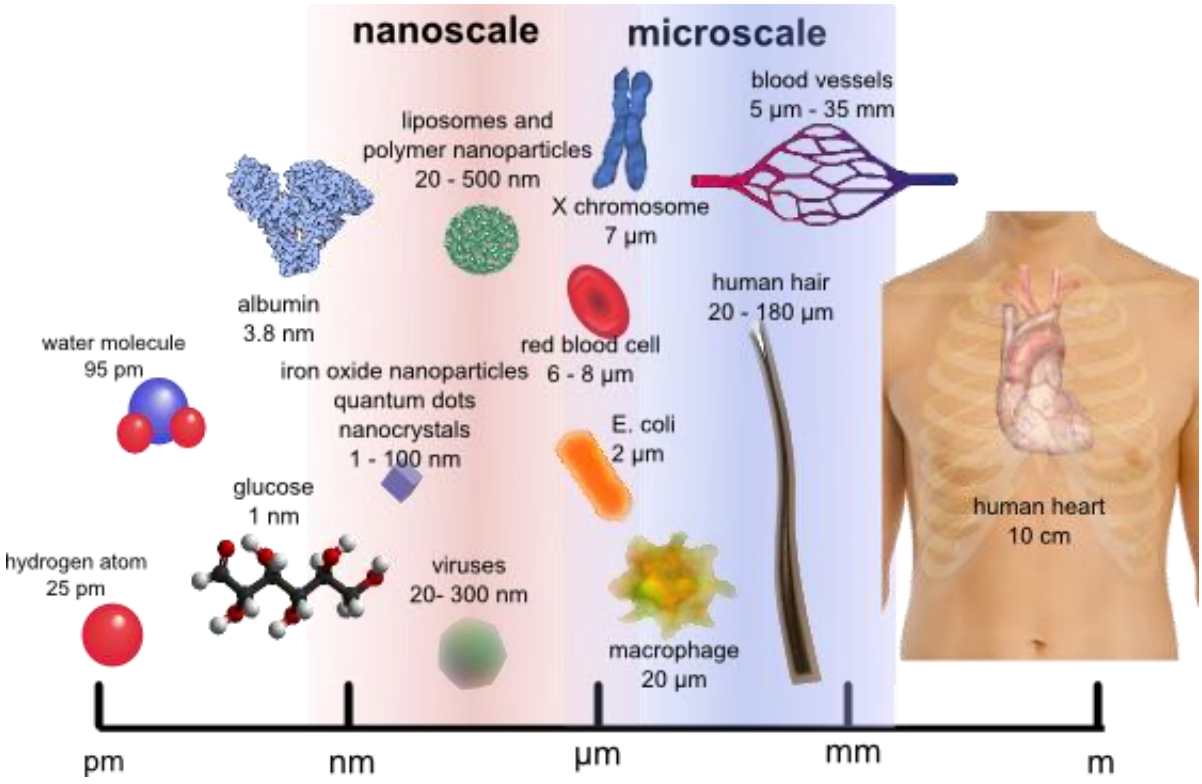

Figure 1: The relative scales of nanomedicine, chemistry, and biology. Objects are presented in approximate log scale. Portions of the figure were excerpted from the following sources [1-2]

Diagnostic nanoparticles for *in vivo* use, encompassing fluorescence and MRI contrast agents, utilize nanocrystals to enhance detection [3]. These collections of atoms are typically quite small, frequently only a few nm, though coated particles may be larger. Generally, such agents measure 1 – 100 nm in diameter. The arrangement of the atoms at the surface dominates the physics and chemistry, giving them unique properties. Quantum dots (QDs) are semiconductor nanocrystals with properties superior to conventional fluorophores: relatively broad absorption, but narrow emission, and no photobleaching, allowing longer imaging of multiple targets *in vivo* [4-6]. Colloidal gold nanoparticles can be used to observe molecular interactions via fluorescence quenching [7-8]. Superparamagnetic iron oxide nanoparticles are excellent contrast agents for magnetic resonance imaging (MRI) [9-10]. Because these nanoparticles are so small, they have excellent tissue access *in vivo*, and conjugation with a targeting group enables detection of, for example, cancer metastasis, and incorporation with a therapeutic nanocomplex would allow monitoring of the biodistribution of that agent.

While therapeutic nanoparticles include photosensitizers, radiosensitizers, and therapeutic ultrasound agents [11-12], the most common therapeutic nanoagents are typically vehicles carrying pharmaceutical payload, and they are usually larger than nanocrystals, but usually < 250 nm [3]. Many drugs have poor aqueous solubility, and encapsulating them in a carrier allows a greater effective dose to be delivered. Packaging therapeutic agents also protects them from degradation in the blood, and can reduce systemic toxicity. Furthermore, the circulation time can be increased, and the drugs can be released at a controlled rate or in response to their environment [13]. This in turn can lower the frequency of dosing and minimize systemic side effects by limiting delivery to a target tissue. Additionally, nanoparticles present an alternative vaccine strategy, by delivering

antigens directly to antigen-presenting macrophages [14]. As of 2013, 45 nanoparticle-based drugs had been approved by the FDA, with nearly 100 in trials; the majority of these drugs are either contained within liposomes or bound by polymers [15].

The pharmacokinetics of nanoparticles *in vivo* fundamentally differ from those of small molecules, with different transport properties, cellular associations, and clearance mechanisms (Figure 2). The specific interactions of nanoparticles *in vivo* are independent of the interior or function of the nanoparticle, but depend strongly upon surface chemistry, size, and shape. Though the agents may be delivered locally to the target tissue, that is not always possible, and systemic delivery presents several significant barriers.

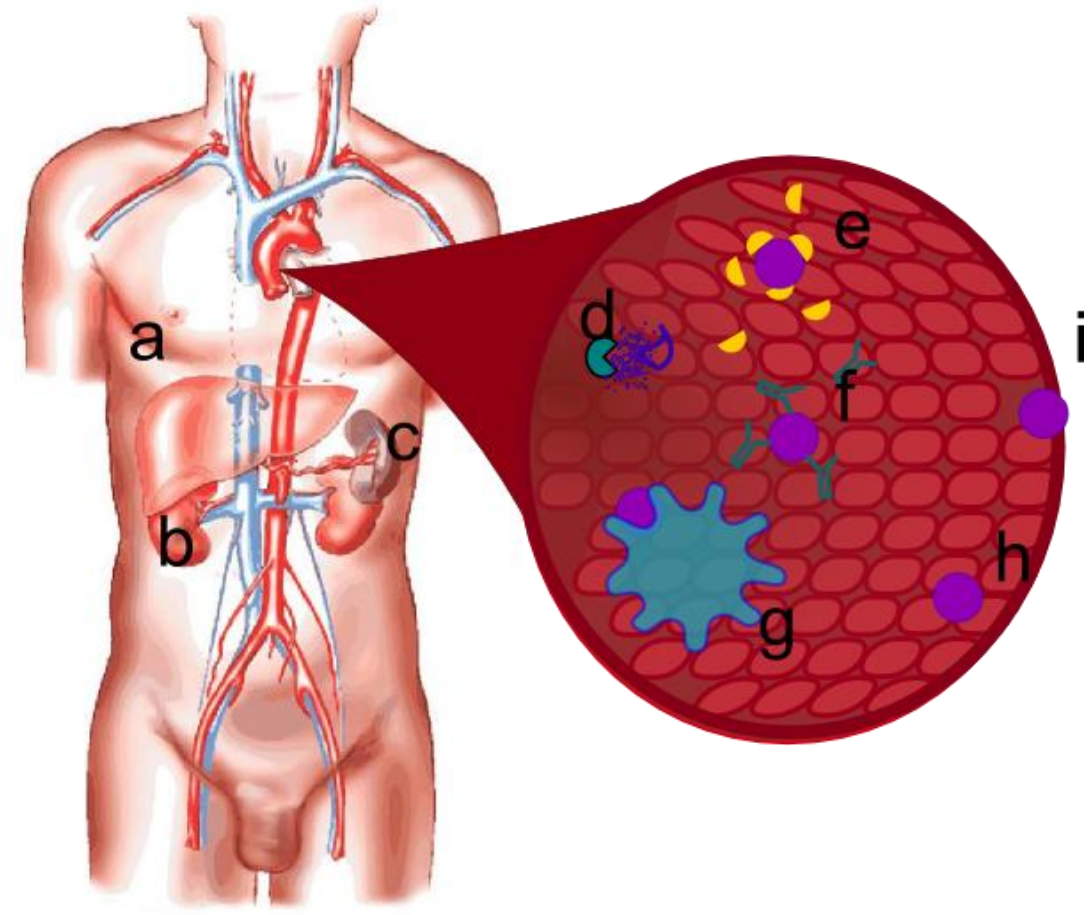

Figure 2: Systemic barriers to nanomedicine delivery. Systemic clearance occurs chiefly *via* the liver (a), kidneys (b), and spleen (c). Bare nucleic acids are readily degraded by serum nucleases (d). Nanoparticles are also removed from circulation by binding with serum proteins (e), leading to aggregation and clearance, opsonization by circulating antibodies (f), which facilitates removal by macrophages (g), and interactions with the endothelial surface (h). In order to reach target tissues from the vasculature, nanoparticles must escape through fenestrae (i).Vascular system diagram borrowed from another source [21].The primary organs to remove nanoparticles are the liver, spleen, and kidneys. In the liver, particles > 200 nm are most efficiently cleared by the Kupffer cells, while renal filtration is limited to particles < 8 nm; macrophages in the spleen remove a broad range of particle sizes, but phagocytosis is most rapid for particles < 200 nm [3, 16-17]. Buildup of non-biodegradable material in these organs is a major cause of nanoparticle toxicity [18]. Another major clearance mechanism is phagocytosis by the reticuloendothelial system (RES), accelerated by opsonization and nonspecific binding of blood proteins to the particles [19]. Serum contains more than 0.7 g/ml proteins, most of them negatively charged; however, significant adsorption still occurs on particles with negative zeta potentials, as well as those with positively charged and hydrophobic surfaces, though the both the rate and type of protein deposition differs [20].

Because this protein binding affects the ultimate size and surface properties of the nanoparticles, it also impacts biodistribution and clearance [20]. Furthermore, interactions with some proteins, such as fibrinogen, promote inflammation and contribute to the toxicity of the nanoparticles [22-23]. Polyethylene glycol (PEG) is a neutral, hydrophilic polymer known to significantly reduce nonspecific binding (Figure 3). PEG does not interact either electrostatically or hydrophobically with other species, and the polymer provides a steric hindrance to interactions with the material beneath [24]. Though antibodies to PEG have been reported, the effect seems to be dependent upon the chemical linkage, and PEG itself is regarded as non-immunogenic [25]. Modifying nanoparticles with PEG substantially reduces clearance by the liver and spleen, increasing circulation time, and is popularly regarded as a safe, effective way to improve nanoparticles for *in vivo* use [20, 26-32].

Figure 3: PEG structure (left) and function (right) as a non-fouling agent for nanoparticles. PEG can be chemically conjugated to the surface, incorporated using an amphiphilic version such as PEG stearate, or included pre-fabrication as part of the polymers or lipids that compose the nanoparticle. The hydrophilic PEG localizes to the exterior of the particle and sterically inhibits interactions with the surface, reducing protein deposition and aggregation.

Another tissue with which circulating nanoparticles must interact is the vascular endothelium. Size impacts the behavior of nanoparticles in vascular flow, and their tendency to adhere to the walls; flow analysis suggests that a diameter of 120 nm maximizes the time to migrate toward the vessel wall, thus increasing circulation time [33]. Several groups are investigating non-spherical particles to modify flow behavior, biological interactions, biodistribution, and drug release kinetics [34-38].

To reach the target tissue, the nanoparticles must exit the bloodstream, or extravasate. This process is strongly dependent upon the local endothelium in the vessels, but the most porous, the discontinuous endothelium of the liver, spleen, and bone marrow, only has gaps of 30-500 nm [39-40]. Smaller particles are more likely to pass through these small openings. Once the nanoparticles arrive at the target tissue, they must be internalized to deliver the therapeutic payload. Because they are too large for passive transport across the membrane, this generally occurs via endocytosis [41]. Particle surface properties and targeting molecules play a significant role in this process, but it is also strongly dependent

on size. Several models of the energetic and kinetic limitations to endocytosis have been designed, and the optimal particle diameter shown to be 50 – 60 nm [42]. However, the size of the endocytotic vesicle ranges from 90 – 120 nm, depending upon the mechanism of uptake [43].

Based upon the mechanisms of clearance, interactions within the vasculature, extravasation, and endocytosis, the ideal size of a therapeutic nanoparticle appears to be 50 – 100 nm diameter, though the actual delivery efficiency depends heavily on the surface properties of the particles and the specific target tissue. Nonetheless, the biodistribution and clearance, and, therefore, the efficiency and toxicity of a nanomedicine are extremely sensitive to size.

Nanotechnology presents some unique challenges to regulation. The connection between size and both the performance and safety of nanomedicines has garnered significant attention, and, as it is not a parameter considered for previous technology, many feel that current metrics and standards may not be sufficient [44]. However, the situation becomes more confusing, as nanotechnology frequently defies the conventional FDA categorizations of drug, biologic, or device, with many systems blurring the boundaries [45]. Thus, nanomedicine is a field with new principles, properties, and problems, and it does not fit into the conventional regulatory structure. It is crucial for those evaluating safety and setting guidelines to understand this relatively new field, and so the FDA set up a Nanotechnology Task Force in 2007, though many remained uncertain as to whether this approach would help or hinder the approval of new therapeutics [46-48]. The study concluded that regulation requires better, more appropriate metrics for quality and safety, and a focus on product stability and uniformity [49]. Thus, consistent, uniform size is one of the most crucial parameters to nanoparticle performance and to regulatory approval.

Nucleic acid therapeutics

Transfer of genes from one organism to another has enabled countless discoveries over the past several decades, ranging from studies of gene function and regulation [50-51], disease models [52-53], and the production of engineered proteins [54-56]. While initially, recombinant gene expression was limited to bacteria and yeast, higher organisms followed, and gene delivery to humans became a feasible goal [57]. The "holy grail" of gene delivery is gene therapy, in which DNA is introduced to the cells of a patient to replace the function of a deficient gene—a possible cure for a host of genetic diseases, like cystic fibrosis and severe combined immunodeficiency disorder (SCID), and even some acquired diseases such as type 1 diabetes and cancer [40, 58]. Rather than ongoing treatment with drugs to manage symptoms, a patient would express the gene product endogenously, in quantities controlled by regulatory sequences. Thus, a type 1 diabetic, for instance, could produce insulin in response to blood sugar levels. In addition to monogenic disorders, gene therapy also holds great potential in the treatment of cancer, with the majority of current clinical activity focusing on a range of cancer targets; cardiovascular disease and therapeutic angiogenesis also shows promise as a disease target [59]. However, safety and efficiency are major hurdles to overcome before such therapies can be practical [60]. To date, over 1800 clinical trials of gene delivery have been approved, though only about 20% of them are beyond phase I or I/II [59]. Nonetheless, the great potential of gene therapy still renders it an attractive goal, and progress toward practical therapeutic use in human continues [61].

Another notable therapeutic strategy is gene knockdown via either antisense or RNA interference (RNAi). In 1978, Stephenson and Zamecnik successfully used sequence-specific oligonucleotides binding to inhibit gene translation [62]. If the antisense binding spans an RNase H cleavage site, which occur relatively frequently in the genome, the

nuclease degrades the mRNA; antisense binding can also modify splicing and polyadenylation [63-66]. DNA oligos are usually preferred for their superior serum stability, which can be further improved by backbone modification [67]. Vitravene (fomivirsen), a modified antisense oligodeoxynucleotide (As-ODN) drug, was developed by Isis Pharmaceuticals, Inc., for the treatment of cytomegalovirus retinitis, an HIV-associated condition, and in 1998 became the first nucleic acid therapeutic approved by the FDA [68]. Better treatment of HIV reduced the frequency of the condition, and Isis stopped marketing it in 2008 [69], but its approval paved the way for further development of antisense and nucleic acid therapeutics.

Regulation of gene expression by endogenous RNA was first discovered in plants in 1986 [70]; this discovery led to the development of RNA interference (RNAi) as an alternative therapeutic strategy [71]. Native RNAi requires 60-80 base single-stranded micro RNA (miRNA)to bind to mRNA in the cytoplasm, triggering the RNA-induced silencing complex (RISC), which activates endonucleases to cleave the bound RNA preventing translation [72], a mechanism of the cellular defenses against viral infection. However, this typically elicited only nonspecific reactions in mammalian cells, until it was discovered that shorter double-stranded RNA could produce the desired gene knockdown [73-74]; these 20-25 bp fragments are small interfering RNA (siRNA). Interestingly, RNA can also activate gene expression (RNAa) [75]. There are several reasons for the popularity of RNAi and antisense as a therapeutic method. Though similar in cellular uptake and duration of action, RNAi produces significantly greater gene knockdown effects than antisense[67]. Unlike the delivery of plasmid DNA and RNase H-dependent As-ODNs, siRNA and miRNA only require cytoplasmic delivery, and produce only short-term effects, rendering them both easier and safer to use. While the formulation and delivery remain a challenge [76],

different therapeutic targets do not require the development of distinct vectors, significantly reducing the costs and risks of an RNAi pipeline [77-78]. Furthermore, the relatively recent discovery has left the IP space relatively open for commercialization [77]; the awarding of the Nobel Prize in 2006 to Fire and Mello for RNAi only fanned the flames of corporate interest in the technology [72]. Using oligonucleotides to regulate gene expression is a potential therapy for viral infection and cancer, and has already been shown to successfully treat macular degeneration, and large companies such as Roche, Novartis, and AstraZeneca have invested millions in the over the past 5 years [79-81]. Both antisense and RNAi are hot properties for the pharmaceutical industry [78, 82-84].

An additional mode of therapeutic utility for nucleic acids is as a customizable molecule for specific binding. Unlike gene delivery, RNAi, and antisense, aptamers do not rely on either the genetic information or complementary base binding of the oligonucleotide sequence, but rather upon their shape and affinity for a chosen target. These single-stranded oligomers are not found in nature, but are developed to bind a particular target by *in vitro* affinity screening and selection, *via* a process commonly referred to as SELEX [85-86]. The second nucleic acid therapeutic approved by the FDA came in 2004 with Macugen (pegaptanib), an anti-VEGF aptamer for the treatment of wet age-related macular degeneration [87]. Though aptamers lack many of the biological and delivery challenges of other nucleic acid therapeutics, with nuclease resistance conferred by their three-dimensional shape and modified nucleotides [87-88], they do have in common the challenges of the development and production of a relatively new class of therapeutic agents.

Production of nucleic acids in the necessary quantities for therapeutic use is another challenge to development. Plasmid DNA is relatively simple to amplify via bacteria; improvements in bacterial strains, growth conditions, and purification have been made, but

the process has remained largely the same for decades [89]. Oligo DNA and RNA, on the other hand, are more complex to produce. For conventional large-scale synthesis, solid-phase phosophoamidite chemistry is used, with the growing chains linked to resins in a packed column [90-91]. Though the process is now carried out with automated synthesizers [92], costs go up as oligo length increases; longer oligos are more likely to contain errors. The scale of such synthesis is also relatively low, with "large scale" defined as 1 – 10 g quantities. This translates to between 20 and 30,000 doses, depending upon administration; with many therapies requiring dosing every two weeks, that would be sufficient for only a few thousand patients at best [87, 93-95]. Many consider oligo synthesis to be a limiting factor, adding to the cost of the resulting drugs. Macugen, for instance, was initially priced at $800/dose [96-97]. Nonetheless, some companies report a total manufacturing capacity upwards of 30 kg/year, and improved methods, such as modified columns and the use of dinucleotides to reduce the steps in the synthesis of larger oligos [91, 97]. An alternative synthetic technique, polymerase-endonuclease amplification reaction (PEAR), allows *in vitro* PCR amplification of oligos, potentially increasing both yields and purity [98]. Despite such improvements in oligo synthesis, any optimization of agent fabrication and delivery remains of great interest to facilitate drug manufacture and lower costs.

Vectors

Though nearly 20% of gene therapy trials have utilized naked DNA, this requires either local administration to the tissue, or *ex vivo* transfection of cells [59]. Both Vitravene and Macugen rely upon intravitreous injection to treat the retina [87, 94]. Naked nucleic acids are vulnerable to nucleases and do not readily enter cells; RNA and DNA must be packaged for good transfection with systemic administration. Gene delivery vectors are generally divided into two major classes: viral and non-viral. Fundamentally, viruses are gene

delivery machines, evading the immune system to deliver a payload of nucleic acid to a particular cell type. These properties have been fine-tuned by evolution over countless generations, and so engineered viruses have naturally been considered the ideal vectors for gene delivery.

Viral systems do, however, have considerable drawbacks. Because viruses are pathogens, their capsids typically produce strong immune reactions, which can be a significant risk for *in vivo* use [99]. Retroviruses, such as lentivirus, also have the potential to insert the transgenes into the host chromosome, which, though enabling persistent expression of the genes, may cause cancer by disrupting the host genome [100]. Due to the relatively high efficiency of viral gene delivery, more than ¾ of clinical trials focus on such vectors [59]. However, the previously unforeseen safety issues have led to general caution concerning human use—the only gene delivery product on the market is an adenoviral cancer therapeutic, and was approved only in China [101]. Furthermore, because viral genomes are relatively small compared to those of higher organisms, the capacity of viral vectors is limiting. Though the transfection efficiency is considerably lower, non-viral systems are favored for their relative safety and ease of preparation.

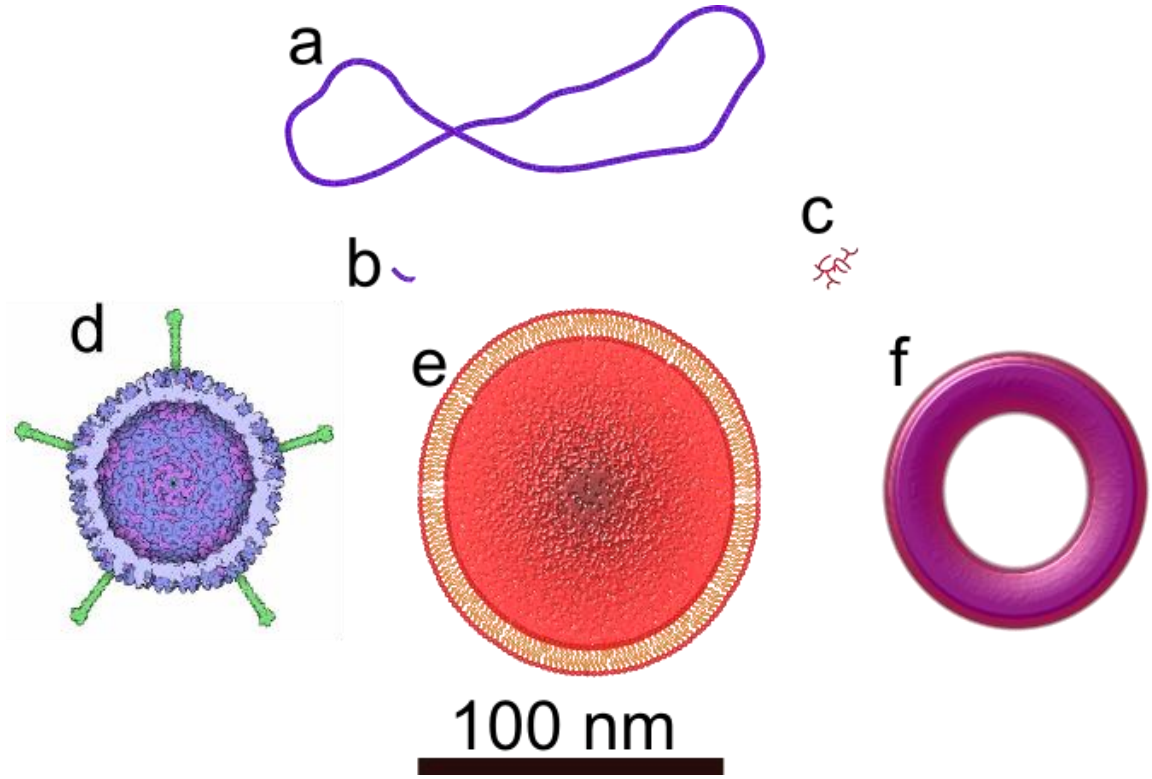

Figure 4: Relative scale of gene delivery vectors. The 5.7 bp gWiz GFP plasmid (a) has a hydrodynamic diameter of 114 nm [102], while a 22 bp DNA oligo (b) would measure only 7.5 nm, and the diameter of 25 kDa branched PEI is around 8 nm [103]. Adenovirus, a popular viral vector (d), measures 70 – 90 nm [104], while liposomes (e) and polyplexes (f) for nucleic acid delivery typically measure between 20 and 500 nm. Non-viral methods typically rely on cationic species to interact with the polyanionic nucleic acids to condense and package them. Histones, viral capsid proteins, and the polyamines spermine and spermidine all utilize this feature to compact DNA in nature, and synthetic compacting agents are also cationic. Though DNA can be complexed with a large variety of positively charged molecules and structures [105], the most common agents are cationic lipids and polymers.

Lipid-complexed DNA forms vesicular structures called lipoplexes. The technique has been in use for decades, and Lipofectamine remains a common standard for transfection efficiency [106]. Particularly with the addition of neutral "helper lipids", lipoplexes readily associate with membranes and facilitate release of DNA from the endosome [40, 95, 107].

6% of clinical gene therapy trials have involved lipid-based vectors [59]. However, variations in fabrication and an incomplete understanding of structure remain drawbacks of such systems [108]. Uniform and reproducible structures are crucial to reliable transfection efficiency and *in vivo* behavior for both lipid and polymer-based systems.

A wide variety of polymers can be used to compact DNA into polyplexes, most commonly poly-L-lysine (PLL), chitosan, diethylaminoethyl-dextran (DEAE-dextran) and polyethylenimine (PEI) [109]. A major advantage of polyplex systems is the ability to create multifunctional systems via copolymers and conjugated ligands and labels for targeting, uptake enhancement, enhanced biocompatibility, nuclear localization, and tracking [29-30, 108].

Barriers to Cellular Delivery

For successful nucleic acid delivery, the DNA or RNA must cross the cell membrane and enter the cytoplasm (Figure 5). While RNAi only requires cytoplasmic delivery, knockdown by RNase H or gene expression only occur if the plasmid or oligo enters the nucleus.

Unless the cell membrane is either physically breached or disrupted, as by microinjection, particle bombardment, or electroporation, the vector must be taken up by endocytosis [107-108, 110-111]. Though physical means can be efficient and exhibit low toxicity to cells *in vitro*, they are considerably less feasible for anything beyond localized gene delivery to accessible tissues *in vivo* [108], limiting the utility of the method. Endocytosis does not require direct access to the cells, increasing the range of possible physiological targets. Furthermore, the inclusion of particular ligands on the surface of the vector both increases efficiency and enables transfection of particular cell types [112].

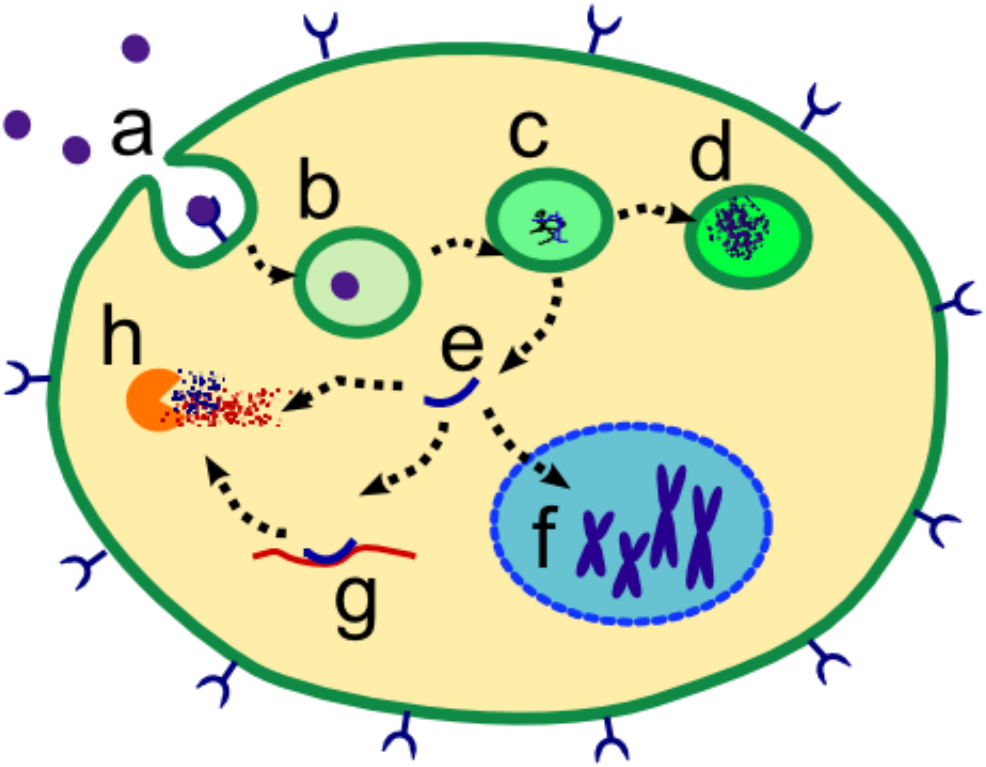

Figure 5: Schematic of cellular transfection. The vector is typically internalized *via* endocytosis (a), which may be aided by inclusion of a targeting ligand. The endosome (b) begins to acidify (c), and will eventually become a lysosome (d), degrading its contents. Before this occurs, the nucleic acid must escape the endosome into the cytoplasm (e). There, transgenes or antisense DNA must be transported to the nucleus (f) to function. By contrast, siRNA and miRNA operate directly in the cytoplasm (g), but may be digested by endonucleases (h).Once the vector has been taken up by endocytosis, it is contained within a vesicle called the endosome, which the cell acidifies to digest the contents [113]. In order to enter the cytoplasm, the vector must contain some mechanism to rupture the endosome. Typically, this involves fusogenic peptides or lipids, buffering capacity, or a pH-driven change in hydrophobicity to disrupt the lipid bilayer [40, 114].

This is sufficient for RNAi, but in order to achieve gene expression, plasmid DNA and antisense oligos must enter the nucleus and release from the vector. The nuclear pore is approximately 55 nm in diameter, so most gene delivery vectors require active transport through the nuclear pore complex [111]. Transport can be considerably enhanced by the inclusion of nuclear localization signals (NLS), but efficient entry to a non-dividing nucleus

remains a major hurdle for effective gene delivery [115]. Given the difficulty of nuclear transport, maximizing the amount of DNA internalized per transfection event is crucial to achieve good expression. However, the release of nucleic acids within the cell triggers an innate immune response via the Toll-like receptors (TLR). Double- and single-stranded RNA and CpG-containing DNA, present during viral or bacterial infection, trigger TLR3, TLR7, and TLR9, respectively [116], all of which are localized to intracellular compartments to probe endocytosed material [117]. Though TLR9 is the primary trigger of inflammation by DNA administration, other, less-understood mechanisms also contribute to systemic toxicity [118]. Thus, higher doses, even when internalized by the target tissue, are undesirable.

Achieving the right balance is a considerable challenge. The nucleic acids must be well packaged for protection, but still release readily within the cell [119]. The vector must be small enough to successfully reach the target tissue, but large enough to contain sufficient DNA or RNA for activity. The choice of vector system and its physical properties are crucial to effective gene delivery. Size, in particular, is a crucial factor for evading the immune system, tissue access, endocytosis, and overall transfection efficiency [120-123].

Overall challenges to clinical use

Regardless of the type of nucleic acid therapy, delivery to cells *in vitro* and *in vivo* remains the primary barrier. Though non-viral delivery is preferable for the increase in payload and reduction in immunogenicity, transfection efficiencies remain low, with 5%-10% transfection *in vitro* for good vectors, and considerably lower *in vivo* [124]. Furthermore, increasing the therapeutic dose is not feasible; therapeutic doses of DNA for humans range from 150 μg to 2 mg [94, 124-125], a large amount to produce, given the short duration of transfection (< 2 weeks), and larger doses increase immune response and toxicity.

Therefore, it is of great interest to maximize efficiency of delivery. While mechanisms such as tissue-specific targeting and shielding by PEG [29, 126] assist in this goal, size remains a crucial parameter to increase efficacy and reduce the necessary dosage and accompanying adverse effects. Moreover, because it affects bioavailability, clearance, and toxicity, size is of great importance for all nanomedicines, and good control and characterization are essential to the development of new therapies for regulatory approval and clinical use [44, 47, 127].

The system

DNA and charged polymers

Polymers have significantly different properties than their substituent monomers or other small molecules. Many consist of hundreds or thousands of units; their large size severely limits their diffusion. The number of functional groups tethered in close proximity has a large effect on the kinetics and thermodynamics of interactions [128]; and their conformation and, thus, their interactions are sensitive to hydrodynamic forces [129-130]. Charged polymers, such as DNA and PEI, also behave quite differently than smaller ions.

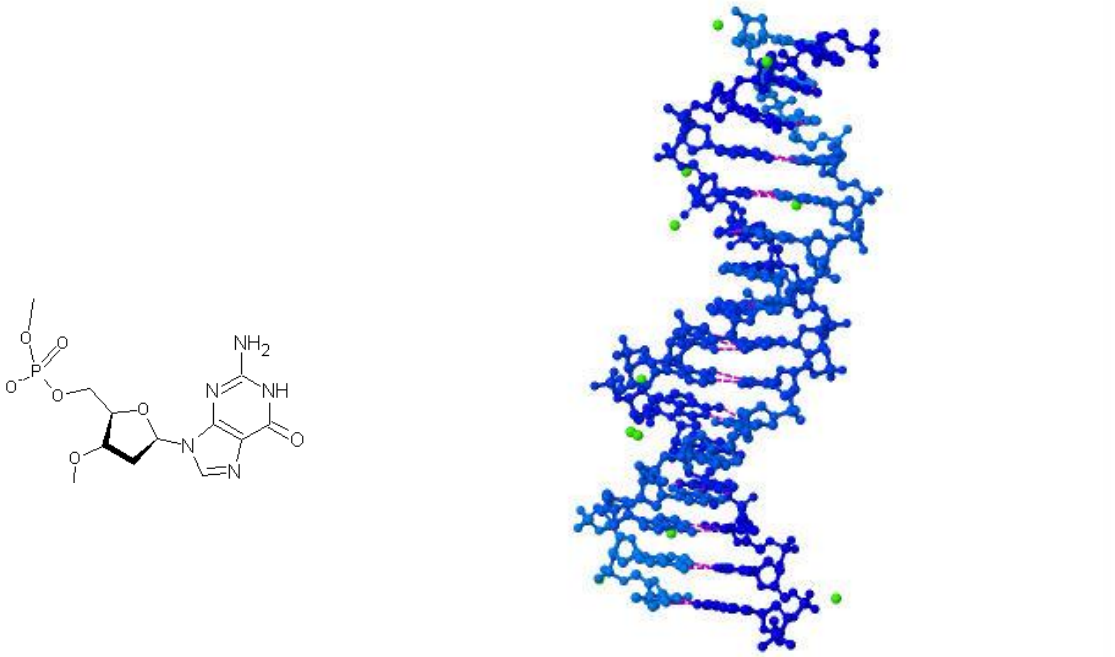

Figure 6: A deoxyriboguanine nucleotide (left), and the crystal structure of DNA, from PDB structure 3BSE (right) [131]. The negatively charges phosphates of the spiraling backbone are oriented outward, while the bases form hydrogen bonds in the center (dashed magenta lines). Guanine (shown, left) and cytosine form three hydrogen bonds, while adenine and thymine form two. The green species in the structure are Mg^{2+} ions

The complex structure of nucleic acids gives them some fairly unique properties. The most common form of DNA is a B-form double helix, in which the hydrophilic sugar-phosphate backbone is oriented outward (Figure 6), spiraling around the hydrogen bonded and horizontally stacked base pairs [132]. The interior is a hydrophobic environment, and a number of intercalating dyes take advantage of this property [133]. RNA may be either single or double-stranded, but is better known for complex secondary structures, as in tRNA, rRNA, and ribozymes [134-135]. When single-stranded, either nucleic acid is relatively flexible and prone to self-association into secondary structures such as hairpins. Double-stranded nucleic acids, on the other hand, are quite stiff, with a persistence length of 50 nm, or about 150 base pairs [136-137]. Thus, oligos are relatively rigid, particularly when < 50 bp (16 nm). Longer DNA molecules, such as plasmids, are flexible over their

length, but the hydrodynamic radius and diffusivity of even a 5.8 kb molecule are still strongly influenced by its mechanical structure-- supercoiled, open circle, and linear [102].

The phosphate groups have a pK_a near 0, and so the molecule carries a charge of -2 for each base pair, a substantial charge density [135]. This electrostatic charge gives large DNA molecules an electrophoretic mobility similar to those of much smaller ions (Table 1, Aim 3). Furthermore, this charge density creates a local potential field, and results in substantial interactions with neighboring ions and water molecules [138-140]. Counterion shielding by monovalent species has little effect on the electrophoretic mobility at low concentrations [141-145], but transient interactions with buffer ions can have an effect [146]. As significant as DNA and RNA interactions with counterions are, the association with water molecules is of far greater magnitude. While each base pair may interact with one or two ions, there are 20 hydration sites [147-148], making the polyelectrolyte a truly complex environment. Water molecules tend to accumulate in the minor groove (Figure 7), resulting in local concentrations around the DNA 2 to 6 times greater than the bulk [149]. DNA is a relatively large molecule with intricate structure, with a large, complex, semi-ordered population of molecules surrounding it.

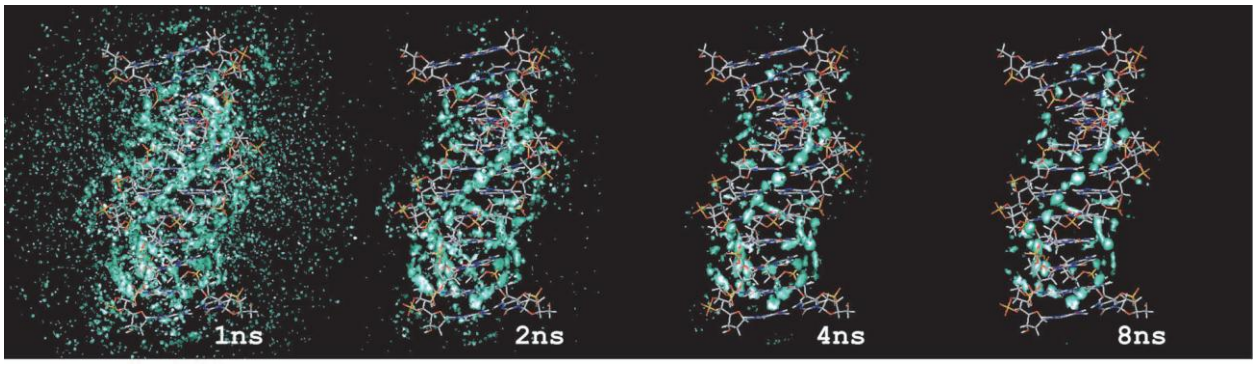

Figure 7: Results of a molecular dynamics simulation of DNA and associated ions and water molecules by Yonetani, et al. [149]. Marked regions represent where the concentration of water is > 2.25 times the bulk concentration, indicating strong attraction and long-lived associations.

Polyethylenimine (PEI) is a polycationic polymer, noted for complexation with DNA to produce relatively high transfection efficiency [150]. PEI is, therefore, a model transfection agent for *in vitro* studies. It is typically branched (Figure 8), with primary, secondary, and tertiary amines at an approximately 25/50/25 ratio [151-152], though linear PEI, consisting entirely of secondary amines, is also popular. This efficiency is attributed to the "proton sponge" effect, as the buffering capacity of the molecule exceeds the cell's ability to acidify the endosome, ultimately building osmotic pressure until the vesicle ruptures [150, 153]. The density of titratable nitrogen atoms gives the molecule this large buffering capacity, though their proximity causes interactions between them; thus pK_a must be determined empirically, and is both pH- and concentration-dependent [152]. The major drawback to PEI is its cytotoxicity. Free PEI associates with serum proteins and disrupts the plasma membrane, while internalized PEI damages the mitochondrial membrane [154]. However, other polymer and lipid formulations have similar problems [155]. Toxicity varies with the size and form of the PEI, as does transfection efficiency [151, 156-157], and PEI remains a popular condensing agent for nucleic acid transfer [28, 158-160].

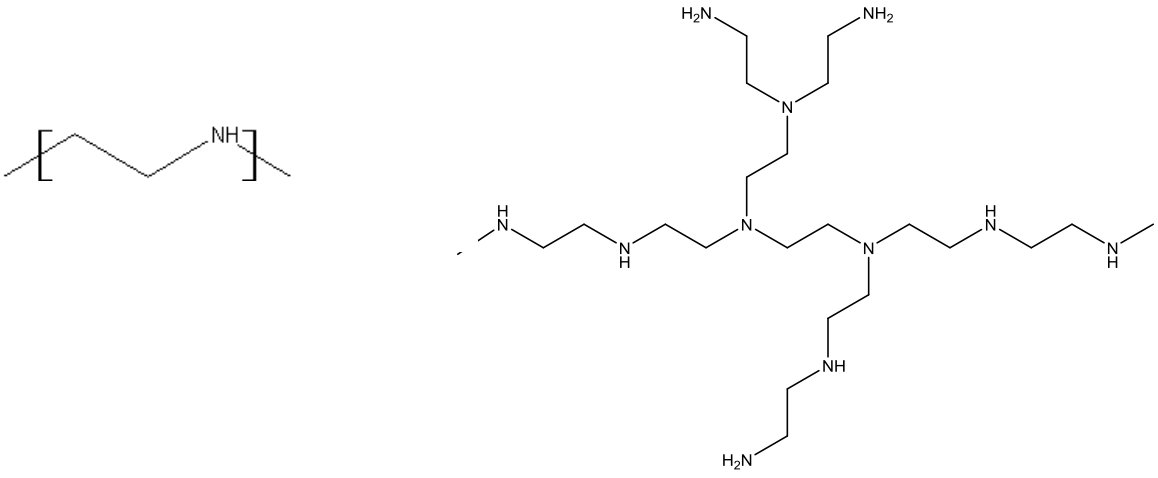

Figure 8: The formula and structure of branched PEI. Linear PEI contains only secondary amines, but branched PEI consists of primary, secondary, and tertiary amines, giving the molecule complex behavior with varying pH.

DNA complexation and complexes

The large negative charge of DNA results in significant interactions with cationic species. However, when the charge of the counterion is 3 or more, the interaction is both stronger and longer-lived, such that the charge on the DNA is largely neutralized [161-162]. When this occurs, the DNA falls out of solution and into a compact colloidal phase. This is the principle behind the compacting ability of spermine, histones, and viral capsid proteins, but will occur with any large cationic species, including cationic lipids, and polymers such as PEI.

Though electrostatic forces are responsible for much of the self-repulsion of a polyelectrolyte, and for the strong attraction between those of opposite charge, charge neutralization alone is not responsible for the compaction of DNA. In fact, the majority of the stiffness of DNA is due to its structure alone [136], and this stiffness is still apparent in the compact nanoparticles[163]. The primary force is actually dehydration of the molecule.

$$\Delta G^{\circ}_{H} = \Delta G^{\circ}_{vdw} + \Delta G^{\circ}_{cav} + \Delta G^{\circ}_{e}$$

Equation 1: Equation stating the free energy required to hydrate a molecule. ΔG°_{vdw} is the favorable van der Waals interactions between the first shell waters with a macromolecule, ΔG°_{cav} is the unfavorable entropic process of forming a clathrate cavity to fit the macromolecule, and ΔG°_{e} are the other electrostatic interactions between the water and the macromolecule [128]. Once the charge on the DNA has been 90% neutralized, the favorable interactions with water (ΔG°_{e}, Equation 1) are substantially reduced, and the energy of hydration is no longer favorable, and the complex becomes hydrophobic [161-162, 164]. Though compaction of the large DNA molecule and condensing agent physically restricts them, reducing their entropy, the large number of water molecules previously associated with it—roughly 20 per base pair—gain entropy, and collapse of the polymer reduces the number of waters in a clathrate.

Though the principles of polyplex formation are constant, they can be assembled differently for different applications. Of course, the small size and inherent stiffness of oligos prohibits any major deformation, so, given a small and/or flexible condensing agent, notable structure is unlikely, and complexes will adopt a globular morphology; longer DNA, however, shows some unique behavior of biophysical interest. Many studies focus on the nuances of structure, packing, and thermodynamic limits favor small condensing agents like spermine and hexamine cobalt, and low N/P ratios to maximize observation of the DNA backbone [165-167]. Size and polydispersity are controlled by sequence-directed nucleation templates or the gentle techniques of dialysis with small condensing agents or changes in salt concentration to initiate complexation [165, 168]. In such studies, the inherent stiffness of the DNA backbone results in the formation of toroids and rods (Figure 9, a and b), minimizing both the surface area to water and the need for sharp bends. For larger DNA, the minimum size of a nanoparticle is dependent upon the radius of curvature of the DNA, as the toroid is the most densely packed, energetically favorable geometry [168-170].

For gene delivery applications, on the other hand, biocompatibility and transfection efficiency of the compacting agents and polyplexes is of paramount importance, so polymer systems at higher N/P ratios are used, and mixing is typically achieved by vortexing [27, 29, 119, 157, 171]. The resulting particles are typically less structured, and more variable in size and shape (Figure 9, c and d). The bulk properties of the nanoparticles and function as transfection agents are the crucial properties, so size and polydispersity are often the only two parameters reported. Clearly, the fabrication process for gene delivery is considerably more difficult to control.

Though formulation parameters such as concentration, salts, and N/P ratio are the conventional means of manipulating polyplex properties, the assembly kinetics are a strong

determinant of size and polydispersity. The manner and order in which reagents encounter each other has a significant impact on the final particle properties [172]. Characterizing and controlling the physical aspects of the process will lead to particles of more uniform and reproducible parameters.

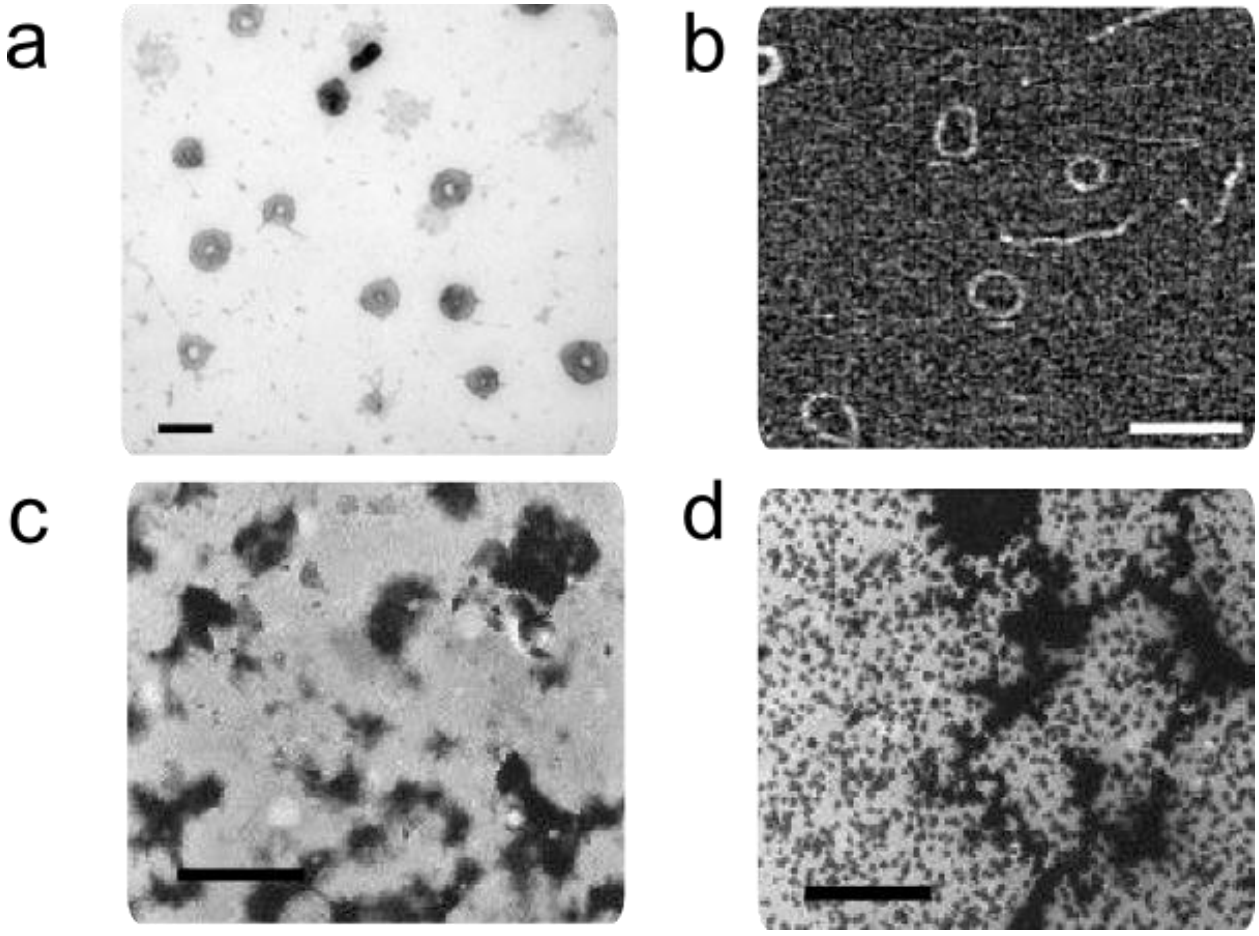

Figure 9: Images of assorted DNA complexes. TEM image of particles formed by hexammine cobalt (a, scale bar is 100 nm) show the stability of the toroid structure [169]. Real-time monitoring of complex formation with a PEGylated poly(amido amine) *via* AFM (b, scale bar is 300 nm) reveals the process of toroid growth, and the development of rods, which are less stable, due to the need for tight bends at either end [173]. TEM image of the less controlled assembly conditions with PEI (c, scale bar is 1 μm) and DOTAP (d, scale bar is 1 μm) produce more variable particles, which may not produce the toroid structure before aggregation [174].

Equilibrium vs. kinetics

The interaction conditions affect the nanoparticle formation because the complexation is kinetically controlled; the desired endpoint is not a global energy minimum. Considering

the hydrophobic nature of the condensation, the thermodynamic endpoint would be complete phase separation with minimal surface area presented to the solvent (Figure 10). In fact, one of the chief problems of non-viral vectors is their instability in solution, and tendency to grow and eventually aggregate over time, unless the kinetic trapping is enhanced by PEGylation of the particles, or the nanoparticle concentration is sufficiently dilute that further interactions are unlikely [29-30, 164, 175-178].

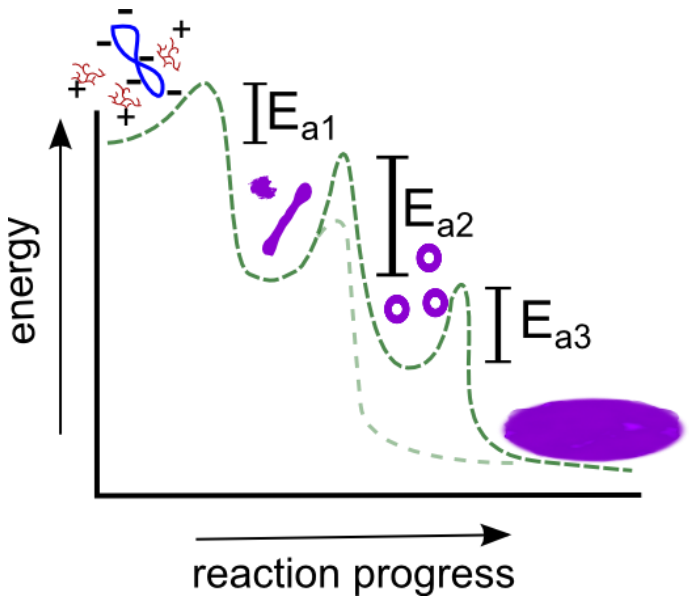

Figure 10: Schematic of relative energy states during DNA complexation. Because the polyelectrolytes are strongly attracted, E_{a1} corresponds to transport effects, and is significant only at very low concentrations. The increase in global entropy from the release of associated water molecules is strongly favorable, but, given the size of the system, the lowest energy conformation is not guaranteed and other structures, such as rods or globules, are likely, depending upon the size of the DNA, the nature of the condensing agent, concentrations, and buffer conditions. The DNA and condensing agent can undergo rearrangements, and develop into toroids over time, but large scale rearrangements require several high-energy conformation steps, so this process is slow, and E_{a2} is relatively large. Ultimately, the lowest energy state is a complete phase separation, but this requires transport of the complexes *via* diffusion to within the necessary range for interaction; E_{a3} depends upon the concentration, and may be lower than E_{a2}, such that toroids never form within the system. However, PEGylation of the complexes effectively raises E_{a3} by providing a steric barrier to interaction, and stabilizing the complexes.

Kinetic control is common in chemistry and nanofabrication [179-183], and also appears to be at work in DNA complexation. The carefully controlled conditions of biophysical

experiments (e.g. dilute solutions, dialysis, and long observation times) are specifically to achieve a thermodynamically optimal result: well-structured DNA toroids [161, 163, 169-170]. Under such conditions, the minimum particle size is dependent upon the radius of curvature of the DNA, and the resulting particle size is a function of nucleation-growth kinetics (Figure 11) [167-170, 184]. However, particle size and stability are highly sensitive to both the relative (e.g. N/P or charge ratio) and absolute concentrations of the species [175, 185-187]. Thus, suspensions at clinically useful concentrations typically to have a finite lifetime before aggregation [164, 174-176], unless a shielding agent such as PEG is used [11, 27-28, 30].

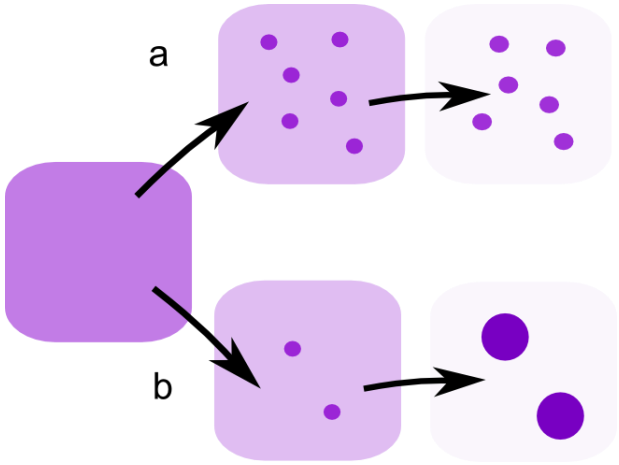

Figure 11: Illustration of nucleation-growth kinetics. The simultaneous development of many nuclei (a) spreads the material over a larger number of bodies, producing smaller particles; when nuclei are scarce (b), the system produces fewer, but larger particles. The process depends upon both the energy barrier to nucleation relative to that of deposition, and the timing of transport. The balance of those barriers dictates the relative rate constants of the nucleation and deposition processes, while the transport defines the local concentrations of species and, thus, the local rates of those processes [188]. Smaller particles are more likely in a homogeneous system (i.e. one that is well-mixed), while a system introducing fresh material to existing nuclei encourages deposition, rather than self-nucleation, and, thus, larger resulting particles.

The range of and intensity of the electrostatic attraction makes the initial interactions quite rapid—on the order of 1 ms [189], though further growth occurs over minutes, with near-complete aggregation within 24 hours [164, 175]. This difference in energy and timing for the processes produces a meta-stable, kinetically trapped state. A large zeta potential, or

surface charge, increases the stability of the suspension, as the complexes repel one another, but this destabilizes them *in vivo*. Although the DNA and condensing agents retain some mobility within the complex [189], the energy required for disentanglement and rearrangement into a more thermodynamically stable state is such that the rate is quite slow; at clinically relevant concentrations, complexes are more likely to diffuse and encounter each other until they reach such size as to fall out of solution (Figure 12). Relatively high concentrations are required for therapeutic use, biasing the system toward greater interactions between complexes, and, therefore, larger particles and potential aggregation. To produce good quality particles at relevant concentrations, deliberate kinetic trapping is necessary. One way to do that while minimizing particle size, at least for point-of-care use, is to accelerate the complexation [182]. As polyplex assembly is largely transport-limited, due to the size of the species, the mixing process is of paramount importance. Though growth and accumulation continue over minutes to hours, the initial interaction occurs in < 50 ms [173, 175-176, 178, 190-192]. While the behavior of DNA under shear prevents further measurement resolution, it also means that the process remains transport-limited under any slower method. Thus, the kinetically trapped state will depend upon the specifics of the mixing process, and controlling that process will control that state.

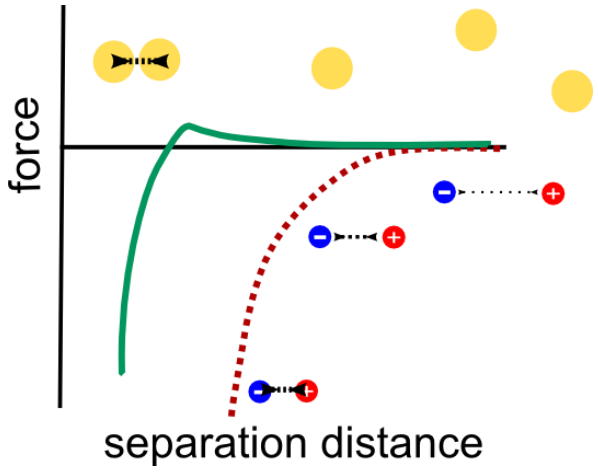

Figure 12: Illustration of force as a function of distance between species. For simple species with opposing electrostatic charges (red dashed trace), the force is proportional to the magnitude of charge, and the inverse of the square of the distance. For charged polymers, the maximum distance for attraction is quite large, and the initial interactions are rapid. Weakly charged species, such as DNA/PEI complexes, do not interact over long distances, and may repel if the zeta potential is large enough. However, large zeta potentials reduce stability *in vivo*, and low surface chares permit interactions. At short distances, the electric double layer and van der Waals forces do produce attractive interactions (green trace) [193], and the hydrophobic nature of complexation causes unshielded complexes to adhere.. Suspensions of DNA complexes are stable over short time scales, but will ultimately aggregate over a few hours [164] unless a minimum separation is maintained, either by reducing concentration to limit interactions, or physical separation by PEGylation.

Key principles and techniques

Microfluidics

Reynolds number and laminar flow

A microfluidic system is defined as one in which at least one dimension is less than a millimeter. The many processes and materials behave quite differently at such small dimensions, and several dimensionless parameters describe these differences of scale. Perhaps the most crucial is the Reynolds number (Re), which describes the ratio between inertial forces to viscous forces [194].

$$\mathrm{Re} = \frac{Lu\rho}{\nu}$$

Equation 2: Reynolds number, describing the relationship between inertial and viscous forces in fluid flow. L is the characteristic length (m), usually the smallest dimension of a system, u is linear velocity (m/s), ρ is fluid density (kg/m^3), and ν is the dynamic viscosity (Pa*s).The small dimensions of microfluidic systems

usually result in low values of Re, in which viscous forces dominate. For low flow rates and small dimensions, Re < 0.1, creeping flow results, and the fluids track with the walls in streamlines independent of the flow rate. Turbulence sets in at Re > 2100, and only extremely high flow rates can produce this in a microchannel. At intermediate flow rates, flow remains laminar, but the momentum of the flow may be evident, producing recirculation and eddies dependent upon the flow rate (Figure 13). Though most microfluidics devices operate at low Re, mixers often require slightly higher values.

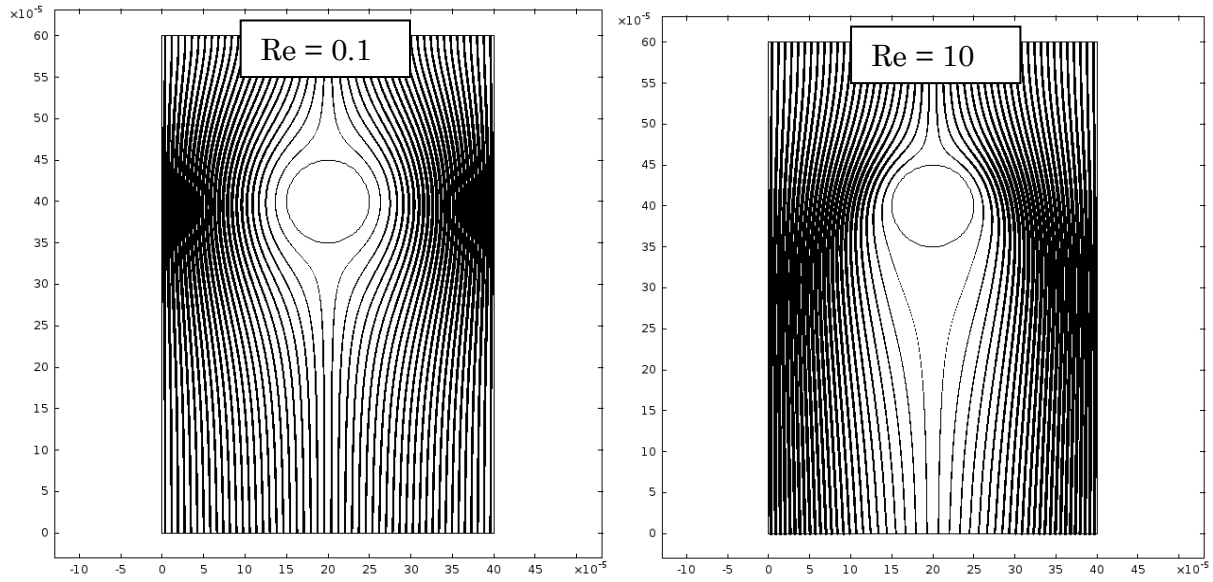

Figure 13: Illustration of the effects of Re on streamlines passing a post. Flow proceeds from top to bottom, line thickness indicates relative velocity. At low Re (left), flow is dominated by the viscous effects of the walls, and streams follow the geometry closely. At higher Re (right), momentum forces the fluid past the post, leaving a large stagnant region downstream. In other geometries, this may produce flow separation and pockets of recirculation.

The ruling equation of microfluidic systems is the Navier-Stokes equation. For aqueous solutions in a microchannel, gravity is negligible and density can be considered constant, so the equation reduces significantly to,

$$\nabla p = \nu \nabla^2 \mathbf{v}$$

Equation 3: The Navier-Stokes equation, simplified for incompressible flow with no body forces. ∇p is the pressure gradient in Pa/m, ν is the dynamic viscosity in Pa·s, and v is the velocity vector in m/s.

Such simple flow is highly predictable. This is largely due to the no-slip boundary of the ever-present walls. For fully-developed flow in a simple duct, this constraint produces a parabolic Poiseuille flow profile, which has several implications. The laminar nature of the flow dictates fluid fate, and elements of the fluid near the center of the channel will stay in the center of the channel, and those near the walls will stay near the walls in the absence of diffusion or advection or other disruption to the flow. The no-slip boundary at the walls creates large gradients of velocity and residence time, leading to such complications as shear forces, Taylor dispersion (Figure 14), and "the butterfly effect" [195-196]. These phenomena can prevent mixing and complicate analysis, but they also render flow and solute movement highly predictable and controllable. Microfluidics are an extremely powerful tool, due to the interesting properties of low Re flow. The unique properties of microfluidics have already been applied to the controlled assembly of complex nanostructures [197-202]. The behavior of such systems is predictable and easily characterized, making microfluidics an excellent way to control the mixing and complexation of DNA and PEI. Additionally, the unique phenomena of the small scale may be harnessed to further manipulate the assembly process.

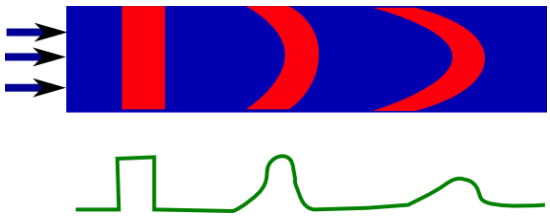

Figure 14: A representation of Taylor dispersion in two dimensions. The spatial variation of velocity in pressure driven flow can spread species out along the flow axis. In addition to distorting time-variant concentration profiles independent of diffusion (above, green trace), this also means that species experience varying residence times.

Mass Transport: Péclet and Damköhler Numbers

Regardless of system scale, mixing occurs when the scale of diffusion reaches the scale of system variations, ultimately producing homogeneous concentrations. The dominant equations of mass transport are Fick's first law of diffusion, which relates flux to a concentration gradient, and the general equation of convection and diffusion, which incorporates Fick's second law and the continuity equation [194].

$$J = -D\nabla c$$

Equation 4: Fick's first law of diffusion, describing mass flux. J is flux (mol/m²/s), D is diffusivity (m²/s), and ∇c is the concentration gradient (mol/m⁴).$\frac{\partial c}{\partial t} = D\nabla^2 c - \mathbf{v} \cdot \nabla c + R$

Equation 5: General equation of mass transport, including Fick's second law of diffusion for the change in concentration over time, along with convective transport and reaction terms. D is diffusivity (m²/s), v **is the velocity vector (m/s),** R **is the reaction rate (mol/m³/s), and c is the concentration of interest (mol/m³).**Another descriptor of importance is the Péclet number, Pe, which describes the ratio of convective transport to diffusion (Figure 15).

$$\mathrm{Pe} = \frac{Lu}{D}$$

Equation 6: Péclet number, describing the relationship between convective and diffusive transport. L is a characteristic length (m), u is linear flow velocity (m/s), and D is diffusivity (m²/s). While the small dimensions of a microfluidic device might suggest a small value for L, and therefore small values of Pe, this is not always the case in microfluidic devices. For flow rates measured in μL/s, the small dimensions frequently produce velocities on the order of 10 cm/s. Furthermore, in laminar flow, the length required for diffusion may remain fixed, while higher Re flow might assist in advection to reduce the length scale. Particularly for larger solutes like polymers, particles, and DNA, Pe can easily measure from 10^3 – 10^6 in a microchannel. Such large values indicate sharp concentration gradients, and hint at the challenge of mixing in microfluidic systems.

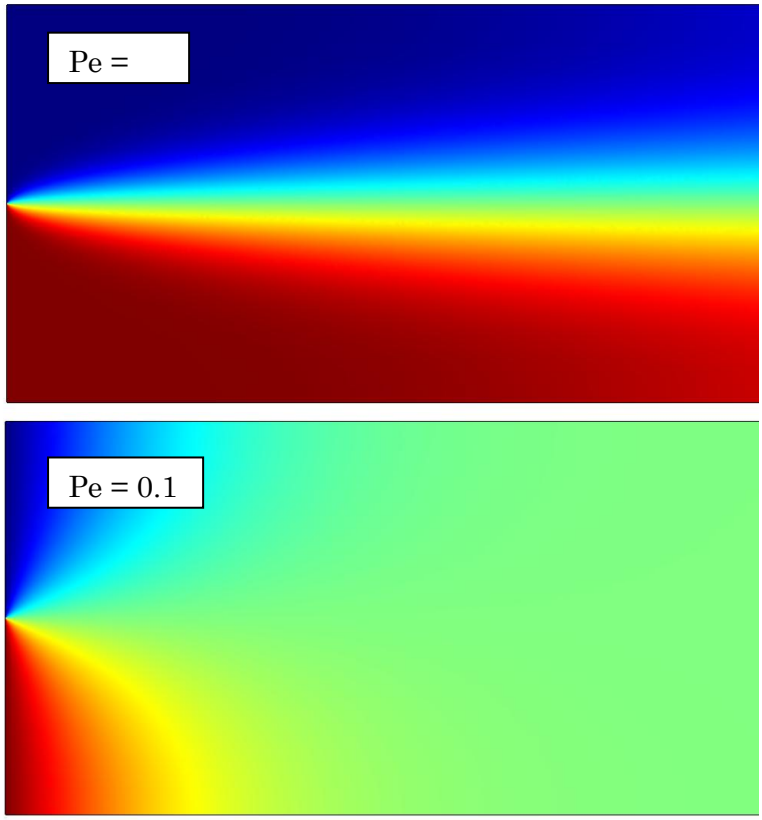

Figure 15: Illustration of Pe. At high values of Pe (upper), solutes are predominantly moved by convection, while diffusion dominates for lower values (lower).

For reacting systems, the Damköhler number, Da, is also worth consideration. It describes the relationship between the time for transport and the time for reaction. While the definition varies by both chemistry and geometry, two possible interpretations are of interest here: a local definition relating the reaction to mixing (Figure 16), and a device definition relative to the residence time, to evaluate reaction progress within the device.

$$\mathrm{Da} = \frac{kcL_i^2}{D}$$

Equation 7: Damköhler number of mixing, relating the rates of reaction and diffusion for a second order reaction , where k is the rate constant (1/s), c is the concentration of the limiting species (mol/m^3), L_i is the

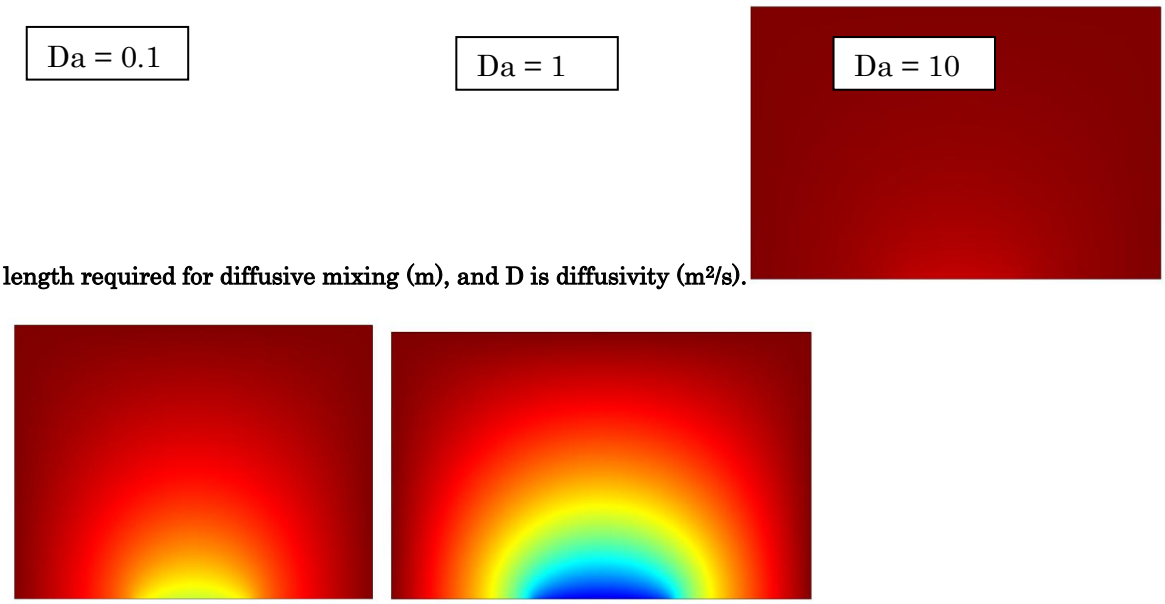

length required for diffusive mixing (m), and D is diffusivity (m^2/s).

Figure 16: Illustration of Da for a spatially-dependent reaction. The model depicts a solute reacting on a catalytic surface. At low values of Da (left), diffusion is faster than the reaction, and the reaction proceeds at its inherent maximum rate. For high values (right), the reaction is faster than diffusion, and the system is transport limited. At intermediate values (center), both factors contribute to the system reaction rate.

To produce uniform reaction conditions, mixing should be faster than the reaction, and Da should be small. However, large values of Pe suggest that mass transport is limiting, and Da is correspondingly high. In such cases, the actual reaction progress may be much slower than the inherent rate suggests, entirely dependent upon other aspects of the system such as mixing. Multiple groups have pursued microfluidic preparation of DNA particles, but few have considered actual in-device mixing, and none has monitored the complexation within the device [203-209].

Microfabrication

Several different methods to fabricate microfluidic devices have been developed; among them are micromachining, chemical etching, *in situ* photopolymerization, and micromolding [210]. The optimal method depends largely upon the application, but soft lithography with

polydimethylsiloxane (PDMS) is particularly popular [211]. The simplified process is illustrated in Figure 17.

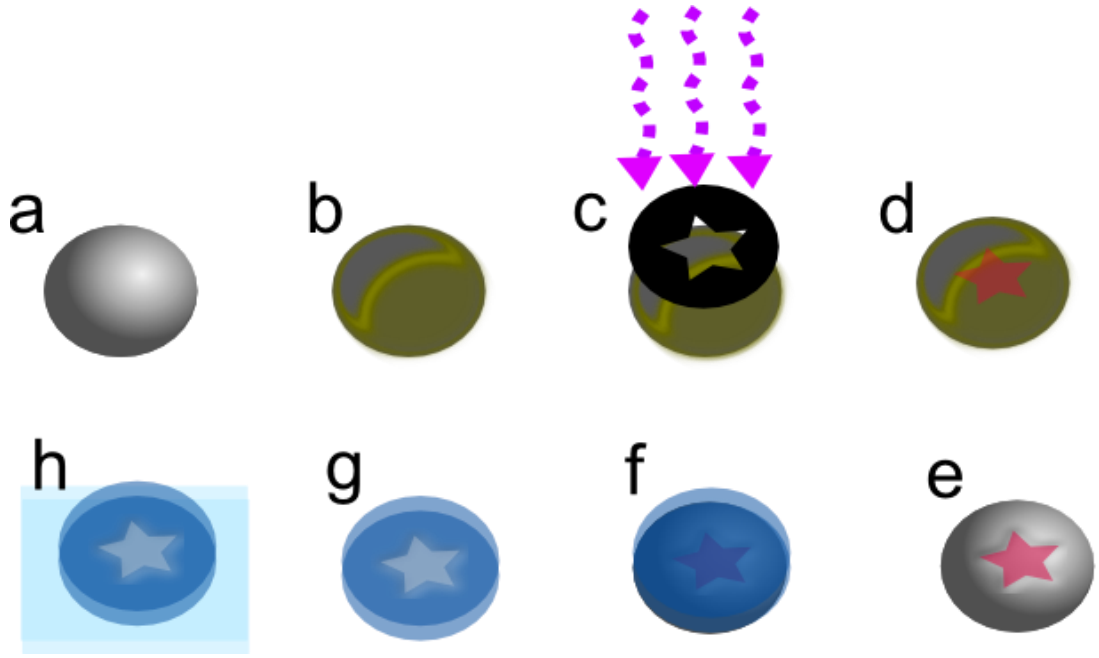

Figure 17: An illustration of the processes of photolithography and soft lithography. Clockwise, from upper left, a silicon wafer (a) is spin-coated with photoresist and baked until solid (b). The photoresist is cured in a pattern *via* exposure to UV through a photomask (c). Additional features may be added with another layer of photoresist and exposure. The exposed photoresist (d) is left when the uncured resist is removed by solvents (e). When PDMS is cast on this mold (f), a high-fidelity negative replica is produced (g), with channel spaces where the photoresist was. This piece can then be bonded to glass (h) or other PDMS by oxygen plasma.

While PDMS has many advantageous properties (e.g. optical transparency, mechanical compliance, gas permeability, excellent feature reproduction), it is also quite hydrophobic, which is particularly problematic for many biological applications. Resistance to wet-out allows bubbles to remain indefinitely at low pressures, and deposition of proteins and other biomolecules is inevitable. Thus, considerable attention has been paid to surface modification strategies [212-220]. Treatment with oxygen plasma renders the surface both hydrophilic and activated for bonding to glass or other activated PDMS surface (Figure 18) [221], but the mobility of polymers within the material allows recovery of the hydrophobic surface within several minutes, unless the surface is protected from air [222]. One of the

most versatile and convenient chemistries of PDMS is covalent linkage with silanes (Figure 19 - Figure 20). Use of surface modification techniques to render PDMS hydrophilic is popular [212, 217], though because any functional group can be incorporated *via* silane chemistry, it is one of the most useful techniques.

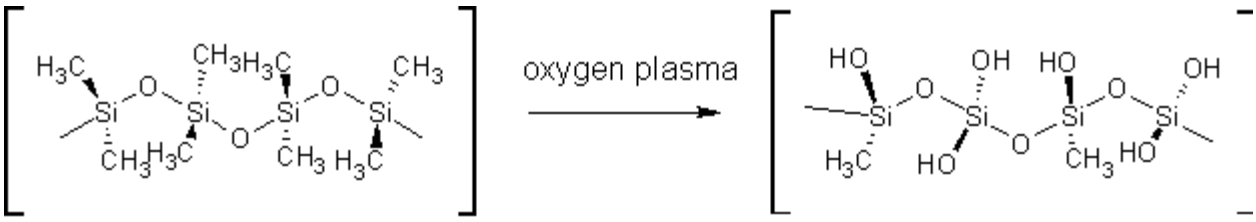

Figure 18: The surface structure of PDMS, and activation by oxygen plasma. Though oxygen plasma converts the hydrophobic PDMS surface to hydrophilic silanols, the mobility of chains in the material result in replacement of the hydrophobic surface within hours. Excessive plasma treatment results in a brittle surface of silicon dioxide.

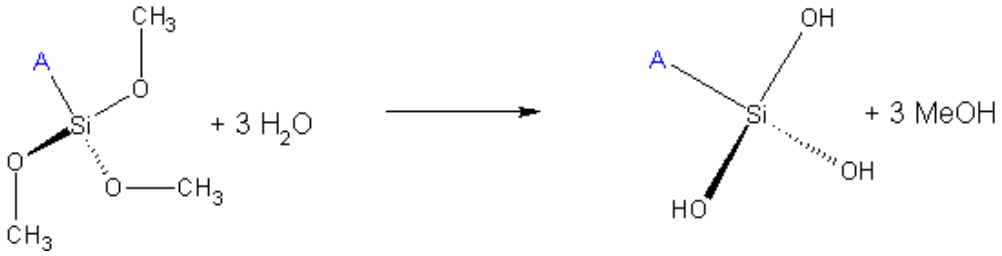

Figure 19: Activation of trimethoxy silanes. "A" represents an arbitrary functional group. The methoxy groups readily leave in the presence of water, leaving highly reactive silanols.

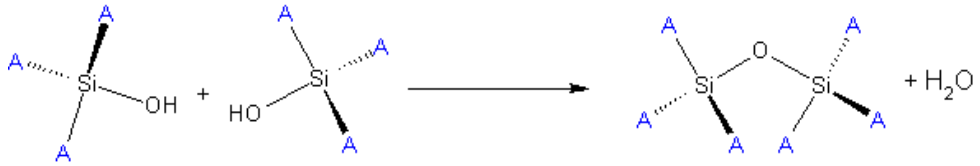

Figure 20: Reaction between silanols. "A" represents any other group, including bulk PDMS, glass, or any functional group. This mechanism allows both the bonding of activated PDMS to activated PDMS or glass, as well as covalent surface modification with silanes.

Mixing

Both on the macroscale and in the constrained flow of a microchannel, diffusion alone is a very slow process over any scale larger than a few μm, but mixing can be significantly accelerated by advection, or stirring, which reduces the lengths necessary for solutes to move from areas of high concentration to areas of low concentration.

Active mixing in a microfluidic system is defined as any process which requires an outside input, such as acoustic waves, applied fields, or pulsatile flows [223-225]. Such devices can be extremely efficient, though fabrication and operation may be more difficult. Passive mixers rely simply upon the topography and configuration of the channel to redistribute fluid in the channel. Depending upon the mixing strategy, these devices may operate at low Re, but many depend upon inertia and higher Re to function [226-231].

Though the lay definition of "chaos" is disorder and randomness, this is only the appearance of such a system, and not its true nature. Technically, "chaos" is a situation in which very small perturbations in initial conditions lead to very different outcomes [232]. As an example, consider stretching a piece of dough: two regions that were adjacent would become monotonically farther apart. However, when alternately stretched and folded in a baker's transformation, two such regions will become closer of more distant depending upon their original positions and the point in the mixing process. Non-chaotic advection results in linear changes in length scales [233], while chaotic processes achieve exponential changes, and thus such processes are extremely efficient mixing strategies [234]. In a chaotic system, two adjacent elements of fluid at an inlet end up well-dispersed: chaotic mixing reflects the most efficient redistribution of fluid [235-238].

A number of chaotic advection micromixers have been described [230, 239-241]. Among the simplest is the staggered herringbone mixer (SHM) from the Whitesides group [241]. Briefly, herringbone-shaped grooves in the floor of the channel force fluid from the center to the sides of the channel, ultimately producing circulation orthogonal to the primary flow axis. Because the vertex of these herringbones is offset from the center of the channel, fluid is transferred between the two sides. This offset alternates between sides of the channel with each set of grooves, transferring fluids across the centerline and disrupting the circulation centers on either side of the channel [233], ultimately producing the exponential stretching and folding characteristic of chaotic advection.

Advection, though helpful, is not required for mixing in a microfluidic system. Since it is a reduction in length scale that ultimately facilitates diffusive mixing, the small dimensions of microfluidic systems can be utilized to reduce this length in a controlled fashion. The typical method is focusing one fluid stream between others, either in 2 or 3 dimensions. Confining one or more species to the center of the channel ensures a relatively uniform velocity, limiting any differences in residence time and dispersion effects. Furthermore, complexation can be accelerated by sheathing a key reagent in a core of excess smaller reagent. By controlling the flow rates, the width of the focused stream can be reduced to nanometers for extremely rapid mixing [242], though this requires very high linear flow rates and, depending upon the setup, high shear forces. Sheath flow can produce a core of intermediate thickness, on the order of 15 – 30 μm, with considerably less effort [243]. Such an intermediately sized core has the advantage of complexation without significant dilution of the core reagent, as well as easier recovery of the product.

Application of microfluidics to the assembly of non-viral nucleic acid therapeutics is not novel. However, most previous investigations have only utilized microfluidics as a means of

controlling reagent ratios [26, 204, 208, 244], and those involving mixing only consider a single method, and do not observe the complexation within the device [203, 206-207]. To examine the actual impact of mixing, and it suitability for laboratory and clinical production of therapeutics, understanding the function of the device and its role in the complexation is essential.

Measurement techniques

Direct observation of complexes by atomic force microscopy (AFM) and transmission electron microscopy (TEM) give the most detailed view of the morphology, though adsorbed particles may not accurately reflect those in solution [173, 178, 184, 245-246]. Furthermore, because only a handful of complexes may be imaged at any one time, the information may not be representative of the full population, particularly if there is a large polydispersity. Microscopy is essential for a good understanding of the particles. However, while shape may play a role in *in vivo* behavior [33], size is a greater factor, and evaluating bulk characteristics is more important for clinical use than detailed morphology.

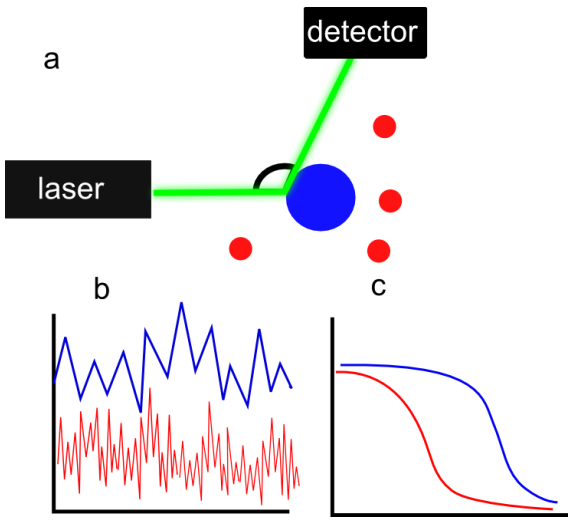

Figure 21: Schematic of DLS analysis. Polarized laser light is directed at a colloidal suspension, and is deflected by the particles (a). The signal received by the detector at a particular position is a result of constructive and destructive interference patterns from all particles in the volume, and it varies as the particles move (b). The rate at which the signal changes, the autocorrelation function (c), indicates the magnitude of Brownian motion,

and, therefore particle size. Signals from mixed populations are separated by analytical software, though the strong dependence of scattering intensity on particle size makes large contaminants a problem, and smaller particles more difficult to measure.

Dynamic light scattering (DLS) can yield information about the size distribution of the particles in a solution, and is a standard method for characterizing gene delivery particles and other nanoparticles (Figure 21). Laser light is scattered with an intensity proportional to the sixth power of particle diameter [247]. The autocorrelation of the scattered signal is measured over time to assess the rate of movement of the scattering species. The exponential decay of the correlation is evaluated to determine the motion of the scatterers, which gives the distributions of diffusive mobilities, leading to estimates of particle sizes. It does not, however, yield any information on particle shape. Furthermore, the scattering signal is relatively weak and sensitive to convection, so scattering cannot be used to monitor a complexation in a microchannel or during mixing.

Many groups have tried to observe the polyplex assembly progress, though with limited results. Stopped-flow studies are limited by the sensitivity of DNA to shear forces, though the early phases of interaction seem to take place in less than 50 ms [129, 248]. Detailed studies of the growth phase have been done with light scattering over a time scale of seconds to minutes, though the long time scale is likely due to slow transport [175]. Direct observation of single complexes via AFM has shown that they rearrange to achieve stability, though the technique requires adsorption to a substrate, which may hinder any kinetic information [173]. It is difficult to separate the actual complexation time from the limitations of mass transport, but the key points of the process appear to occur over a ms-to-s scale. Control of the mass transport in the system is tantamount to control of the complexation timing. Ethidium bromide is an intercalating dye with >10-fold fluorescence enhancement upon DNA binding [249]; between the charge neutralization and the stress of compaction on the DNA backbone, it is ejected upon complexation (Figure 22) [250].

Therefore, an ethidium bromide signal is a logical means of tracking DNA complexation; in a steady-state microfluidic device, location corresponds to timing, and, therefore, information about transport and process timing may also be revealed.

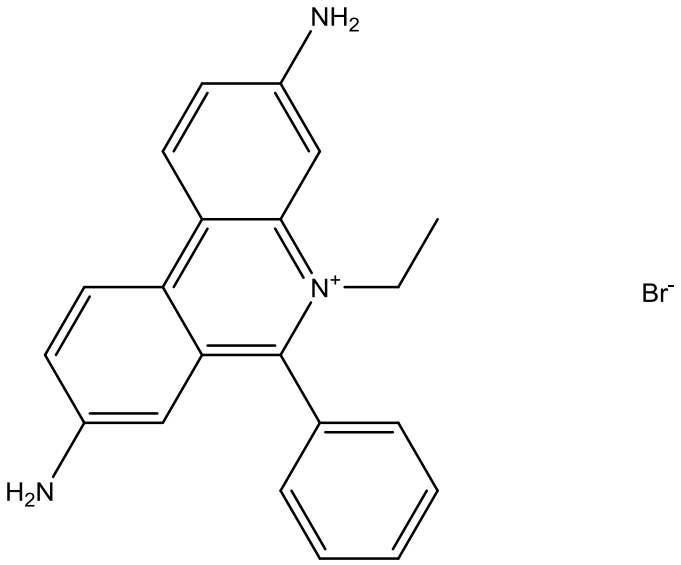

Figure 22: Structure of ethidium bromide. The molecule intercalates between the DNA bases, causing a 100-fold increase in fluorescence. Because intercalation distorts the structure of DNA, ethidium bromide is largely ejected upon complex formation, allowing tracking of free DNA and observation of complexation progress.

Computer Modeling

While partial differential equations like Navier-Stokes and mass transport describe microfluidic systems completely, many systems have no precise analytical solution. As a result, numerical methods, which produce solutions over a set of points to match the equations, are often required. Computational fluid dynamics (CFD) is a powerful method to predict fluid behavior in microfluidic systems. There are several methods for modeling [251-254], but the finite element method (FEM) is particularly useful and versatile. In a nutshell, the ruling partial differential equations (e.g. Navier-Stokes, Fickian diffusion) are reduced to a simpler set of ordinary differential equations. Multiphysics simulation is an indispensible analytical tool, because it can incorporate several interrelated phenomena,

such as fluid motion, mass transport, energy transport, and mechanical forces into a single model.

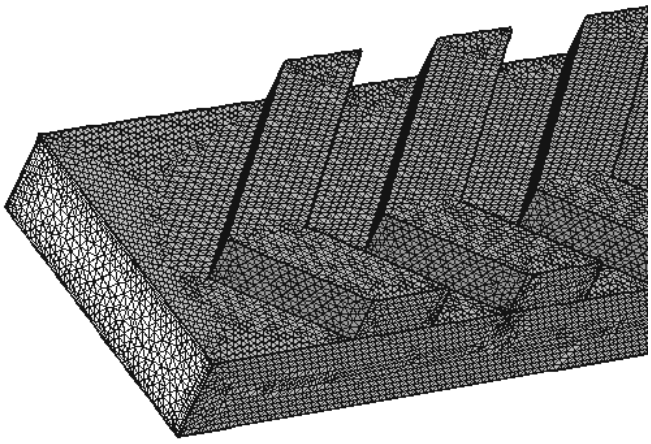

Figure 23: Image of the mesh of points in a COMSOL model of the SHM. The equations are solved numerically over this set of points, giving an approximate solution for analytically insoluble problems.

These models enable detailed analysis of a system prior to wet experiments, as well as prediction of phenomena not readily measured, such as the development of small eddies, force distributions, or the transient electric fields. However, there are limitations, and complete models of a system are often unattainable. The equations that define a system are solved for all variables over each point in the mesh (Figure 23), so going from a 1-dimensional model to a 3-dimensional model with similar resolution increases the degrees of freedom, and therefore the size and complexity, by a power of 3. Sharp gradients, as are often generated by large values of Pe or Da, require extremely fine resolution to arrive at a convergent solution without significant instabilities. Phenomena taking place over small length and time scales may have negligible effects on macroscale systems, but their importance in microfluidic systems require adequate simulation.

Just as FEM analysis simplifies a system of PDEs, many systems need to be reduced to their important elements prior to modeling. Reduction of the dimensions of the system and awareness of symmetry can make simulation much easier without significant loss of information. Calculation of dimensionless groups, such as Re, Pe, and Da elucidates the dominant forces in the system. Those parameters and phenomena that are less important can often be safely approximated. However, it is essential to remember that the quality of model is entirely dependent upon whether the equations, boundary conditions, and parameters passed to it, and the assumptions made during setup are valid and appropriate, and all models must be tested experimentally to assess their accuracy.

FEM modeling of the microfluidic systems allows prediction of behavior for better device design, as well as observation of behaviors not readily measured. Together these allow a better understanding of physical systems in advance of and beyond wet experiments.

Summary of work

Size is a crucial parameter for the bioavailability, efficiency, and reduction of adverse effects for any nanomedicine. Better control of size and reduction of polydispersity would increase the efficacy and safety, and potentially reduce both development and per-dose costs of such therapeutics. Therefore, examination and exploration of the mixing process as a means to better understand and control the size of their fabrication, which is kinetically sensitive, is both novel and of considerable value.

Using microfluidic systems, this investigation examines a system of DNA and PEI at clinically relevant concentrations to elucidate the importance of their physical interaction on nanoparticle properties. The strategies explored are accelerated mixing in a chaotic advection mixer (Aim 1), minimizing shear and variation of complexation conditions in sheath flow (Aim 2), and modifying transport *via* passive electrophoresis (Aim 3). The actual in-device complexation is monitored with ethidium bromide fluorescence, and the output of each device measured with DLS.

Aim 1: Mixing by Advection in the Staggered Herringbone Mixer

Introduction

The ideal DNA nanoparticles for clinical use would be relatively small (< 100 nm) [122, 255], of low polydispersity (near 0.1) [127], and with high reproducibility. While a high N/P ratio does produce smaller, more stable particles, excess polycations may contribute to toxicity [154-155, 171]. Therefore, though the N/P ratio must be well separated from charge equivalence, it must also be limited. This means that during mixing, it will take longer for all of the fluid to achieve the stability of a high N/P ratio. Clinically relevant concentrations also bias the system toward larger particles and aggregation [186-187].

The perfect conditions to produce small, uniform nanoparticles at high concentration and limited N/P ratio would be for the DNA and condensing agent to be mixed rapidly relative to the time scale of the interaction. However, the apparent complexation time is less than 50 ms, so this scheme would require a high-shear device such as those used for stopped flow kinetics [248], which is likely to damage longer pieces of DNA [256]. Nonetheless, any improvement in mixing time reduces variation in assembly conditions, and will produce a more uniform result.

The staggered herringbone mixer (SHM) is an efficient chaotic advection mixer that is simple to fabricate and operate (Figure 24, Figure 25) [241]. These characteristics have made it the subject of several analyses and variations [241, 243, 252-253, 257-262]. Though it is an effective mixer, the actual mix time and necessary operational parameters for an arbitrary system, such as DNA/PEI, had not been described. Such an analysis is necessary to evaluate mixer performance, and much of the following has been published in *Lab on a Chip* [261]. The practical aspects of using the SHM with the DNA/PEI system are then

presented, along with measurement of the complexation in the channel as a function of flow rate and the resulting polyplex size distributions.

Evaluation of SHM function

Before considering the more complex, interacting system of DNA and PEI, the performance and operational parameters of the SHM were explored via COMSOL modeling, a more general analytical model, and comparison with confocal micrographs of mixing at varying values of Re and Pe.

COMSOL model

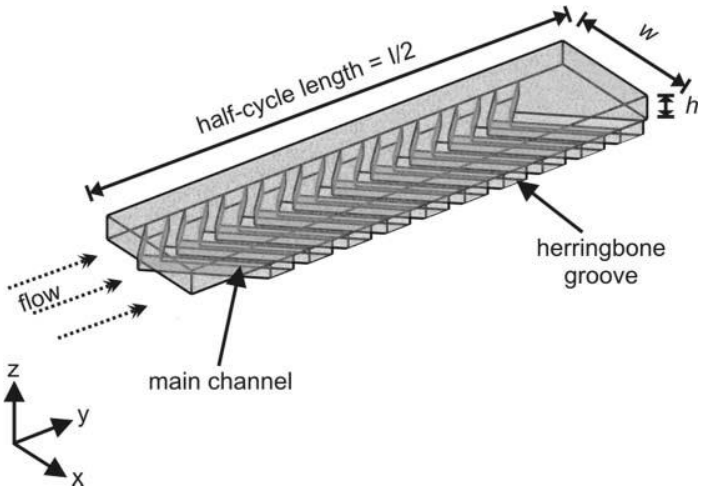

Figure 24: One half-cycle of the staggered herringbone mixer (SHM) [261]. The points of the grooves are offset 1/3 of the way across the channel. One complete cycle consists of two complementary half-cycles, with the herringbone grooves offset to opposite sides of the centerline. This was the functional unit used for modeling.

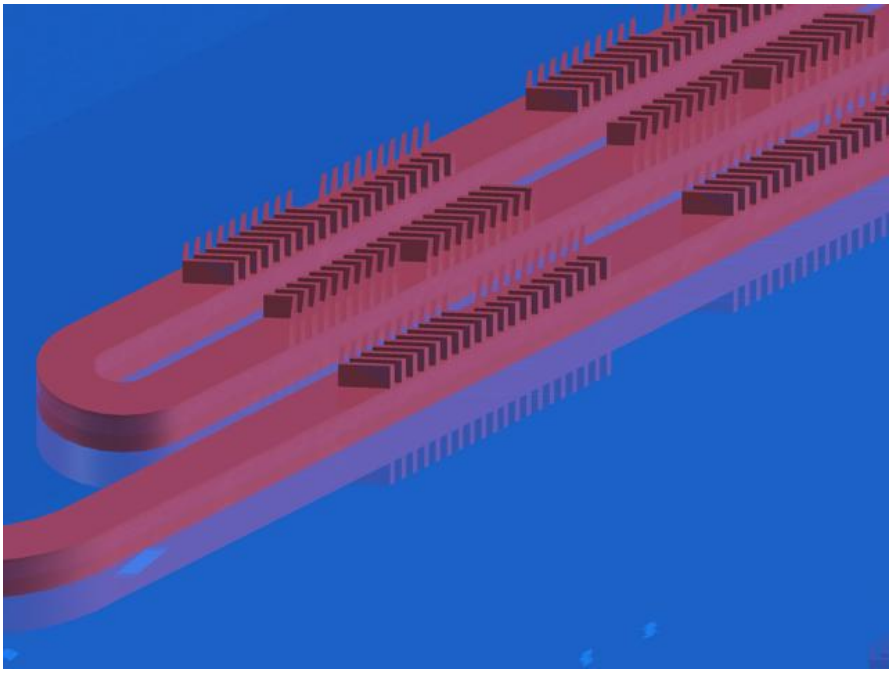

Figure 25: Rendering of an SHM channel, close up. The channel is 400 μm wide; depths are exaggerated by a factor of 5. The functional unit of the mixer is the paired half-cycles, and significant redistribution of fluid occurs after several complete cycles.

The flow rate behavior of the SHM was simulated assuming an incompressible Navier-Stokes (NS) model of a short section of the device (w = 410 μm in the across the channel x-direction, h = 80 μm in the vertical z direction, 700 μm in axial y-direction; 3 grooves 50 μm in the vertical z-direction and 85 μm in the axial y-direction) using COMSOL 3.3a software (COMSOL Inc., Stockholm, Sweden). The inlet condition (y = 0) was set to mimic fully developed flow, the outlet (y = 700μm) was set to no pressure, and all other boundaries had a no-slip condition.

Because the SHM functions by forcing fluid laterally across the channel, performance was evaluated as total flow across the channel (x-direction) normalized by flow along the channel axis (y-direction), $\frac{|v|}{u}$ (Figure 26, a). This ratio remained constant at flow rates below 1 μL/s (Re = 2.7), when the inertia is insufficient to overcome shear against the walls.

Slight deviation occurred when flow was increased to 5 μL/s (Re = 14), and a large drop in fluid deflection ($\frac{|v|}{u}$)

occurred above 15 μL/s (Re = 36). The reason for this can be seen by observing streamlines (not shown) or vorticity (Figure 26, b). At low flow rates, the fluid follows the grooves closely, with only small amounts of recirculation in the corners. As flow is increased, these small eddies break down, resulting in a slight dip in vorticity, and higher flow rates produce a larger recirculation in the grooves, reducing the relative volumetric flow rate through the grooves and decoupling the flow in the grooves from the flow in the main channel, producing less advection. For flow rates of less than 5 μL/s (Re = 14), behavior is relatively constant.

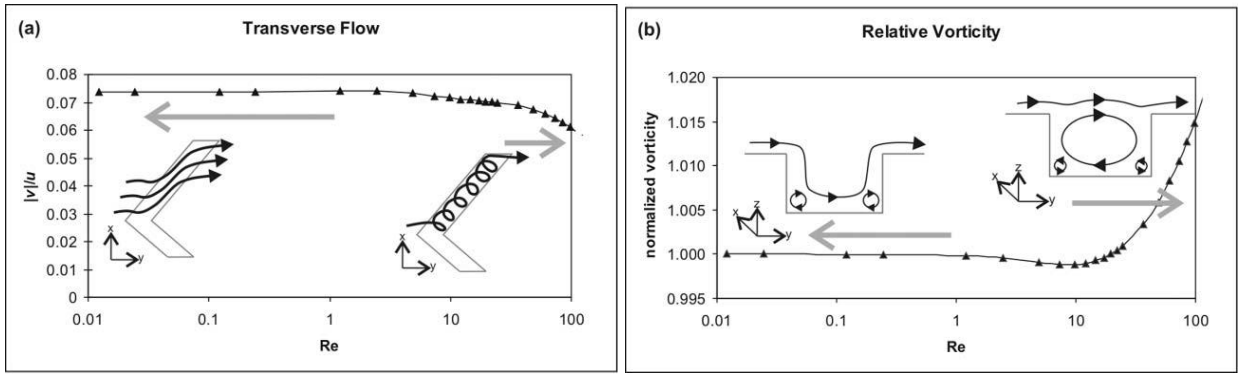

Figure 26: Evaluation of the SHM response to flow rate [261]. The ratio of velocity across the channel width (v, x direction) to velocity along the channel length (u, y direction) was used to quantify mixer function. Vorticity is defined as the curl of the velocity vector. Behavior is extremely consistent at low Re, where the viscous forces from shear against the walls dominates, but significant inertial effects such as recirculation begin to set in above Re = 5.

Because fluid behavior is dominated by the walls at low Re, the streamline position is constant and all velocities scale. Furthermore, the mixer behavior is relatively insensitive to the actual dimensions of the channel, within a certain range [252, 257, 262-264].

A complete model of the mixer was then produced in half-cycle segments (10 herringbones over 2 mm length, Figure 24). This division of the model into short sections was necessary

to reduce the degrees of freedom and produce faster, more detailed models. Three NS solutions were created: the first half-cycle, with fully developed laminar input at 30 μL/min (Re = 1.4), and an "even" half-cycle and an "odd" half-cycle, with input from a previous unit, to simulate all successive units. The fluid motion from the three NS units was then used for the convection vectors in the convection-diffusion mode (CD) to model solute motion. The first half-cycle had an input concentration profile of a smoothed step function with concentration from 0 to 1 at the channel midline, and successive half-cycles were modeled with the output from the previous cycle.

Pe was a limiting parameter for the models, so models were computed over a range of Pe = 6.25×10^1 to 3.10×10^6, with varying accuracy (Figure 31). Obtaining a good model of the DNA-PEI system, with Pe on the order of 10^6, was impossible directly. Adaptive mesh refinement was used to resolve the sharp gradients, but the exponential stretching of chaotic advection prevented convergence until artificial diffusion was employed. This condition facilitates convergence by adding diffusion where concentration gradients are steep, though it reduces the accuracy of the model in the case of high Pe. This additional diffusion overwhelmed the magnitude of native diffusion in the case of high Pe, so an alternative method was developed to estimate mixer performance [261].

Analytical model

Because the SHM redistributes fluid over the channel cross section efficiently, dispersion is significantly reduced; over the scale of one or more full mixing cycles, any solutes behave as though in plug flow [241]. Thus, the Poiseuille profile can be ignored, and the axial distance along the channel can be directly related to residence time as a function of flow rate; comparing the location in the mixer to expected diffusion length can give an estimate of mixing.

Consider two side-by-side inputs of solute and buffer at a particular distance along the mixer channel, where the fluids may be twisted and folded into thin layers. Mixing occurs when solute moves from one fluid to another, homogenizing concentration. This happens where and when the length scale of transport meets or exceeds the scale of the fluid layers in the y- and z- directions. Displacement by diffusion follows a normal distribution centered at 0, but the mean magnitude in one dimension, $\hat{L}_d$, is $\sqrt{2Dt}$. The probability that the distance which a solute in an arbitrary volume has diffused, L_d, not exceeding a particular distance, a, is

$$P(L_d < a) = \frac{1}{2}\left[1 + erf\left(\frac{a}{\hat{L}_d\sqrt{2}}\right)\right]$$

Equation 8: Probability of a diffusing solute traveling less than a particular distance, *a*.

When diffusing away from the fluid interface, the solute eventually encounters another, more distant interface (Figure 27, a-2). If a given layer is assumed to be flat and of thickness b, the mean minimum distance to an interface, $\hat{L}_i$, will be b/4. If the solute in an arbitrary volume element must travel a in one direction, the mean distance to the other interface would be $4\hat{L}_i - a$, and the resultant 2-sided probability function during mixing can be approximated as

$$P\left(-\left(4\hat{L}_i - a\right) < \hat{L}_d < a\right) = \frac{1}{2}\left[\text{erf}\left(\frac{a}{\hat{L}_d\sqrt{2}}\right) = erf\left(\frac{4\hat{L}_i - a}{\hat{L}_d\sqrt{2}}\right)\right]$$

Equation 9: Probability of a diffusing solute remaining within a fluid layer of mean thickness $4\hat{L}_i$ for an arbitrary distance *a*.

As the chaotic advection mixer stretches and folds the fluid, the distribution of L_i will also vary (Figure 27, b-1 to b-3). Before mixing begins, the fluids are of a single thickness with the interface halfway across the channel, $w/2$, and L_i is uniformly distributed between 0 and $w/2$. As the fluid moves down the channel, this distribution will move toward 0,

producing a simple delta function at 0 for infinite mixing. This suggests that L_i may follow an exponential distribution

$$p(L_i = a) = Ae^{\frac{-a}{L_i}}$$

Equation 10: Presumed distribution of L_i at a given position in the mixer.

Combining the distributions of L_d and L_i (Equation 9, Equation 10) and integrating over all a during mixing (where $\hat{L}_d > \hat{L}_i$) yields

$$P(L_d < L_i) = \frac{1}{2} erf\left(2\sqrt{2}\,{\hat{L}_i}/{\hat{L}_d}\right) \approx 1.60\ {\hat{L}_i}/{\hat{L}_d}$$

Equation 11: Probability of a solute not crossing the interface, relative to $\hat{L}_d$ and $\hat{L}_i$.

This relationship describes the likelihood that the solute has *not* crossed the interface, and will vary from 0 to 1 as mixing proceeds, so it will be of similar magnitude to the coefficient of variation (CV) and the two values will be comparable, particularly as the system approaches infinite mixing.

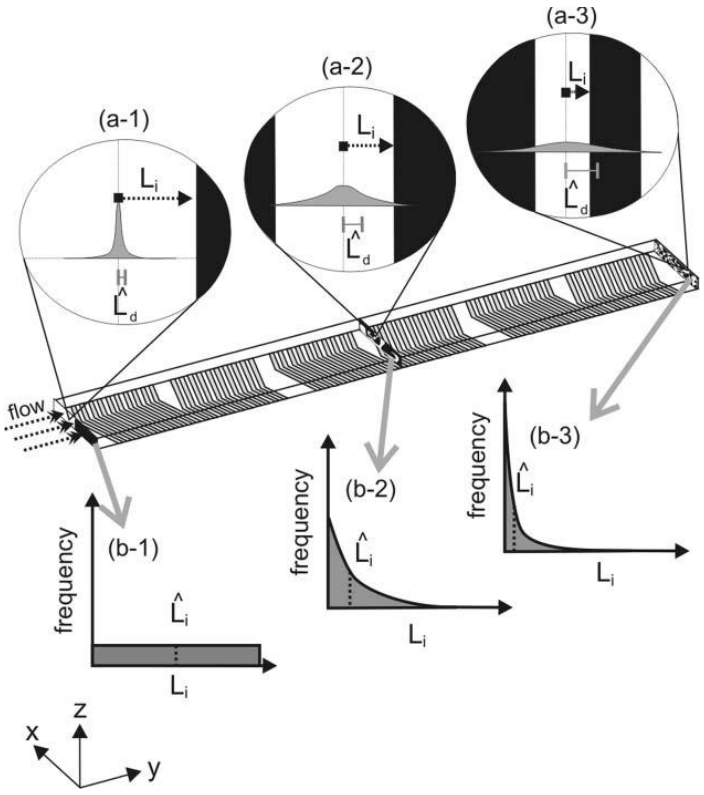

Figure 27: Schematic of the mixing theory of the SHM [261].

Analysis of the SHM is simplified by several factors unique to chaotic advection micromixers. Firstly, the efficient redistribution of fluid across the channel cross section virtually eliminates the effects of the Poiseuille flow profile [241], and the downstream position in the channel (y-direction) can be directly related to residence time. Secondly, below Re = 14, the streamlines in the mixer are independent of flow rate, and so fluid geometry (e.g. layer thickness, x- and z-directions) is a function only of axial position (y-direction). This means that mixing can be expressed as a relationship between flow rate, diffusivity, and position—or simply Pe and downstream position, I (in cycles) and d (length per cycle). Thus, the analytical model (Equation 11) may be restated as

$$P(L_d < L_i) \approx 1.60 \sqrt{\frac{Pe}{wld}} \hat{L}_i$$

Equation 12: Probability of a solute not crossing the interface , dependent upon Pe, channel width *w*, position in mixer *l* (in cycles), length per cycle *d*, and $\hat{L}_i$.

To relate this theory to the SHM, a relationship between *l* and L_i was derived from COMSOL models. Concentration profiles from each half-cycle segment were exported and evaluated in MATLAB R2007a (The MathWorks Inc., Natick, MA). Pe = 6.25×10^4 was used to obtain the clearest interface with a minimum of distortions and errors. An algorithm was written to identify the local maxima in concentration gradient, which was assumed to be the interface (x-z plane, Figure 30, c). The program then located the distance to the nearest interface, L_i, for each point in the channel cross section.

Prior to one full cycle of mixing, the MATLAB algorithm did not identify enough interface points for analysis, and too many points were identified beyond 4 cycles (approximately 1 in 7 pixels) and the layer thicknesses approached the mesh size of the COMSOL source models, 2.5 μm. Histograms of L_i appeared to follow an exponential distribution as described in Equation 10 for all data sets, and quantile-quantile plots of the COMSOL output with exponential models confirmed a good fit (R = 0.98 ± 0.02, not shown).

As expected for a chaotic mixer, $\hat{L}_i$ decreased exponentially with mixer length between cycles 1 and 4, $\hat{L}_i = 19.7e^{-0.55l}$ ($R^2 = 0.994$, not shown). Prior to one full cycle, the slope was steeper, as layers had not yet formed, and the model was not a good descriptor of the region. Beyond cycle 4, the slope was shallower as the resolution of the model was approached. Neither the algorithm nor the COMSOL model could keep pace with the rapid expansion of the interface. Combining this empirical expression with the analytical model

$$P(L_d < L_i) = 0.027\sqrt{\frac{Pe}{l}}e^{-0.55l}$$

Equation 13: Probability of a solute not crossing the interface, dependent upon Pe and position in the SHM.

For a mixing threshold of $P(L_d < L_i) = 0.1$, this gives $Pe \approx 13.6 l_{0.1} e^{1.1(l_{0.1})}$. Despite the mixed form, this can be approximated as a direct logarithmic relationship without significant deviation at low Pe suggested by other studies [240-241].

$$l_{0.1} = 1.73 \log(Pe) - 2.16 \ (R^2 = 0.998)$$

Equation 14: Length of SHM, in cycles, required to achieve the 0.1 mixing threshold, simplified.

Experimental confirmation

The COMSOL models and theoretical analysis were tested by confocal microscopy. The SHM was produced by soft lithography following the design and protocol of Stroock *et al.* [241]. Briefly, the master mold was fabricated by 2-layer SU-8 photolithography on a 3" silicon wafer. Devices were then cast in Sylgard 184 polydimethylsiloxane (PDMS), and bonded to a conventional #1½ 24 mm x 60 mm glass cover slip via oxygen plasma treatment (Figure 28). Fluidic connections were made with ports made of 3/32" x 1/32" silicone tubing embedded in PDMS, plasma bonded over holes punched in the PDMS layer. Solutions were loaded via 1/16" x 0.010 fluorinated ethylene propylene (FEP) tubing from two 1 mL gas-tight glass syringes driven by a Harvard Apparatus model 22 syringe pump at 3 μL/min – 300 μL/min (Re = 1.2×10^{-1} – 1.2×10^{1}, Pe = 8.33×10^{2} – 8.33×10^{5}). Measurements via confocal microscopy showed the channel to be 392 ± 4 μm in width (w) and 56 ± 2 μm in height (h), with grooves recessed 36 ± 2 μm into the channel floor for a total depth of 92 μm. Each 3.5 mm mixing cycle consisted of two half-cycles of 10 grooves, and 7 such cycles were positioned along each of three 25 mm passes of the channel across the slide, for a total of 21 full cycles.

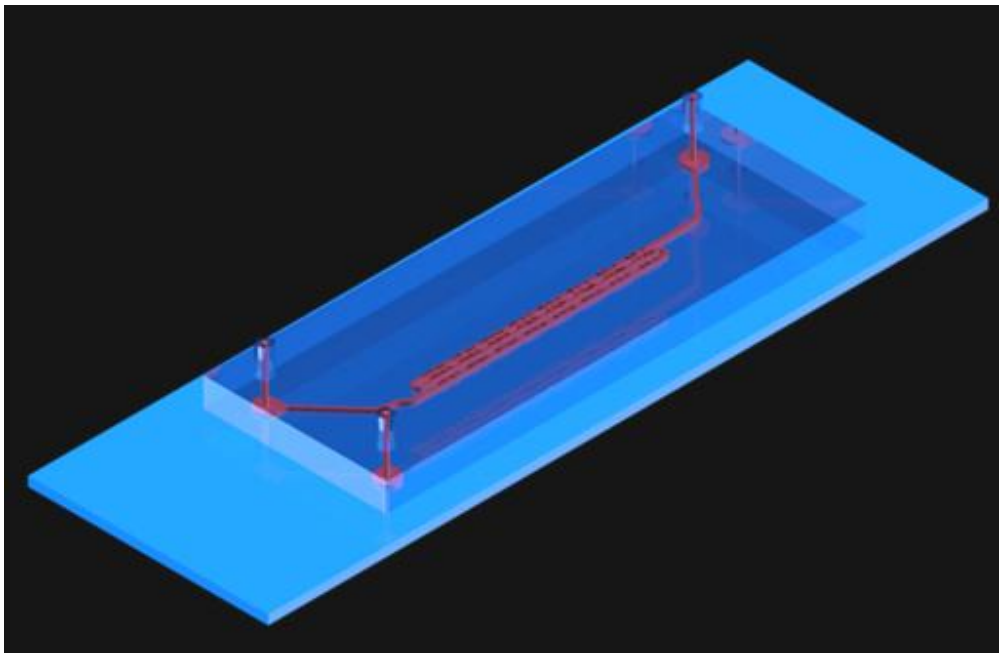

Figure 28: Schematic of SHM design. The actual device has 2 inlets and one outlet, and features three passes of the channel across the slide with a total of 21 full mixing cycles. The blue layer is a conventional glass microscope slide, and the red represents the channel volume. Silicone tubing was cured into the PDMS as fluidic ports.

Figure 29: Side view of a rendering of the SHM. The device consists of a PDMS layer, with embedded silicone tubing, bonded to a glass microscope slide. The channel (red) is defined by the PDMS and glass surfaces.

For confocal microscopy, devices were loaded with 0.05 M sodium borate buffer, pH 8.5, and one of three solutes: fluorescein (MW 0.4 kDa) or fluorescein-conjugated dextrans (MW 40 kDa or MW 2000 kDa), all diluted to 10 μM with respect to fluorescein content. Imaging took place on a Zeiss LSM510 laser scanning microscope at the University of Washington Nanotech User Facility, with a pixel resolution of 0.90 μm x 0.90 μm x 1.50 μm. Images were converted to grayscale and analyzed in ImageJ, and further data analysis was

completed in Excel. For fluorescence data, only the central 350 μm x 45 μm was evaluated to reduce edge effects.

Despite minor differences between the device dimensions and the COMSOL model, there was no impact on the qualitative appearance of the flow (Figure 30, a and b). As expected, both confocal and COMSOL results showed that the geometry of the flow was independent of flow rate over the range tested (Re < 12), and solute position depended only upon l and Pe. As mixing progressed, CV decreases from 1 to 0 (Figure 31). The COMSOL data showed an exponential decay, with a slope dependent upon Pe. An apparent oscillation in the data was an artifact of processing, as the mean concentration showed similar variation. If such an oscillation were due to the segmented construction of the model, the expected period would be one full cycle, rather than the one and one-half seen at higher Pe. The confocal data did not show this variation, and showed similar exponential behavior until reaching baseline at CV = 0.08. The primary contributor to this baseline is non-uniform intensity due to edge effects in the channel. To minimize this effect, only the central region of the channel was analyzed. Further reduction of the measurement region would reduce data accuracy, and averaging techniques would exacerbate any overstatement of mixing due to unstable flow from the syringes at low flow rates but would not alleviate spatial variation near the channel walls.

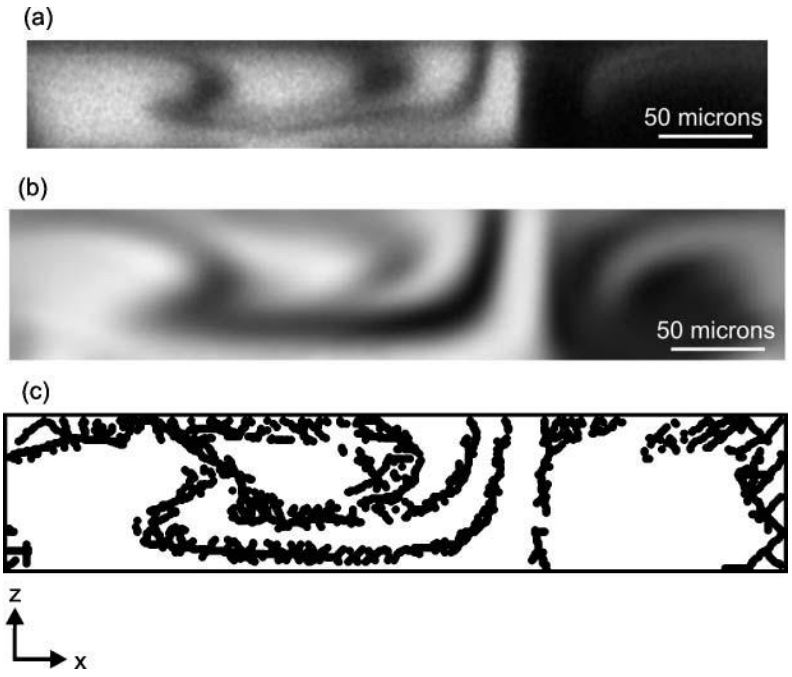

Figure 30: Confocal micrograph of fluorescein-dextran in the SHM (a), along with COMSOL model of mixing (b) , and MATLAB labeling of the fluid interface (c) [261].

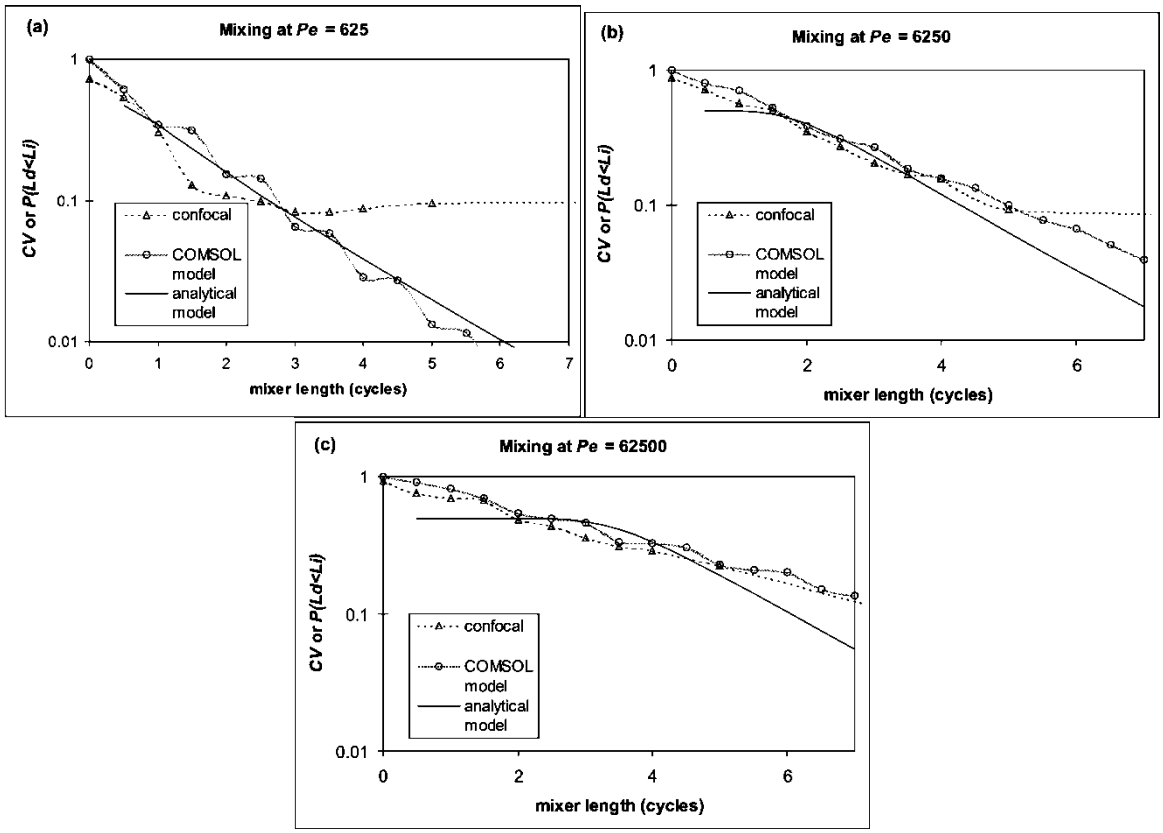

Figure 31: A comparison of models of mixing in the SHM at varying values of Pe, along with measurements from confocal microscopy [261]. Confocal measurements and COMSOL results reflect the CV, while the analytical model shows the probability of diffusion exceeding fluid layering, $P(L_d<L_i)$.

One of the most valuable pieces of information in device design is the required length of a mixer. To match the data range available from confocal measurements, the cutoff considered for mixing was CV = 0.1, and the mixer length necessary to achieve this threshold, $l_{0.1}$, was extracted from the mixing traces. Estimates of $l_{0.1}$ were similar between the COMSOL models and confocal data (Figure 32). Some spread could be seen in replicates in the confocal data, taken with different combinations of solute and flow rate to achieve the same Pe, due to the unstable flow at low flow rates. This variation in interface position resulted in slightly lower estimated mixing distances overall for confocal than predicted by COMSOL. For both methods, $l_{0.1}$ appeared to increase linearly with log(Pe), as predicted [241], until Pe reached 6.25×10^5, when it leveled off. However, fluid layering thinner

than the minimum resolution (0.9 × 1.5 μm pixel size for confocal, 2.5 μm mesh size for COMSOL) could not be distinguished. Furthermore, each technique also overstated diffusion near the interface: the unstable flow in the confocal experiments, and the artificial diffusion in COMSOL, which would have overwhelmed thin layers and native diffusion. This indicates that direct measurement or modeling of mixing is currently limited to Pe < 6.25×10^5. To extend such experiments to higher Pe, significant improvements in resolution for confocal microscopy or finer meshing in COMSOL would be required.

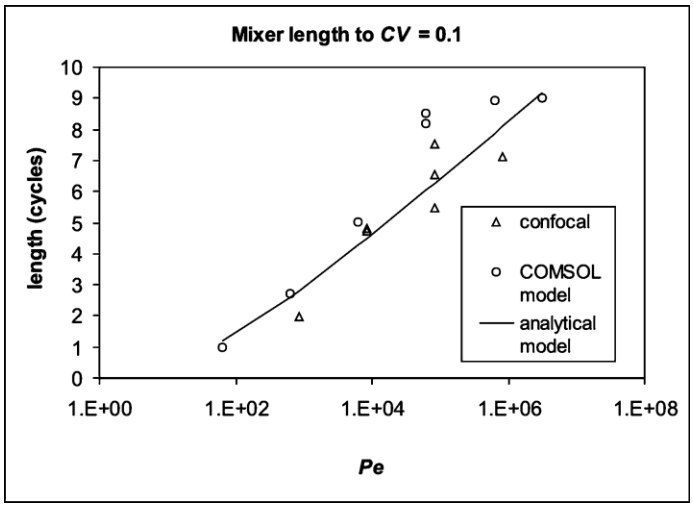

Figure 32: Required SHM length as a function of Pe, measured from COMSOL models and confocal measurements, and compared to the prediction from Equation 14 [261].

With an understanding of the behavior of the SHM and the implications of Pe, the kinetics of mixing for any particular system, such as DNA-PEI, can be estimated. Mixing time is of particular importance. Because the PEI is in excess in the system, mixing should be assessed relative to its concentration. Equation 14 can be used to calculate the mixer length required for a particular system for which D is known.

$$l_{0.1} = 1.73[log(Re) - log(D)] - 11.8 \text{ cycles}$$

Equation 15: Required mixer length to achieve the mixing threshold in a particular system, dependent upon axial (y-direction) velocity.

For 25 kDa branched PEI, with diffusivity on the order of $1x10^{-11}$ m^2/s, $l_{0.1}$ = 10 cycles for the highest predictable flow rate (Re = 15). This suggests that the PEI completely mixes with the DNA within the device over the complete operational range of the SHM, so the complexation is fully completed within the channel. Because mixing time is a function of flow rate, a range of times and their effects on complexation can be explored using the SHM.

Mixing time of DNA/PEI

Because the complexation of DNA and PEI is dependent upon the kinetics of the interaction between DNA and PEI, which are in turn dependent upon transport--both advection and diffusion--the effects of mixing time should be examined. The models derived above suggest that, for the operational parameters of the SHM and a species as large as 25 kDa branched PEI, $t_{0.1} > 120$ ms (Figure 33). Though this is longer than the estimated time of interaction [248], this time scale is similar to the scale of complexation, and changes to the mixing speed are therefore expected to affect the process and its outcome.

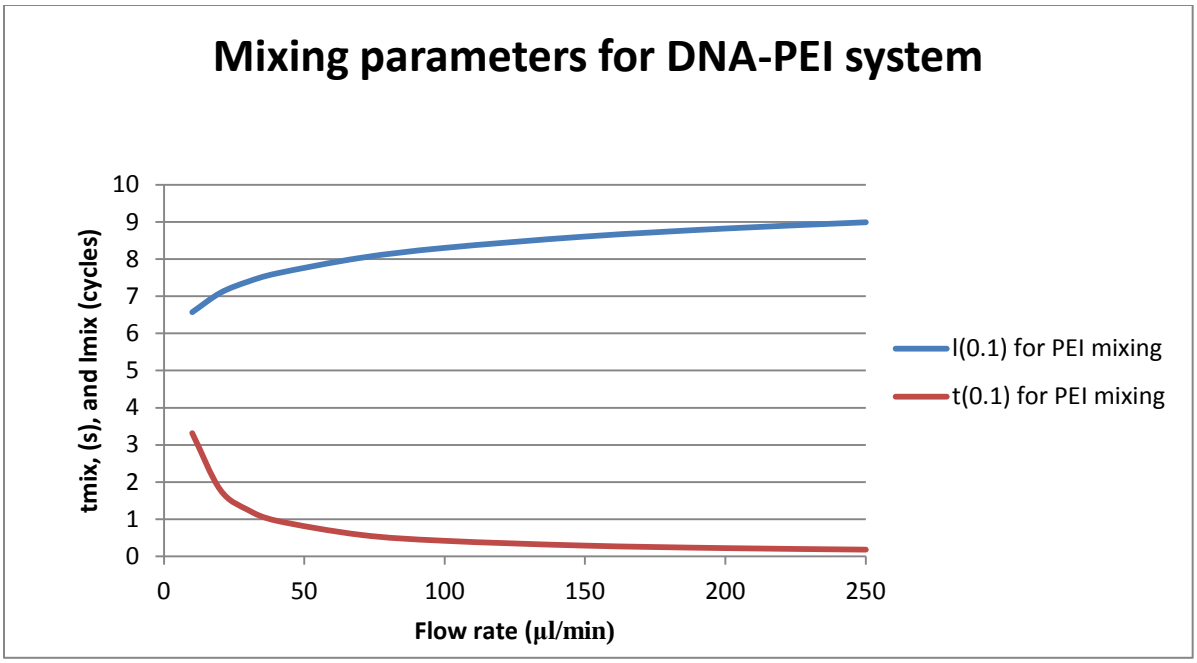

Figure 33: Plot of $l_{0.1}$ for 25 kDa branched PEI in the SHM, calculated from Equation 15, and the resulting mixing times. Flow rates correspond to 0.41 < Re < 10.4.

Challenges of complexation in a microchannel: Precipitation

Initial work involving 5.6 kbp plasmid DNA (gWiz-GFP, Aldevron, Fargo, ND) and 25 kDa branched PEI, at a concentration of 75 µg/ml DNA and an N/P ratio of 6 in 10 mM HEPES buffer, pH 7.5 demonstrated the challenges of using a microchannel for a condensation process. Though fluids are efficiently redistributed around the channel cross-section, the flow profile is not significantly perturbed from the standard Poiseuille flow profile. The fluid has a large residence time near the walls, particularly in the small dimensions of the grooves, and this residence time is longer than the time scale of complexation. Where the fluid interface is adjacent to a wall, material may build up in regions of steady-state charge equivalence (Figure 34). This accumulation, which occurs both on the PDMS and glass

surfaces, degrades mixer function in an unpredictable way by blocking flow in the grooves, and is likely responsible for the production of larger aggregates.

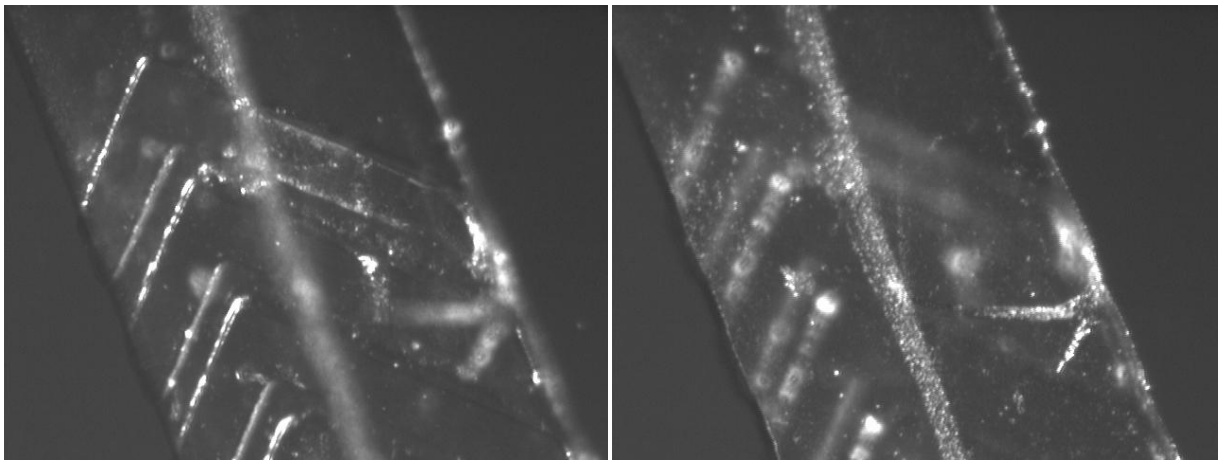

Figure 34: Images of precipitation in the grooves and on the glass of the SHM. The central stripe on the glass reflects the location of the interface between the DNA and PEI solutions.

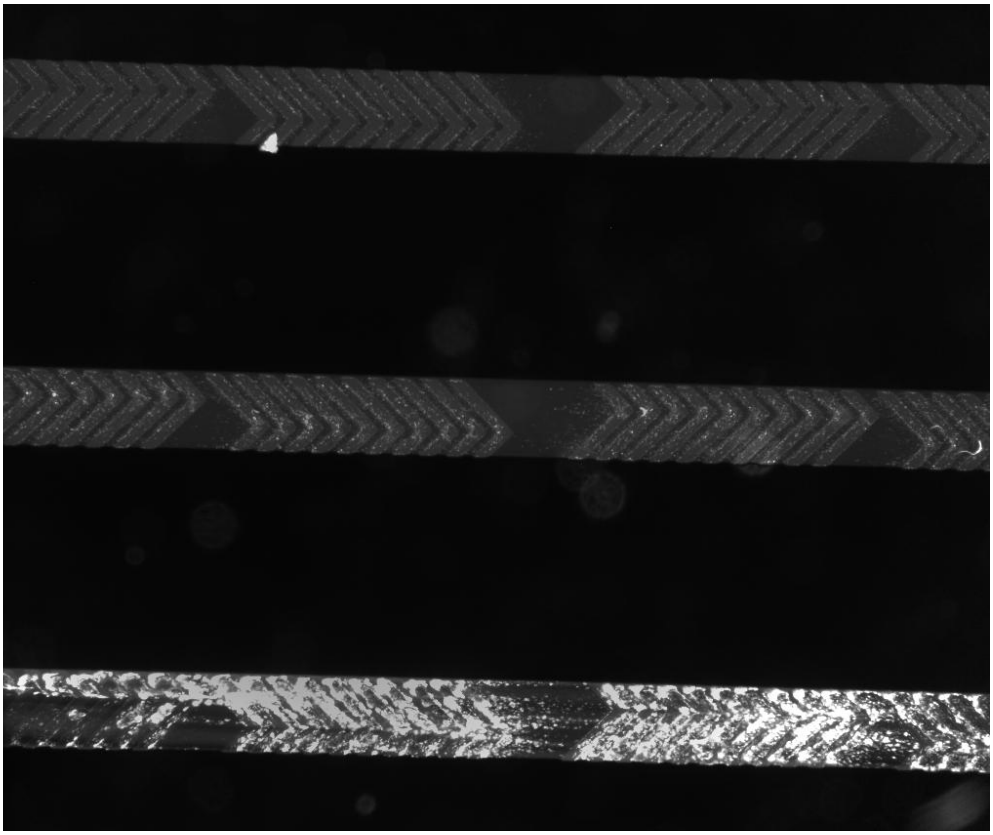

Figure 35: Aggregation of plasmid DNA (75 μg/mL) and PEI (N/P = 6) in the SHM. Flo w is from left to right in the bottommost channel, proceeding right to left in the middle, and left to right again in the topmost channel.

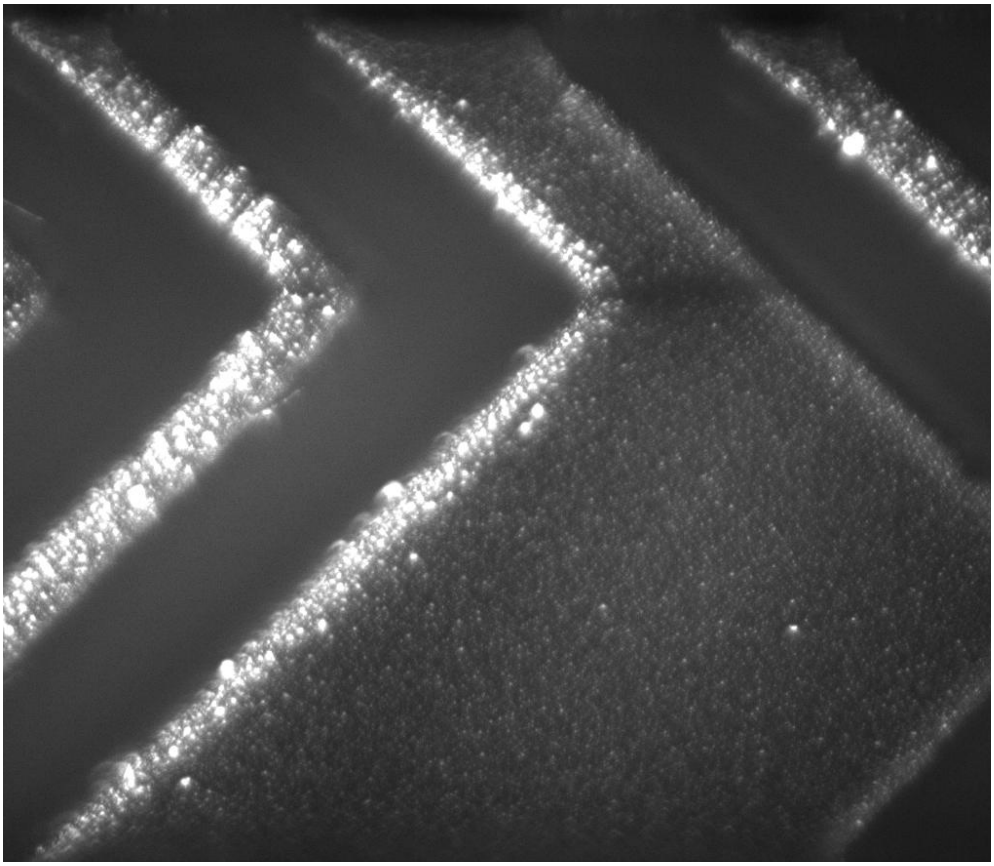

Figure 36: Aggregated material near the end of an SHM treated with PEG-silane. 75μg/mL plasmid DNA and branched PEI (N/P = 6) were used in this experiment.

Furthermore, the magnitude of this aggregation (Figure 35) is sufficient to significantly deplete the DNA from the solution, which, given the necessary dose for clinical applications [160], is a serious concern. Because the ethidium bromide is not ejected from these larger aggregates, it also swamps the fluorescence signal from the solution. The extremely high surface area-to-volume ratio of a microchannel is clearly prone to increasing surface interactions, and the efficient redistribution of fluid over the cross section (x-z plane) of the SHM ensures that all of the fluid comes within close proximity to the channel walls within a few cycles of mixing. While PDMS is known for fouling, due to its hydrophobicity [212-213, 220] and the formation of DNA nanoparticles is dominated by hydrophobic forces [161,

164], deposition of material occurred even on the hydrophilic glass surface (Figure 34), and PDMS modified with PEG-silane, which produces a hydrophilic surface and reduces non-specific interactions (Figure 36). In lower quantities, the preferential deposition of this material on the downstream edges of the grooves is obvious (Figure 36). This indicates that the aggregation is not entirely due to interactions with a hydrophobic surface, but that the physical presence of a surface itself produces the conditions for aggregation. The higher flow, with fluid from both the main channel and grooves converging, results in a higher mass flux over the surface, which provides a greater amount of material for interaction and deposition. Additionally, high shear tends to elongate large polymers, such as plasmid DNA and 25 kDa PEI [129], increasing the surface area and extending the interaction time, and opportunity for crosslinking with other charged polymers (Figure 35, Figure 37). Each additional molecule incorporated into the aggregate increases the likelihood of additional interactions and adhesion, and together, these effects contribute to the creation of visibly large aggregates. This phenomenon may be for similar reasons as the preferential formation of bacterial biofilms under similar conditions [265], or may be related to other nuances of fluid dynamics [266]. Nevertheless, this behavior prevents fluorescence measurements of DNA complexation, due to increasing background signal, and is not desirable for preparation of DNA nanoparticles, due to depletion of DNA from solution and potential production of larger aggregates in the product.

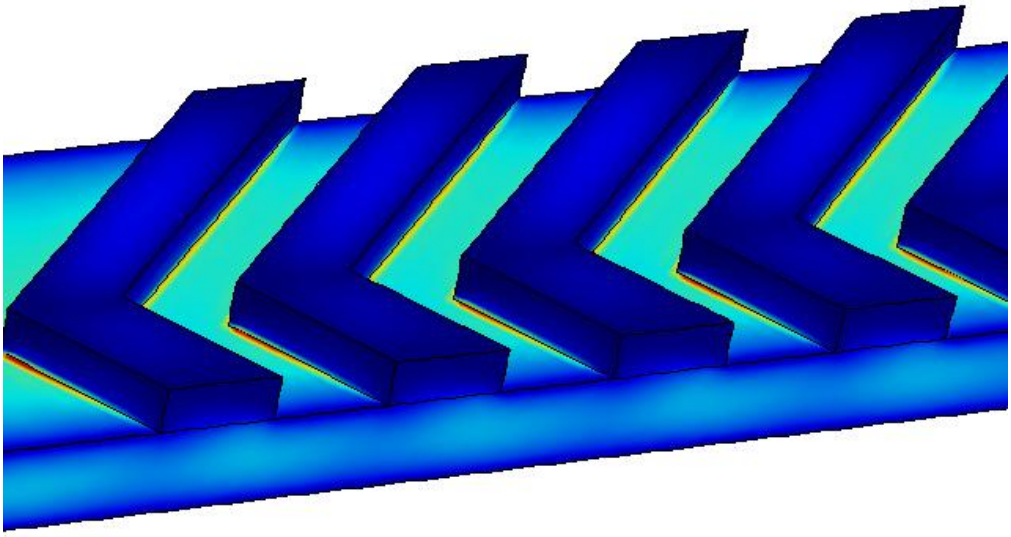

Figure 37: COMSOL model of shear on the SHM surface. Shear is low in the grooves, due to low flow rates, but highest where the grooves meet the channel, particularly on the downstream edge.

The initial experiment parameters, 75 μg/ml plasmid DNA and 25 kDa branched PEI at a ratio of N/P = 6, are within the useful range for laboratory preparation of gene delivery agents, though even this is low for clinical utility [267]. However, as the precipitation is unsuitable for analysis and undesirable for nanoparticle preparation, this formulation is incompatible with the SHM, even when the surface is modified with PEG-silane. Replacing the 5.6 kbp plasmid DNA with 22 bp oligo (Integrated DNA Technologies, Coralville IA) DNA mimics siRNA or μRNA, useful for gene regulation, rather than gene transfer, and significantly reduces the likelihood of intermolecular and surface interactions. Furthermore, in addition to PEGylation of the SHM surfaces to prevent deposition, a PEG-modified PEI (25 kDa PEI with two 5 kDa PEG subunits, provided by Dave Chu) also reduces interactions between complexes [268]. These measures effectively reduce, but do not entirely eliminate, buildup of material in the SHM (Figure 38). Nevertheless, this is sufficient for analysis.

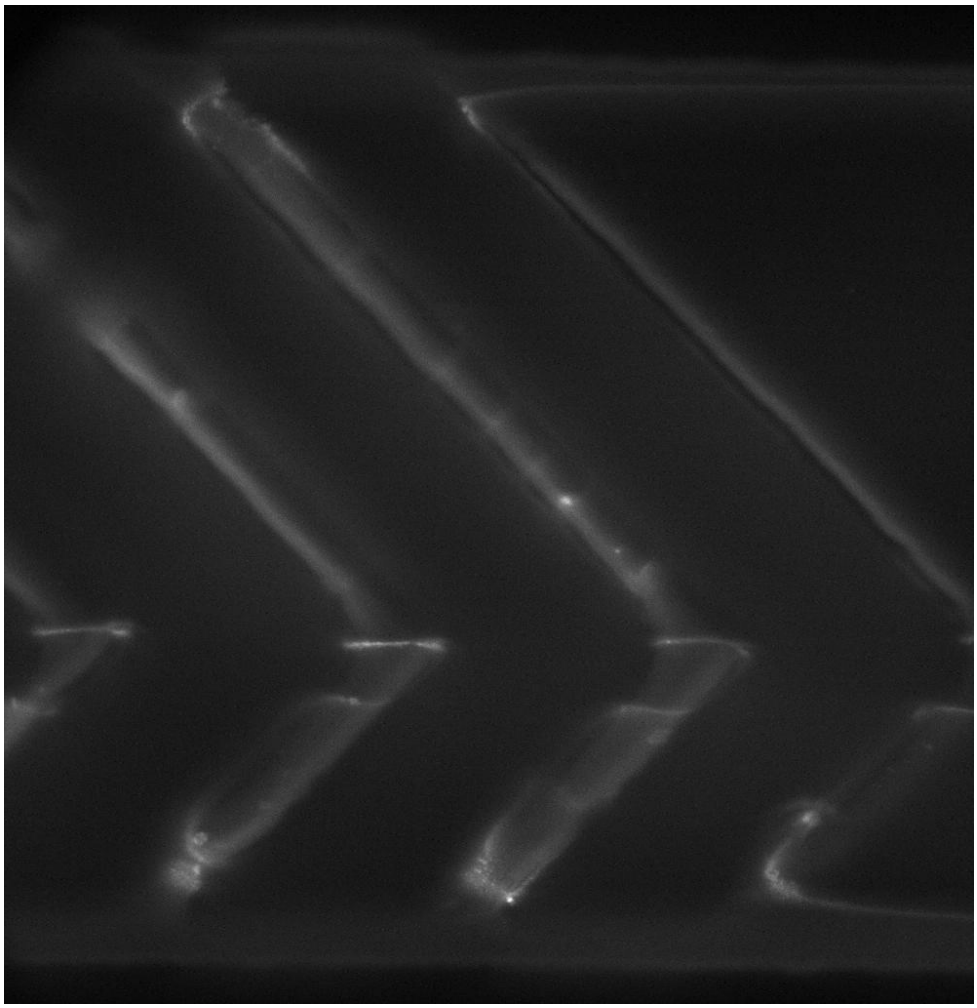

Figure 38: The greatest extent of aggregation seen in the SHM, near cycle 3, under low-fouling conditions (oligo DNA, 20 μg/mL, PEG- PEI, n/P = 6, and channel treated with PEG-silane). The bright stripes near the vertex of the grooves are aggregated material; other bright zones are from defects in the SU-8 master mold.

Impact of mixing time on DNA complexation

20 μg/ml oligo DNA was mixed with PEG-PEI at an N/P ratio of 6, in 10 mM HEPES buffer, pH 7.5 at a range of flow rates. The analytical model predicts that mixing with respect to PEI should occur between 6 and 8 cycles as flow rate is varied between 15 μL/min and 180 μL/min, corresponding to a mixing time reduced from 2.6 s to under 300 ms. Though this is still more than 6 times larger than the estimated complexation time [248], such a difference should have measurable impact on complexation kinetics.

Though the lower concentration of oligo DNA and the PEGylation of both the channel surface and PEI significantly reduce fouling, some buildup of material still occurs, resulting in a variable background fluorescence signal. Nonetheless, it is apparent that the complexation of DNA and PEI occurs predominantly between mixing cycles 2 and 4, regardless of flow rate (Figure 39), where the mean layer thickness is reduced from 6.6 µm to 2.2 µm, according to the COMSOL models. The exponential nature of chaotic advection, combined with the discrete mixing units, masks any variation in mixing length from flow rate, though the time for the fluids to mix by cycle 4 is still entirely dependent upon this parameter, ranging from 1.7 s at the 15 µL/min to 140 ms at 180 µL/min, approximately 40% faster than predicted by the analytical model. Mean diffusion length for an oligo by cycle 4 ranges from approximately 1 µm to 3 µm over those flow rates. This suggests that transport in this system is not due to diffusion alone, and other forces, likely related to electrostatic charge and the liquid junction potential (Aim 3) have a significant impact.

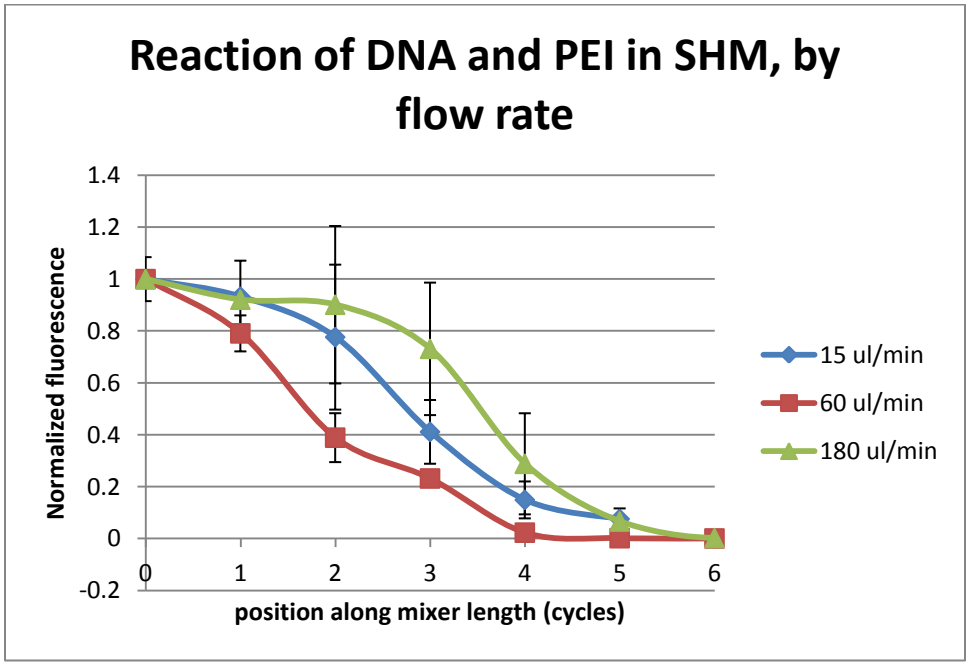

Figure 39: Disappearance of fluorescence signal from ethidium bromide during complexation of 20 µg/ml oligo DNA with PEG-PEI at N/P = 6 in the SHM at varying flow rates (n = 3). Traces are normalized to inlet

intensity, and error bars represent standard deviation. The relatively high variability indicates moderate buildup of fluorescent aggregated material during analysis. Complexation occurs predominantly between 2 and 4 mixer cycles for all flow rates.

To obtain a good signal for dynamic light scattering, the concentrations of oligo DNA were doubled to 40 μg/ml, with a corresponding increase in concentration of PEG-PEI to maintain an N/P ratio of 6. Even so, the signal intensity is low, due to small particle size, producing a fairly large variability in measurements. Despite the relatively large range of mixing time, no significant trend in either size (Figure 40) or polydispersity (not shown) can be seen. However, there is a clear reduction in size resulting from rapid mixing, either *via* SHM or pipette, relative to a smooth channel. The smooth channel, which had similar dimensions to the SHM, allowed a longer interaction time prior to mixing, producing significantly larger particles. This difference suggests that the complexation may occur via nucleation and growth [178], though only over time scales larger than produced in the SHM. Regardless, the small and relatively insensitive particle size is predominantly regulated by the steric hindrance of a large number of intermolecular interactions by the PEGylated PEI.

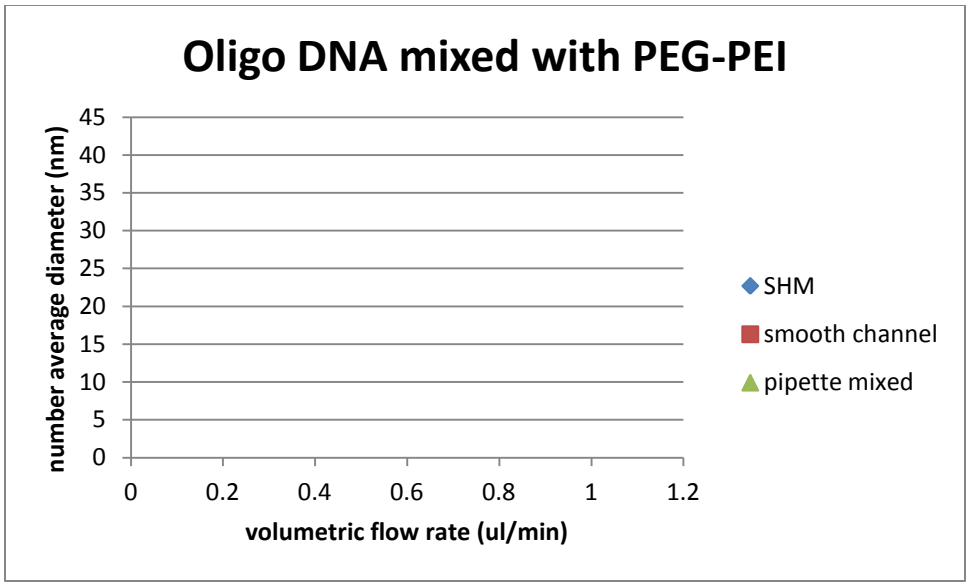

Figure 40: Number average size of DNA nanoparticles, measured by dynamic light scattering. Error bars represent the standard deviation of measurements (n = 9). To attain a stronger signal, the concentration of DNA was doubled relative to other experiments, to 40 µg/ml. Though no statistically significant trend can be discerned from mixing time in the SHM, due to the regulation of particle size by the PEGylated PEI, the mixer does produce consistently smaller nanoparticles than a smooth channel of similar dimensions, and less variability than pipette mixing. Particles prepared by pipette mixing are not associated with a particular flow rate, but are included in the graph for comparison.

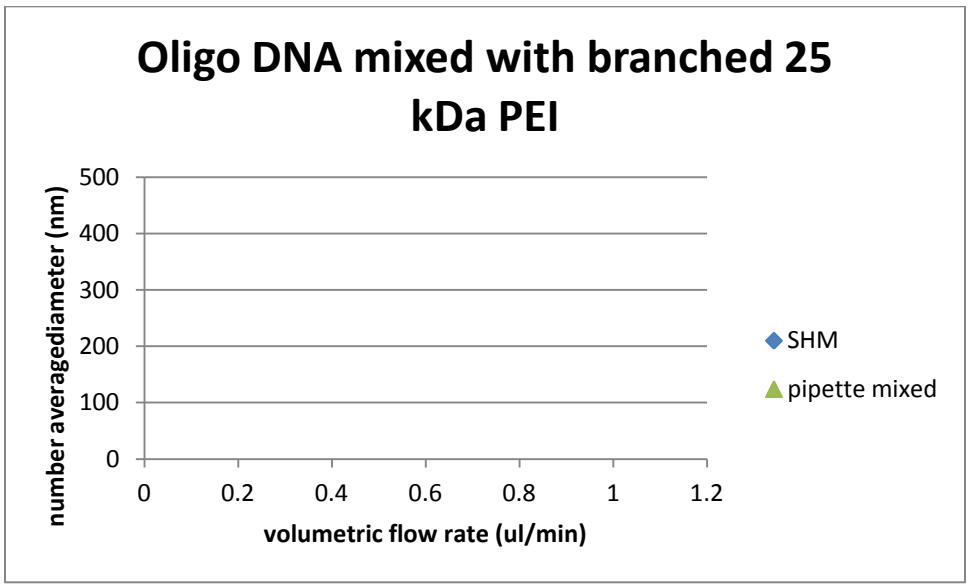

Figure 41: Size measurements of nanoparticles prepared from 20 µg/ml oligo DNA with non-PEGylated PEI in the SHM. Error bars represent the standard deviation of measurements (n = 9). Without size regulation from PEG, the particles are significantly larger, and a weak trend can be seen showing smaller particles with increasing flow rate. Pipette mixing is not associated with a flow rate, but is included to show the significant reduction in size and variability from use of the SHM.

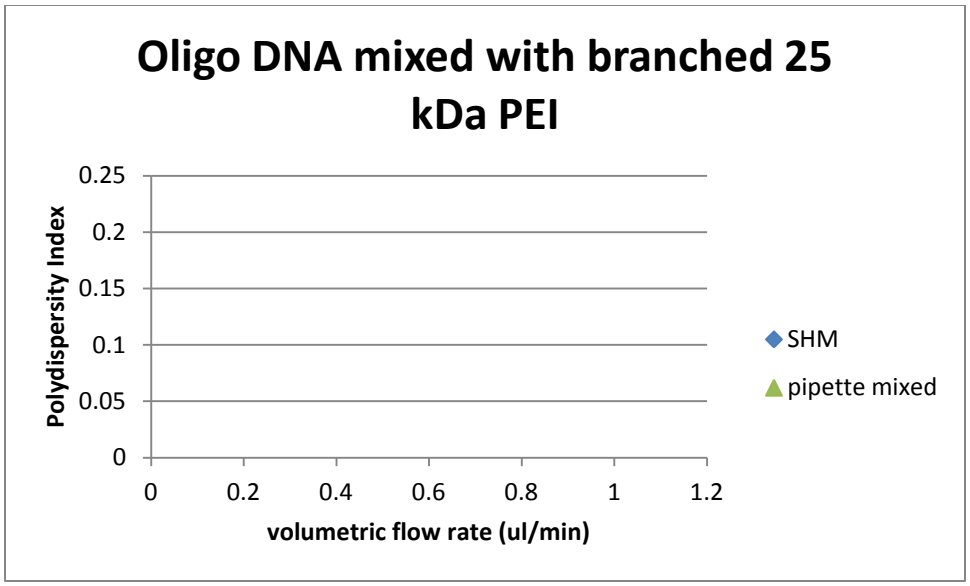

Figure 42: Polydispersity measurements from dynamic light scattering of 20 µg/ml oligo DNA mixed with 25 kDa branched PEI, N/P = 6. Error bars represent standard deviation (n = 9). Pipette mixing is not associated with any particular flow rate, but is included for comparison.

To better detect any variations in size, a larger dynamic range is necessary. Standard 25 kDa branched PEI, without the steric protection of PEG, produces substantially larger particles when complexed with 20 µg/ml oligo DNA (Figure 41). The association between mixing time and particle size is only statistically different between the highest and lowest flow rates, though a significant reduction in both size and variability is apparent. Polydispersity measurements are less clear, though there is again a significant improvement relative to pipette mixing (Figure 42). Thus, though mixing time does appear to affect polyplex size and polydispersity, it is difficult to discern with the SHM.

Discussion

Despite the challenges of modeling a chaotic advection system, the COMSOL and analytical results match confocal measurements well. This study demonstrates several guidelines for the design and operation of SHM-based devices and simple relationships to evaluate its performance for a broad range of systems.

Wet experiments with the DNA-PEI system show faster mixing than would be predicted by diffusion alone, suggesting that diffusion is not the only transport process at work. Long-range electrostatic forces appear to play a large role in transport over short lengths; this is explored in greater detail in Aim 3. Regardless, the complexation proceeds for all flow rates when advection reduces the necessary lengths to several μm—to distinguish further would require a less efficient mixer, such as a non-chaotic slanted groove device [233]. The time scale of the mixing approaches the estimated kinetic limits of complexation time at higher flow rates (170 ms vs. < 50 ms), however, the impact of this relatively fast mixing is limited when compared to slower mixing, and only shows a large difference relative to the long interaction in a smooth channel device when PEGylated PEI is used. Though this is largely due to the steric restriction of size by the PEG, even conventional non-PEGylated PEI, which can produce a broad range of particle sizes, shows limited effects of flow rate on size and polydispersity from the SHM. This suggests that, while the advective mixing of the SHM may be directly related to flow rate, it is not sufficient to significantly impact the practical mixing and complexation in the DNA/PEI system.

Despite the reduction of dispersion over the length of several mixing cycles, pressure-driven laminar flow is subject to a "no-slip" condition of zero velocity at the walls. The impacts of this are 1) longer residence times in zones near walls, 2) higher shear forces near such zones. Flow rates in the grooves, where the fluids are within 30 μm of a wall, are a fraction of those in the main channel, leading to extremely long residence times, and potentially longer interactions between species. Furthermore, at higher flow rates, when such residence times are lower, the velocity gradients and shear rates are increased. This elongates polymers, delaying compaction, and also increases mass flux, both of which

increase the likelihood of additional intermolecular interactions. Thus, mixing in the SHM is neither straightforward nor rapid with regard to large polymers.

Though a microfluidic mixer does provide a well-characterized and predictable mixing process, producing more reliable results than a technique such as pipette mixing, the actual particle size and polydispersity are not necessarily improved [204-205, 208, 269]. Furthermore, the tendency for deposition on the channel walls depletes material, potentially contaminates the product with aggregates, and ultimately degrades mixer function when processing larger volumes. Even substantial modifications to the device and formulation have, in this work, been found to be insufficient to prevent this buildup. These factors ultimately render the SHM unsuitable for practical use for the preparation of DNA polyplexes. Nonetheless, the use of a microfluidic system for remains a logical strategy to reduce variability in polyplex size. Given the biological importance of this parameter, and the noted inadequacy of current methods and standards [270-274], it is likely that even small improvements in size, polydispersity, and reproducibility will be important to safety and key to accelerating regulatory approval.

Aim 2: Low shear in Sheath Flow

Introduction

The results of the SHM experiments show the impact of surface interactions and shear on polyplex formation. Though a well-characterized mixing system is necessary for optimal control of the size and polydispersity of DNA nanoparticles, zones of high shear and contact with the surface must be minimized to prevent aggregation and produce uniform results. Though this rules out conventional advection micromixers, length scales can still be reduced to the length scales necessary for diffusion by sandwiching a reagent stream between faster flowing fluid [242-243, 275], either a carrier stream, or another reagent. 3D focusing techniques both eliminate contact with the channel walls and reduce variations in velocity and residence time, reducing variability in the physical conditions under which the complexation occurs. Creating a rapid mixer using sheath flow requires a very thin core, and a very large ratio of sheath-to-core flow rates [242], which is impractical for the production of a meaningful quantity of polyplexes. A larger core means substantially longer mixing times, as the length scale is fixed at tens of μm; diffusion time over that distance is greater than 1 s for even a relatively small species. However, the results of the SHM from Aim 1 show that surface interactions and shear forces may be more significant to polyplex assembly than pure mixing time (Figure 43).

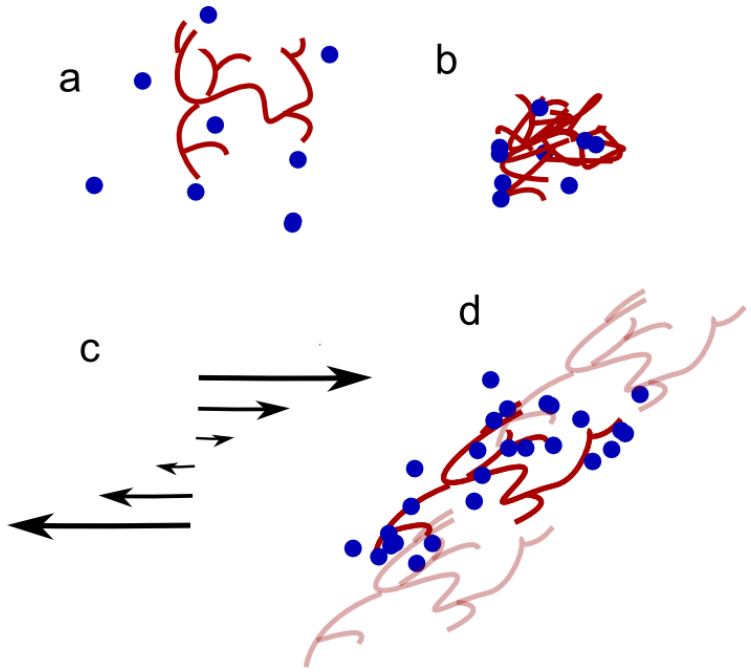

Figure 43: The effects of shear and mass transport on aggregation. Charged polymers and polyions (a) are electrostatically attracted to form larger complexes. In the absence of flow, the species interact only with those other species within diffusion distance, and they collapse into small, isolated complexes (b). In pressure-driven flow, velocity changes with position over the width and height of the channel, which, from a frame of reference within the solution, is significant relative flow along the channel axis (c). The shear force tends to elongate polymers, extending the time and surface area for interactions, and also produces greater local mass transport, due to the relative motion of the adjacent fluid streams increasing apparent material flux and the number of species with which the polymers may interact. These conditions are highly conducive to larger buildups of multiple crosslinked polymers (d).

Device design

A sheath flow device (SFD), designed to prevent the aggregation of DNA and PEI seen in the SHM, has different requirements than typical applications of the technique. The interface between the two reagent solutions must be separated from the walls, even at the inlet, to prevent any steady-state zones of neutral charge where precipitation might occur. Furthermore, unlike devices for kinetics studies, sample recovery is required. One such device, designed by Ligler and colleagues, is suited to this purpose [243, 276-277]. Briefly, a stream of sample is flowed between two streams of buffer, and symmetric grooves set into the top and bottom of the channel, vertex oriented in the direction of flow (y-direction), direct the buffer around the sample, creating a sheath-and-core structure. The dimensions

are reasonable for the production of laboratory quantities of polyplexes, and the principles of operation are similar to the SHM.

A few modifications are required to adapt this sheath flow device (SFD) to the DNA-PEI system. The sample core consists of the DNA and PEI solutions stacked vertically, keeping the interface away from the walls except transiently at the inlet, and giving a large horizontal interface for complexation and the smallest transport distances possible. A long interaction channel is followed by an "unsheathing zone", in which the herringbones are pointed opposite the direction of flow (y-direction). Due to the deterministic nature of low-Re flow, this topologically reverses the sheathing process [276], and the polyplex suspension is layered vertically between the buffer flows to be recovered from a trifurcated outlet channel. The minimum length scale in this device is considerably larger than those attained by the SHM, so the complexation is completely transport-limited, with Da on the order of $10\text{-}10^3$. However, because the complexation zone is a simple interface with relatively uniform velocity, the complexation conditions and extent are expected to be uniform.

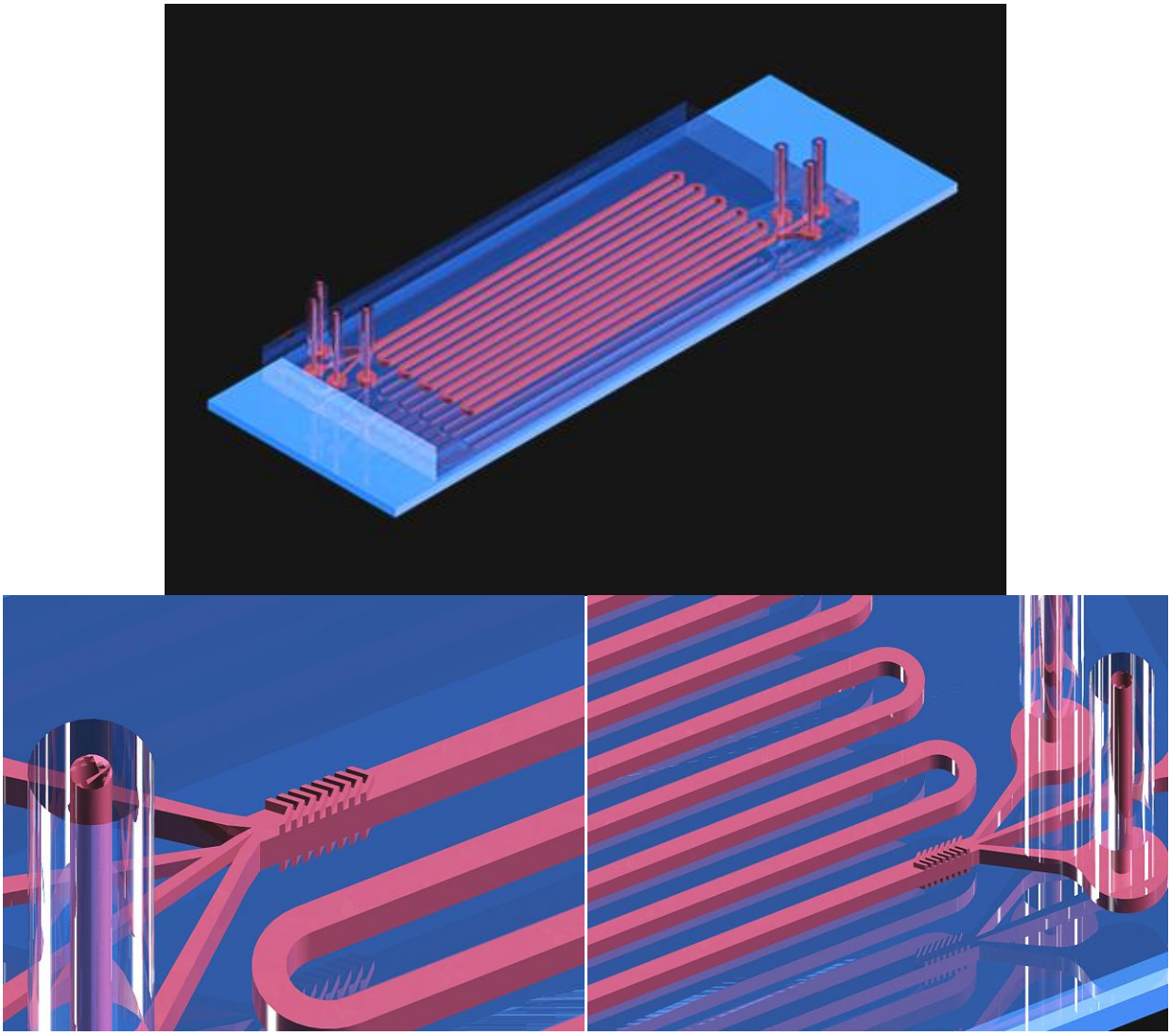

Figure 44: Schematic of the SFD. The 2-layer PDMS device produces sheath flow by symmetric sets of grooves in the top and bottom of the channel (lower left). Grooves at the end unsheath the core for separation at the outlet (lower right).

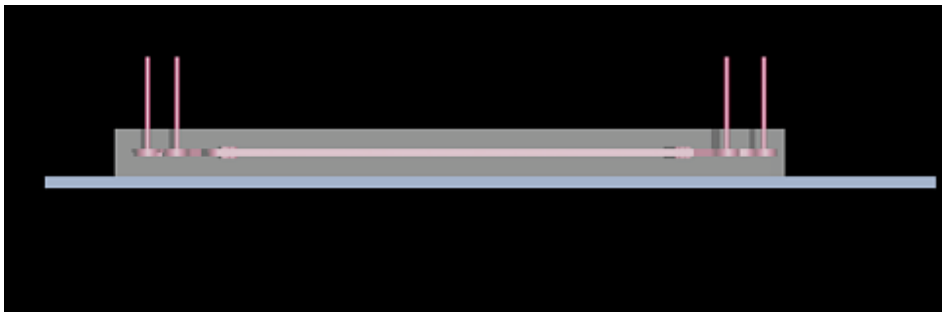

Figure 45: Side-on view of the SFD. Unlike the SHM and smooth-channel devices, the SFD consists of two PDMS layers, with the channel described between them. The glass slide is for rigidity.

To produce the vertical stacking of the DNA and PEI streams, the inlet takes advantage of the two PDMS layers; one sample inlet is in each layer, intersecting at the inlet, while the inlets for the sheath fluids spans both layers, and join the channel from either side (Figure 44). A model, prepared in COMSOL 3.5a, verifies that the two core fluids stack, producing a horizontal interface (Figure 46). Because the initial contact point between the fluids is necessarily adjacent to a wall, the potential for aggregation must be considered. The model was modified to simulate such a complexation, showing both the location and likely extent of interaction to better evaluate the risk of aggregation and fouling. Despite improvements in both the software and processing capacity, the high Pe of the system remains difficult to model in 3D, so the Navier-Stokes equations were solved for the entire inlet, and the convection-diffusion and complexation were solved in a smaller subdomain, where the DNA and PEI fluid streams meet. The model assumes an input of 44 μL/min for each of the sample inlets, which are 65 μm (w) x 65 μm (h), which corresponds to a mean velocity of 3 mm/s; buffer inlets to either side 135 μm (w) x 130 μm (h), with a buffer: core flow ratio of 4:1 (Figure 46). A transport-limited complexation between 75 μg/ml plasmid DNA and 25 kDa branched PEI at an N/P ratio of 6 was then modeled in a reduced geometry to assess potential aggregation, using the flow solution from the full inlet (Figure 47). The sheathing section of the device is assumed to have a cross-section of 400 μm (w) x 130 μm (h), and grooves set 65 μm deep into the top and bottom of the channel, and 75 μm wide along the channel length (Figure 44). The flow model indicates that, for the low Re operation of the SFD, the interface between the two sample flow streams is horizontal. Though some interaction between the species at the inlet is inevitable, the model suggests that it is low in magnitude (Figure 47).

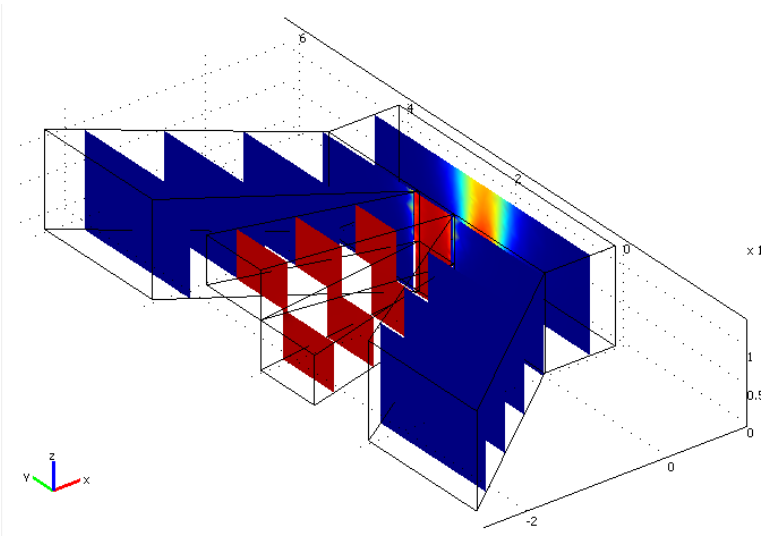

Figure 46: Geometry of SFD inlet, from COMSOL model, showing reagent (red) and buffer (blue) streams.

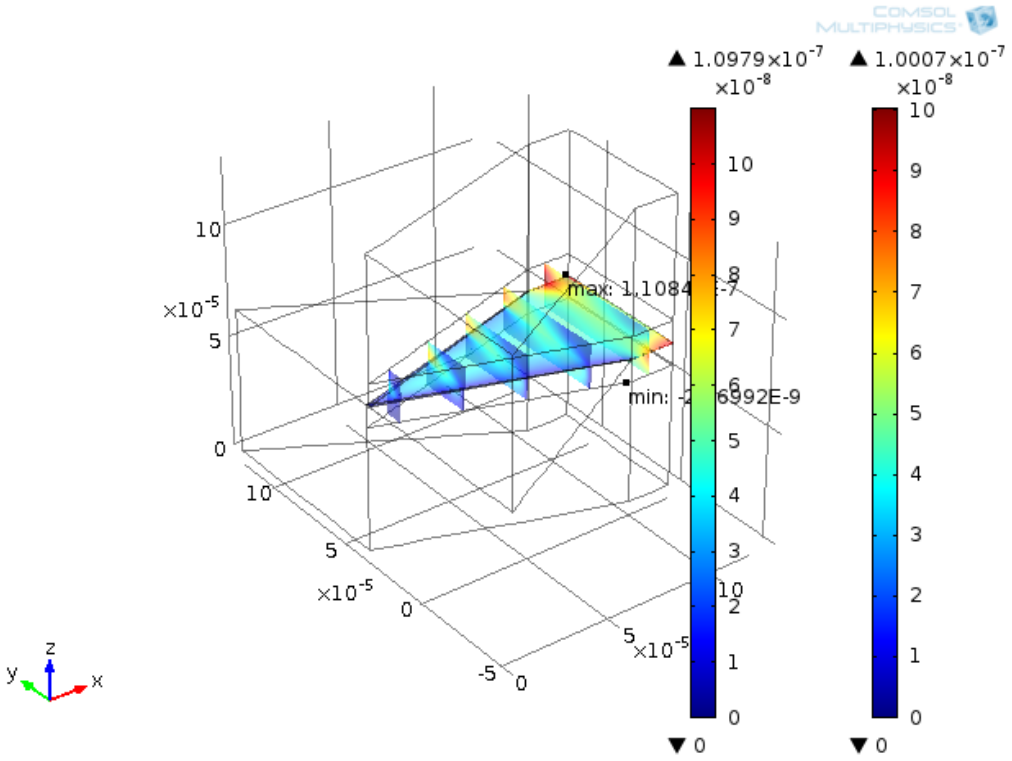

Figure 47: COMSOL model of the sample inlets of the SFD, showing the interaction between DNA and PEI. The predicted magnitude of complexation, and, therefore, the potential for aggregation, is low.

One disadvantage of this device as compared to the SHM is that it is entirely design-dependent, and the thickness of the fluid core is entirely dependent upon the number of grooves used to create the sheath structure [277]. This means that the device function is tunable only by the relative flow rates of core and sheath fluids, and only over a limited range. Mixing performance is a fixed function of the device design and the inherent mass transport of the species.

To determine the ideal number of grooves, additional modeling was required, though again the high Pe of the system precluded an explicit 3D model. Instead, the Navier-Stokes equations were solved for 3D channels with the velocity profile from the inlet model as an upstream boundary condition, and 4-10 sets of grooves. The simulated velocity was then exported from these 3D models and set as a condition for a 2D convection-diffusion model of the channel cross-section, creating a pseudo-3D model with time substituting for the axial dimension. This is easier to solve, as there are fewer simultaneous degrees of freedom than in the steady-state 3D model, and such an approximation has been used to analyze groove-driven advection previously [252].

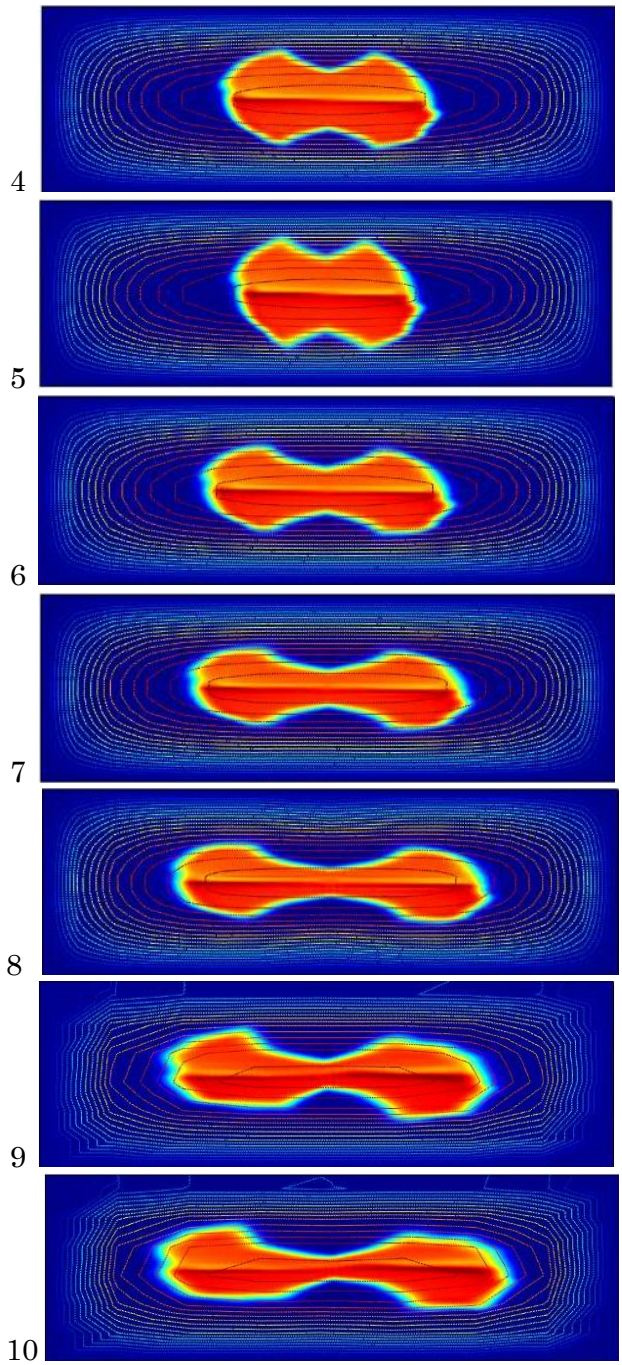

Figure 48: Surface plots of DNA and PEI concentration (both normalized to 1) flowing inlet and sheathing section of sheath flow device, 4 (top) to 10 (bottom) pairs of grooves, overlaid with isolines of linear velocity in the channel. Total flow rate is 7.33 μL/s (Re=18), with 20% sample flow. Interfaces are much clearer following modifications to the inlet model, and the DNA-PEI interface is near-horizontal. The model was extended to 9 and 10 grooves, and the resolution had to be reduced to accommodate the additional length, so the models are slightly choppier in appearance. 8 groove pairs (3rd from bottom) appears to be the best configuration in terms of a thin, but relatively uniform layer.

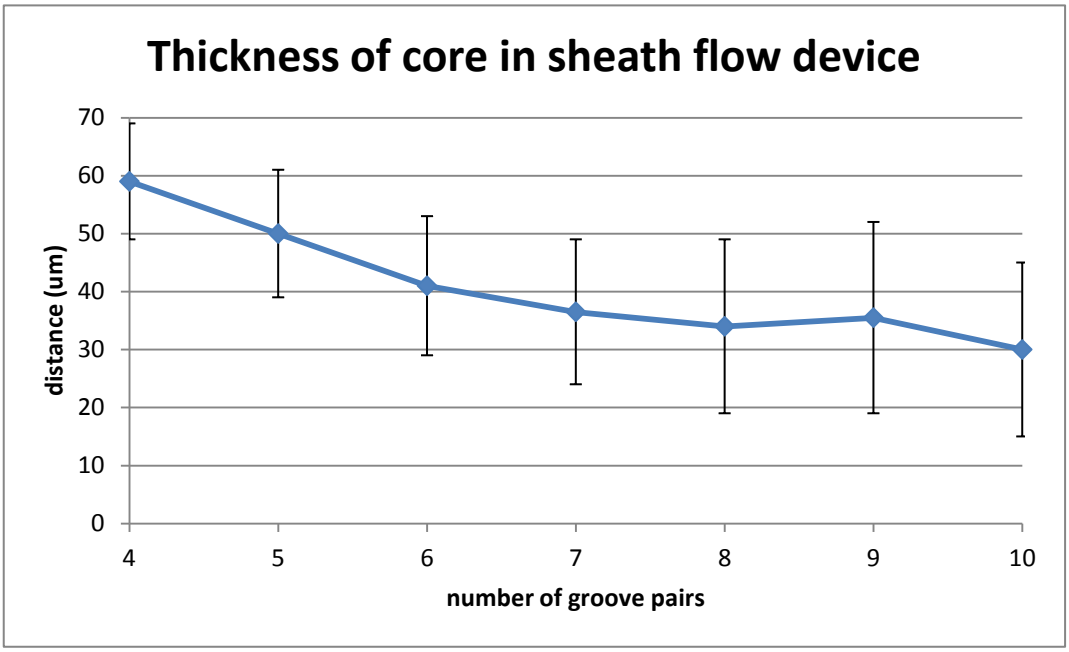

Figure 49: Plot of average thickness and min-max spread of sample cores from sheath flow device, 4 - 10 groove pairs , as measured by hand from the COMSOL model. A setup with 8 groove pairs balances core thickness/interface area and uniformity.

Core thicknesses were measured by hand from the surface plots of the models (Figure 48, Figure 49), by taking the minimum thickness near the centerline, the maximum thickness farther out, and the widths. Both minimum and maximum thicknesses decreased out to 8 groove pairs, though models of 9 and 10 pairs were somewhat choppier, due to the reduced resolution required for export and re-import of the data. Though interface width increased monotonically, 8 grooves seemed the optimum number to produce a thin, yet relatively uniform core.

Because this 2D model did not explicitly consider flow down the channel perpendicular to the model, molar flux varied by around 30%-40% due to the positioning of the core in the high-velocity region of the channel.

A sheathing unit of 8 grooves was selected to balance the mean and distribution of core thickness, though performance appears similar over that range, suggesting that the device can work with minor variation of thickness during fabrication. The minimum length scale, a maximum diffusion length of around 20 μm, is considerably larger than those attained by the SHM, so the complexation is completely transport-limited, with Da on the order of 10^{-3}. However, because the interaction zone is a simple interface with relatively uniform velocity, the assembly conditions and extent are expected to be uniform. Nonetheless, even a small solute requires seconds to diffuse such distances, so a long channel is required for the complexation.

Fabrication and operation

Because sheathing requires grooves in both the top and bottom of the channel, the SFD consists of two aligned PDMS layers. These layers are exposed to oxygen plasma as for bonding, and immediately submerged in DI water to preserve the activated surface. They are then manipulated under a microscope, with ethanol to temporarily prevent bonding and facilitate alignment of the layers. The device is then heated to 65°C for 4 hours, allowing the ethanol to evaporate, and the activated PDMS surfaces to contact and bond. Alignment of the devices was typically within 5 μm, adequate for function (Figure 50).

Figure 50: Image of an assembled SFD. Alignment of the PDMS layers is within a few μm of design, despite the material flexibility.

To assess the functionality of the SFD, the device was run with 10 mM HEPES, pH 7.5, with 10 μM fluorescein in one of the two sample inlets. To control the four inlets and two of the three outlets, six Kloehn syringe pumps were used with 100 μL syringes and controlled via command line, and the minimum recommended flow rate of 120 steps/s (15 μL/min) for the two sample lines, with a buffer-to-core ratio of 4:1. The fluorescein was effectively sheathed, developing a concentration profile with two distinct peaks, as predicted by the COMSOL model (Figure 51). However, the core is narrower, with shallower peaks, more similar to the model for 6 groove pairs (Figure 48). This apparent 25% reduction in advection is likely due to deviations from the assumed dimensions, or the difference between the simplified pseudo 3D model and the realities of Poiseuille velocity profiles, grooves, inertial flow (Re = 18), and the mechanically-compliant PDMS channel.

The fluorescein test also revealed problems with the pump setup. The elasticity of PDMS gives devices fabricated from it considerable pressure capacitance, most frequently

observed as flow continuing after the pumps are shut off. The two-layer SFD has sufficient compliance that the pressure differences between the buffer and sample lines produce a startup time of approximately 30 s before flow stabilizes, and a flood from the sample lines following shutoff. This renders data acquisition difficult, given a total run time of only 90 s before a syringe refill is required, severely limits the amount of product that can be collected from the outlet, and makes aggregation on the channel surfaces unavoidable.

To avoid this problem, the buffer and sample lines must be run at equal flow rates, to generate equal back pressures. Additionally, this increases the potential analysis time, as well as the possible collection volume, by allowing the full 200 μL of the two sample syringes to be dispensed. However, it also increases the dimensions of the core to around 70 μm, increasing the mean transport length to about 18 μm. The time required for oligo DNA to diffuse that distance is 16 s. The lower total flow rate increases residence time in the channel 2.5 fold, to approximately 7.5 s, insufficient by diffusion alone, but the contributions of the electrostatics of the system to mass transport cut transport time by 40% in the SHM, and a similar increase in transport here brings the transport and residence times to similar values.

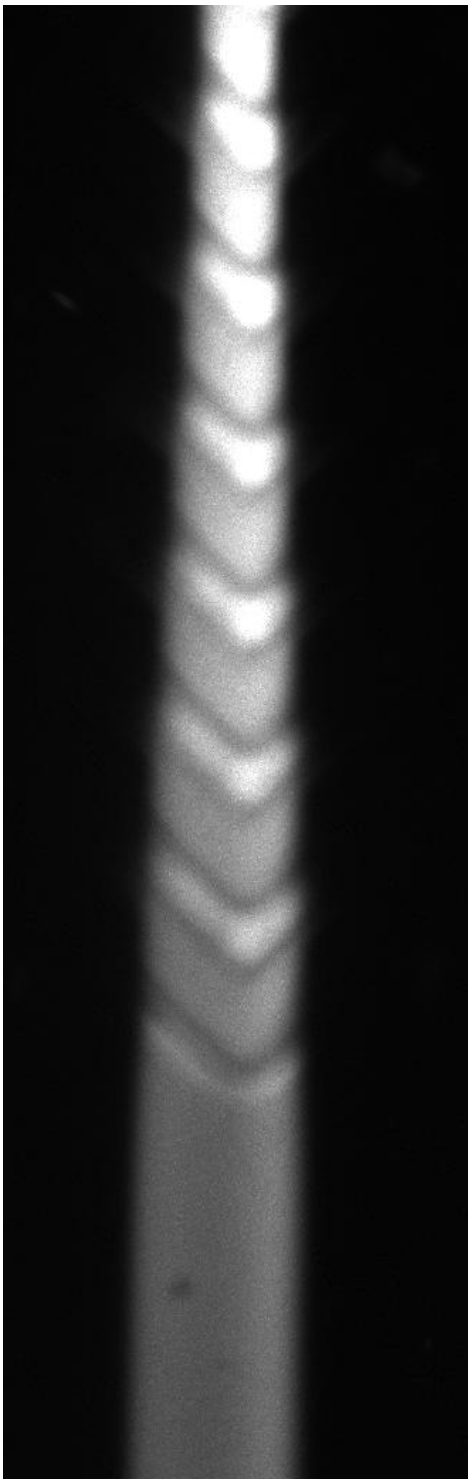

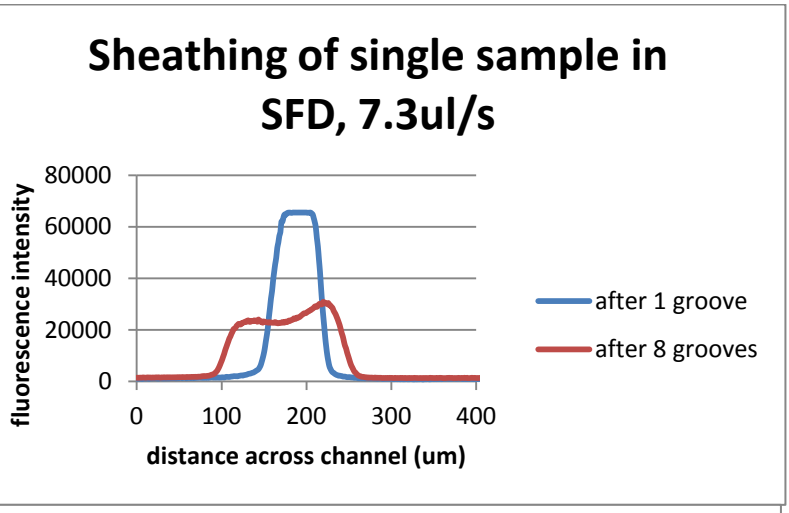

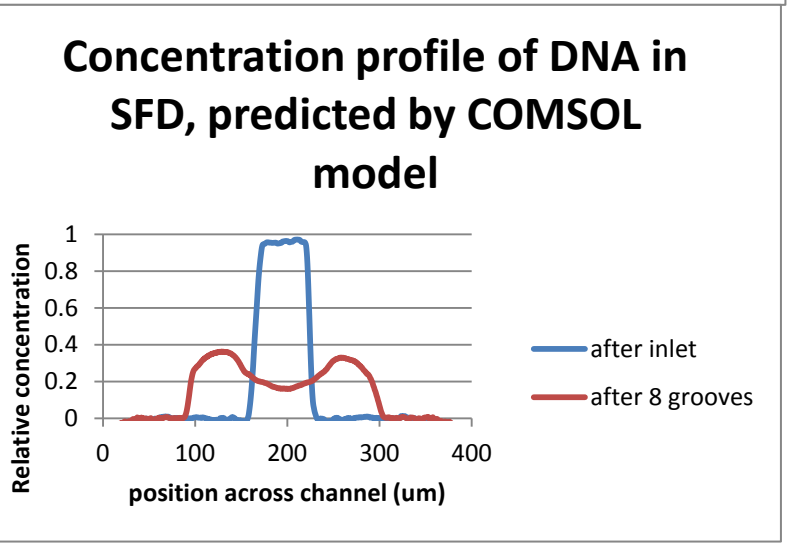

Figure 51: Fluorescence image of sheathing grooves of SFD with one inlet of fluorescein (*left*), the intensity profiles from the setup (*upper*), and the predicted concentration profiles from the COMSOL model (*lower*).

DNA complexation in the SFD

To assess the function of the SFD with equal flow inputs, plasmid DNA labeled with ethidium bromide was loaded into the two sample inlets, and the syringe pumps were run at 15 μL/min each (60 μL/min total). Though the core occupies a significantly larger fraction of the channel, it does not extend to the sides, and the characteristic peaks of intensity indicate the presence of a sheath (Figure 52). Measurement of the concentration profiles indicates that the core is maintained for significant distance downstream, with the sides never extending the full extent of the channel (Figure 53). The profile does degrade considerably, however, possibly due to variations in pumping, or possibly a bubble or defect in the channel. Nevertheless, the sheath structure does separate any interaction from the walls for at least several seconds.

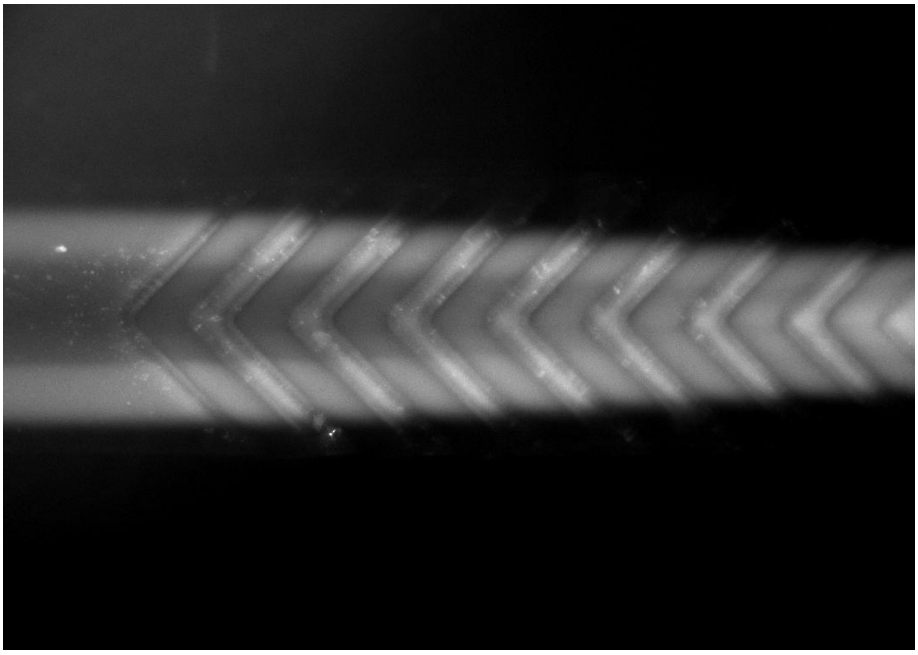

Figure 52: DNA labeled with ethidium bromide in the SFD, with all four inlet flows at 15 μL/min. The sheath is considerably smaller with equal flow rates, but the core is successfully separated from the walls.

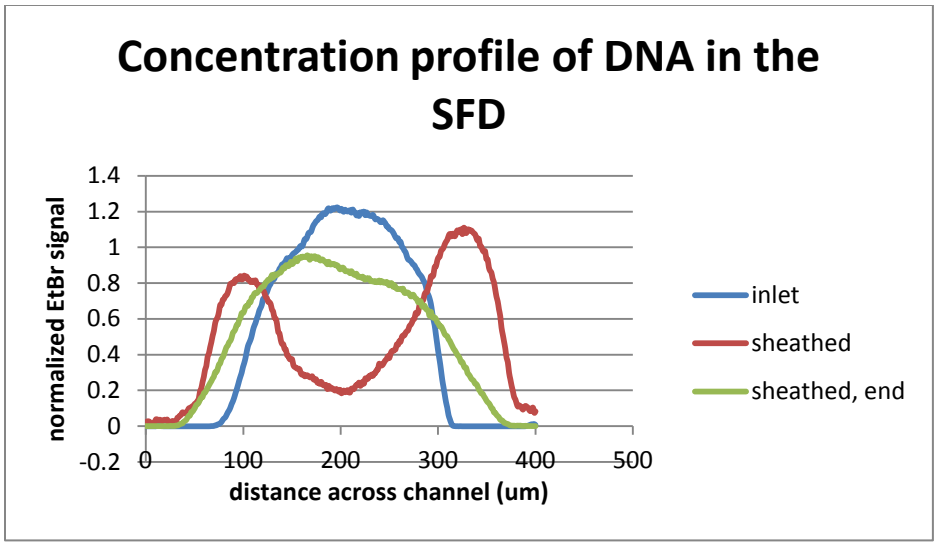

Figure 53: Concentration profiles of DNA in the SFD immediately following the inlet, and the sheathing grooves, and immediately prior to the unsheathing grooves. Though the core form relaxes considerably, it still occupies only the center region of the channel.

To observe complexation in the channel, 40 μg/ml oligo DNA, labeled with 5.3 μg/ml ethidium bromide and PEG-PEI to produce an N/P of 6, in 10 mM HEPES, pH 7.5, were loaded into 500 μL sample loops on each of the central sample inlets, and the sheath lines were filled with plain buffer. All four inlets were run at 15 μL/min. The fluorescence signal disappeared along the channel length, disappearing well before the outlet, though the thickness of the device created considerable optical interference and a variable, location-dependent background fluorescence, preventing quantitative analysis. The output of the device was collected over 3 separate runs, and measured by DLS. No significant effects on either size (Figure 54) or polydispersity (not shown).

The relative insensitivity of the oligo/PEG-PEI nanoparticles is likely due to steric restriction of the size by PEG. Furthermore, that relatively small size produces a weak scattering signal, so any minor variations are undetectable. Unmodified PEI, on the other hand, produces larger, highly variable polyplexes, so any differences are easier to detect, though it is considerably more prone to aggregation in a microchannel.

To simplify pump operation, the DNA was sheathed by 25 kDa PEI, which is in excess at N/P = 6, which increases the total interfacial area for interaction between the fluids, but moves the complexation zone closer to the walls. Nonetheless, the fluorescence decreased to background levels by the end of the channel, and no accumulation of material was observed in the channel during the run. Again, the output of 3 separate runs were collected, and measured via DLS.

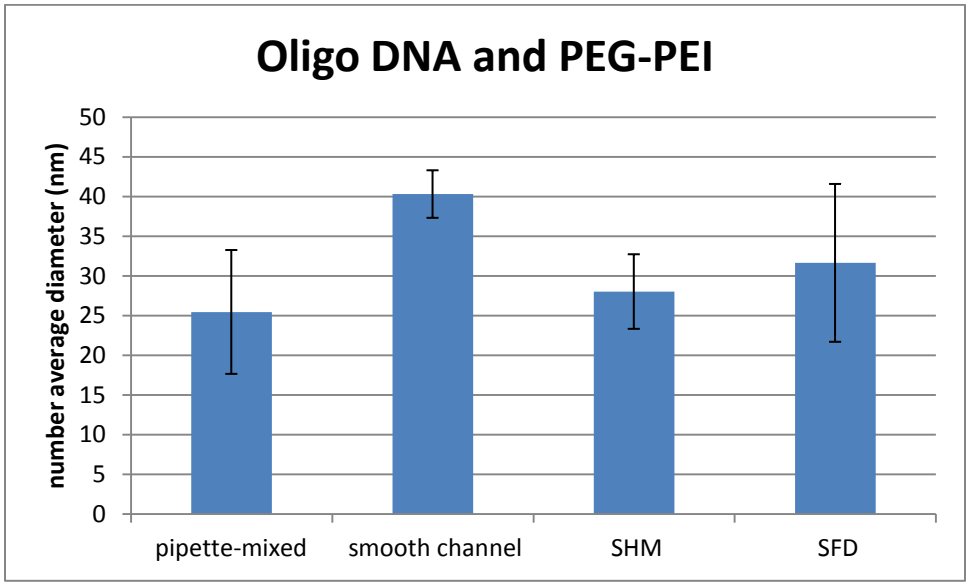

Figure 54: A comparison of polyplex size, measured by DLS, for different fabrication methods of 40 µg/ml oligo DNA with PEG-PEI at an N/P ratio of 6. Error bars represent standard deviation (n > 9). The SHM and smooth channel devices were run at a total flow rate of 60 µL/min. In this case, the SFD was run with a core of DNA and PEG-PEI in HEPES buffer, pH 7.5 at 15 µL/min each, and a sheath of HEPES, pH 7.5 at a total of 30 µL/min (60 µL/min for all fluids).

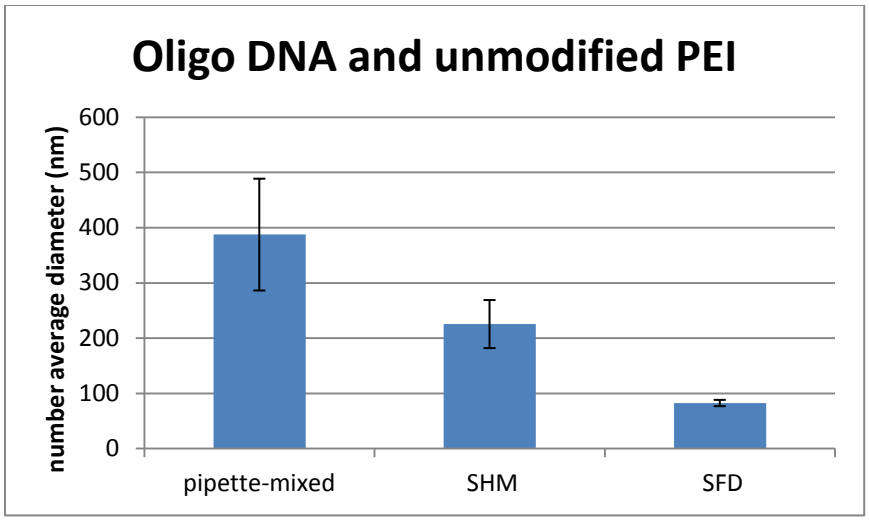

Figure 55: A comparison of polyplex size, measured by DLS, for different fabrication methods of 20 µg/ml oligo DNA with PEG-PEI at an N/P ratio of 6, in HEPES, pH 7.5. Error bars represent standard deviation (n > 9). The SHM was run at a total flow rate of 60 µL/min. In this case, the SFD was run with a core of DNA HEPES buffer, pH 7.5 at 30 µL/min, and a sheath of unmodified PEI in HEPES, pH 7.5 at a total of 30 µL/min (60 µL/min for all fluids).

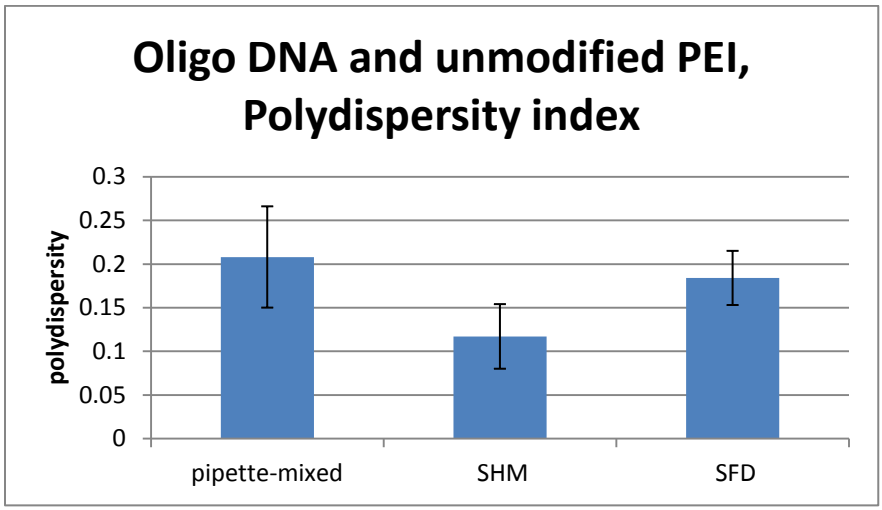

Figure 56: A comparison of polydispersity for different fabrication methods of 20 µg/ml oligo DNA and PEG-PEI at an N/P of 6, in 10 mM HEPES buffer, pH 7.5.

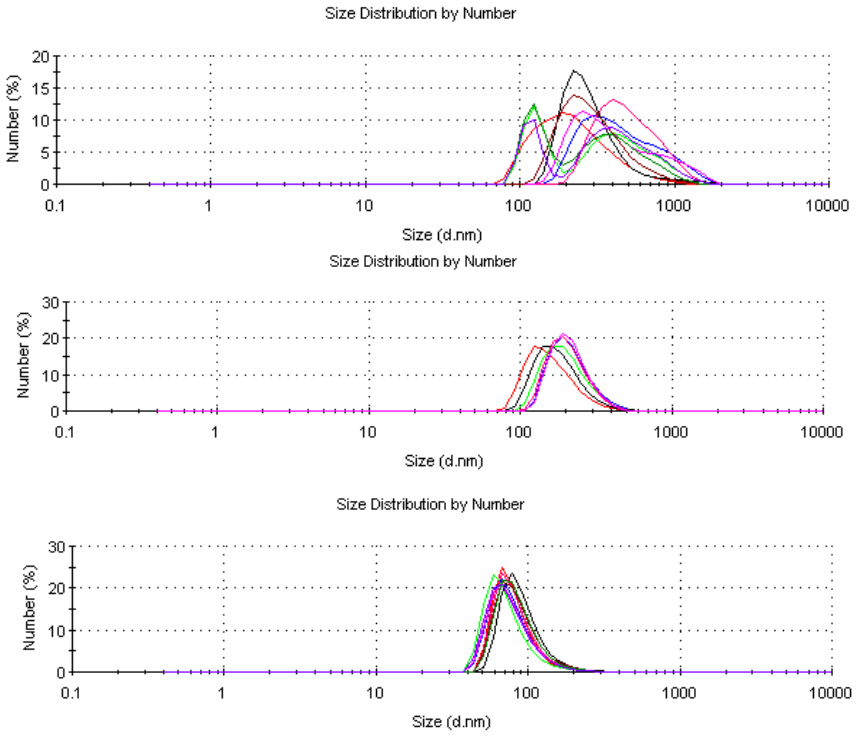

Figure 57: Size frequency curves of nanoparticles from 20 μg/ml oligo DNA mixed with PEI (N/P = 6), prepared by pipette mixing (upper), SHM at 60 μL/min (middle), and in the SFD with a DNA core and PEI sheath (lower), as measured by DLS.

As expected, the particles were significantly larger than those produced from PEG-PEI, but they were substantially smaller than those produced with unmodified 25 kDa PEI by either pipette mixing or the SHM, with a very low standard deviation (Figure 55). This difference in measured size was not due to precipitation of larger species during the time between sample collection and analysis, nor was it due to the presence of ethidium bromide; the pipette-mixed controls of these factors (not shown) were significantly larger. There was no measured change in polydispersity (Figure 56), though the reproducibility of the SFD-prepared particles is clearly superior (Figure 57).

Discussion

The significant reduction of particle size for oligo DNA complexed with unmodified PEI suggests the complexation process is highly sensitive to shear. In this case, the species responsible for intermolecular interaction and the bulk of aggregation is the likely the PEI, being both more flexible and longer upon extension; plasmid-based polyplexes would be even more sensitive, due to the increased likelihood of intermolecular associations.

The SFD is not a versatile device, having a fixed length scale, and therefore a fixed time scale for mixing and complexation. Furthermore, though the design principle is quite simple, actual fabrication and operation of the device is complex, rendering it inappropriate for the practical production of polyplexes. However, the concept of confining the interaction zone to the center of the channel is likely the best microfluidic solution for observing and manipulating systems that tend to aggregate or interact with surfaces. While this has been attempted using simple hydrodynamic focusing [208], such a strategy requires a relatively low flow of DNA to achieve small length scales, and the results of Aim 1 suggest that aggregation still occurs at the top and bottom of the channel unless the flow is focused in two dimensions, as in the SFD. This investigation highlights the role of shear in polymer condensation, and indicates the possible utility value of an improved mechanism to limit wall contact and shear. Droplet-based mixing, which has shown promise for other nucleation-growth mechanisms, may be the best current option to achieve this [231].

Aim 3: Manipulation of Transport via the Liquid Junction Potential

Introduction

A liquid junction potential (LJP) forms spontaneously at the aqueous boundary of any two electrolyte solutions, where a difference in diffusivity between ions of opposing charge produces a transient separation of charge (Figure 58). The magnitude of this separation of charge is entirely dependent upon the relative concentrations and mobilities of the ions on either side of the boundary; a larger difference in diffusivity between an ion pair generates a larger potential. Because the effect is quite small and short-lived, typically peaking in the mV range and decaying in less than 1 s, it has no impact on macroscale systems. Liquid junction potentials have historically been of concern primarily in the study of membrane potentials [278], but in the small scales of microfluidics, it has significant effects on transport within such systems [279]. Because DNA and PEI are vastly larger than their counterions, Na^+ and Cl^-, and they have a large mutual attraction, the LJP profoundly affects the mixing and interaction between them, nearly doubling the apparent mass transport rates in both the SHM and SFD (Aims 1 and 2).

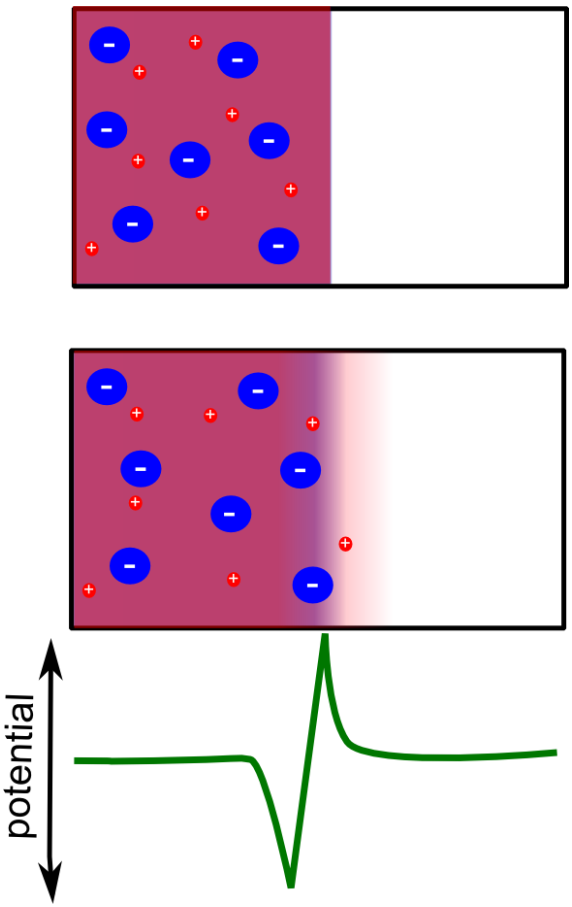

Figure 58: Illustration of the liquid junction potential (LJP). Differences in diffusive mobility between cations and anions produce a transient separation of charge at the interface. The resulting electric field then influences further transport of charged species.

Though the greatest potential difference is generated by large polyelectrolytes, they only account for a fraction of the charge in the system. For 20 μg/ml DNA in 10 mM HEPES, the DNA and its counterions only make up 1.5% of the total charge. Though the inherent LJP of DNA and PEI are sufficient mass transport even at such low ratios, the large excess of smaller ions migrate with the electric field, counteracting it. However, they also diffuse and generate a potential of their own. Even small salts, such as NaCl, generate an LJP at interfaces, but, as it is of considerably smaller magnitude, large concentrations would effectively blunt the LJP of larger species. However, in the DNA/PEI system, the majority of the charge is buffers.

Because the LJP is dependent upon all ions in solution, formulation of the solutions is extremely important. The standard buffer used for polyplex formation is 10 mM HEPES, pH 7.5, and this anion accounts for a significant amount of charge in the system. This need for buffering can be used to manipulate the LJP by using different buffers in the two solutions. While the HEPES anion is larger than its counterion, Na^+, Tris buffer operates over the same pH range, but with the opposite asymmetry, the larger Tris cation with Cl^-. Buffering the DNA with HEPES produces a solution with larger anions, and the relative flux of positive charge across an interface is greater than that of negative charge; this difference in potential would be reinforced with Tris on the other side of the interface, and the net electric field would move the DNA into that fluid. Placing the DNA in Tris has the opposite effect, retarding transport. Buffer choice and pH are significant physical factors in a microfluidic system of electrolytes.

For a transport-limited system, manipulating the LJP is an effective way to manipulate the complexation progress. Simply, it could be used to speed up the polyplex assembly by accelerating transport. There is also the possibility of temporal or spatial regulation of the interaction within a microfluidic device, reducing transport until the species have reached a particular location or state within the system. For processes sensitive to kinetics, it is another means to control the products. In the case of nucleation-growth systems, allowing a controlled amount of interaction could be used to create a known fraction of nuclei, biasing the system to produce smaller or larger particles.

First, to validate the modeling method, work by Munson, et al. [279] was repeated and the models were compared. The effects of a HEPES/Tris LJP on DNA transport were then measured and used to calibrate the model for polyelectrolyte systems. Next, the practical impact of LJP-modified transport on the complexation of PEG-PEI and oligo DNA in the

SHM was examined. Finally, a pH-dependent LJP system was developed to demonstrate the validity of the model and an additional mode of controlling the LJP.

Modeling the LJP

The simplest model of the LJP is an estimate of the potential difference between the two sides of the interface. The potential of membranes is commonly calculated from the Goldman-Hodgkins-Katz equation (GHK) [280]. Though this equation is derived for monovalent ions separated by a membrane, it can be repurposed for a rough estimate of the potential difference between two electrolyte solutions. It was modified as follows:

$$E_{LJP} = \frac{RT}{F} Ln \left[\frac{\sum_{A+} z_i D_i c_i + \sum_{B-} |z_i| D_i c_i}{\sum_{A-} |z_i| D_i c_i + \sum_{B+} z_i D_i c_i} \right]$$

Equation 16: A modified version of the GHK equation to calculate the potential difference between electrolyte solutions A and B , where z_i is charge, D_i is diffusivity, and c_i is concentration. The form of the GHK equation is suited for monovalent ions, but it is used here as an estimate of magnitude for all LJP systems.

While this is sufficient to estimate the magnitude of the potential difference between two solutions, and, therefore, the probable strength of the electric field over a particular transport length, it gives no information on the spatial distribution of the field, its evolution with time, and the specific transport effects on any of the species in solution. For such an analysis, the Poisson-Boltzmann equation is necessary:

$$\vec{\nabla} \cdot \left[\epsilon(\vec{r}) \vec{\nabla} \Psi(\vec{r}) \right] = -\rho^f(\vec{r}) - \sum_i c_i^{\infty} z_i q \lambda(\vec{r}) e^{\frac{-z_i q \Psi(\vec{r})}{k_B T}}$$

Equation 17: The Poisson-Boltzmann equation, describing electrostatic interactions in solutions. $\epsilon(\vec{r})$ is the position-dependent dielectric, $\Psi(\vec{r})$ is the electrostatic potential, $\rho^f(\vec{r})$ represents the charge density of the solute, c_i^{∞} is the concentration of species i at infinite distance from the solute, z_i is the charge of the ion, q is the charge of a proton, $\lambda(\vec{r})$ is a factor for the accessibility of location r to the other ions in solution, k_B is the Boltzmann constant, and T is temperature.

The Poisson-Boltzmann equation specifically models the electrostatic interactions of ions in solution; modifications render it applicable to the electric double layer (Gouy-Chapman) and solution activity coefficients (Debye-Hückel) [281-282]. This equation and its relatives are of critical importance to understanding the interactions of electrolytes, behavior of

colloids and surfaces, and conformation of large biomolecules, but the large number of interactions renders it too complex to solve explicitly. Numerical solutions are the most practical way to solve these equations, and many different strategies have been developed [283-302]. The specific assumptions made vary, depending upon the system being modeled, and so the equation for potential may take different forms, and the accuracy may vary.

One common assumption in electrostatics models is conservation of charge, or electroneutrality. This seems counterintuitive, given that the development of an electric field depends upon a separation of charge. In practice, however, this simplification to the equation for flux does not substantially affect the results of the model [303]. Electroneutrality was applied to previous analysis of the LJP in a microchannel, which used MATLAB to iteratively calculate potential (Equation 18), then move the species over a set time step via the Nernst-Planck transport equation (Equation 20) [279]. COMSOL models do not require this simplification to compute the potential field (Equation 19), and time steps are selected by the solver such that the calculations agree with the equations within the set tolerances. Those experiments by Munson, et al. were repeated to validate the COMSOL model, and the experimental setup used for further experiments.

$$\frac{\partial V}{\partial t} = \frac{-F\sum_i z_i D_i \frac{\partial c_i}{\partial x}}{F^2 \sum_i z_i^2 \mu_i c_i}$$

Equation 18: Expression for potential with electroneutrality assumed. Adapted from Munson, et al. [279]

$$M\frac{\partial V}{\partial t} + \nabla \cdot \left[\frac{F}{\epsilon}\sum_i z_i c_i\right] = -\frac{\partial V}{\partial x}$$

Equation 19: Expression for potential used in COMSOL models of LJP. ϵ is the permittivity, and M is a mass damping factor to suppress drift of the potential, as $\frac{\partial V}{\partial t}$ is not otherwise used in the model setup.

$$\frac{\partial c}{\partial t} + \nabla \cdot (-D\nabla c - z\mu F c \nabla V) = R$$

Equation 20: The Nernst-Planck equation for mass transport, which includes both Fickian diffusion (Equation 5) and electrophoretic motion. The models did not consider convection, and so the term for velocity is left out.

A more significant assumption is the behavior of large polyelectrolytes in the model. Approximating the drag behavior of a small molecule as a sphere is relatively safe, but larger species deviate significantly from that ideal, and changes in orientation and conformation occur with motion and alter its mobility [304]. Electrophoretic mobility is measured at steady state, but transient effects upon changes in the electric environment are inevitable. Rearrangements occur not only in the physical structure, but also the dielectric environment of a large species in an applied field [138]. Furthermore, a large polyelectrolyte such as DNA is closely associated with a population of counterions. These counterions electrically shield the molecule, as well as produce additional drag when an electric field moves the species in opposite directions. DNA not only interacts with small counterions and larger charged condensing agents, but exhibits changes in mobility in different buffers [146]. In addition to the complex behaviors of macromolecules, both the GHK equation and the Poisson-Boltzmann were developed for monovalent ions, and may not reflect the behaviors and effects of more complex species [280, 305].

Nevertheless, such models are the best way to approximate LJP transport behavior. Until new models of polyelectrolyte behavior are developed, simple modifications to the parameters of DNA transport allow these COMSOL models to better represent empirical measurements. This adjusted model could then potentially be used to predict DNA transport behavior.

Table 1: Values for the LJP transport models. Most mobility values are derived from diffusivities using the Einstein-Smoluchowski relation ($D = \frac{\mu k_B T}{z}$). Charges on PEI were calculated for pH 7.5, though differing pK_a values were found.

ion	Charge, z	mass	Diffusivity, D	electrophoretic	source

		(g/mol)	($\frac{m^2}{s}$)	mobility, μ($\frac{m^2}{s \cdot V}$)	
H^+	+1	1	$2.57x10^{-9}$	$1.00x10^{-7}$	
Na^+	+1	23	$1.33x10^{-9}$	$5.19x10^{-8}$	[306]
Cl^-	-1	35.4	$2.03x10^{-9}$	$7.91x10^{-8}$	[307]
SO_4^{2-}	-2	96.1	$1.03x10^{-9}$	$8.0x10^{-8}$	[306]
Tris	+1	121.1	$6.7x10^{-10}$	$2.6x10^{-8}$	[308]
HEPES	-1	238.3	$3.75x10^{-10}$	$1.46x10^{-8}$	[309]
AMPSO	-1	227.2	$3.7x10^{-10}$	$1.4x10^{-8}$	[310]
Fluorescein	-2	332.3	2.7×10^{-10}	$1.0x10^{-8}$	[311]
PEI	+366	25k	$1x10^{-11}$	$3.2x10^{-8}$	[103]
Plasmid DNA	-11514	3.8 m	$2x10^{-12}$	$3.3x10^{-8}$	[102, 312-313]
Oligo DNA	-44	14.8k	$7.7x10^{-10}$	$3x10^{-8}$	[314]

A 1D, time-dependent model was used to approximate the LJP across a simple interface in COMSOL 3.5a. The domain consisted of a 200 μm line, with 100 nm spacing between nodes near the interface at the center, increasing to 2 μm at either side, for a total of 925 elements. No transverse convection was considered, and though the experimental system was pressure driven flow in a smooth channel, the effects of the Poiseuille flow profile and Taylor dispersion were ignored for simplicity. The solutes included were any analytes (fluorescein or DNA), buffer species, counterions, and H^+, and were considered to move only via the Nernst-Planck equation (Equation 20). Equilibrium interactions were included for all buffer species to account for possible pH effects at the interface. A simple PDE mode was

set up to calculate the potential field from all charged species, and included a damping factor to reduce the floating potential, as the system included neither a fixed ground nor a specified change in potential over time (Equation 19). The boundaries were considered to be non-interacting: symmetry for the solutes, and zero electric field (Neumann). As the potential was vastly larger in magnitude than the other species, and the solutes varied in their diffusivities and mobilities, a tolerance was set for each variable to allow the solver to handle large changes in potential while limiting instabilities in the concentration profiles. The small size of the model only had 20k degrees of freedom, but the inherent instability forced small step sizes, and the time to compute each model ranged from 30 s to 4 hours.

Transport of monovalent species: fluorescein

The system used by Munson to observe LJP-induced transport was 9 μM fluorescein in 0.13 mM AMPSO, pH 9.4, flowing in a 1.4 mm wide, 10 μm deep silicon channel beside a stream of either 1 m NaCl or Na_2SO_4, also in AMPSO, at low flow rate (125 nL/s) [279]. The experiments were re-created in a PDMS device with a channel 400 μm wide, 75 μm deep, and 25 cm long, using a tabletop syringe pump for 1 μL/s total flow.

Applying the GHK equation (Equation 16) to the system, NaCl has a 4.72 mV potential, and Na_2SO_4 produces 2.85 mV in the opposite direction. Over a separation of 10 μm, this corresponds to an electric field strength of several hundred V/m in each case. Because the potential in the COMSOL model is not explicitly defined (e.g. there is no constant potential defined in the system, and floating values are only damped artificially), analyzing the gradient of potential—the electric field strength—is the most robust measurement. Though the peak value at 100 ms, at which point the potential separation appears to be approximately 10 μm, is double that estimated by GHK, the mean value is in agreement (Figure 59). Furthermore, the concentration profiles also match well, despite the possible

effects of dispersion (Figure 60-Figure 65). Quantitative transport across the fluid interface is also similar between the experiments (Figure 66) and COMSOL models (Figure 67).

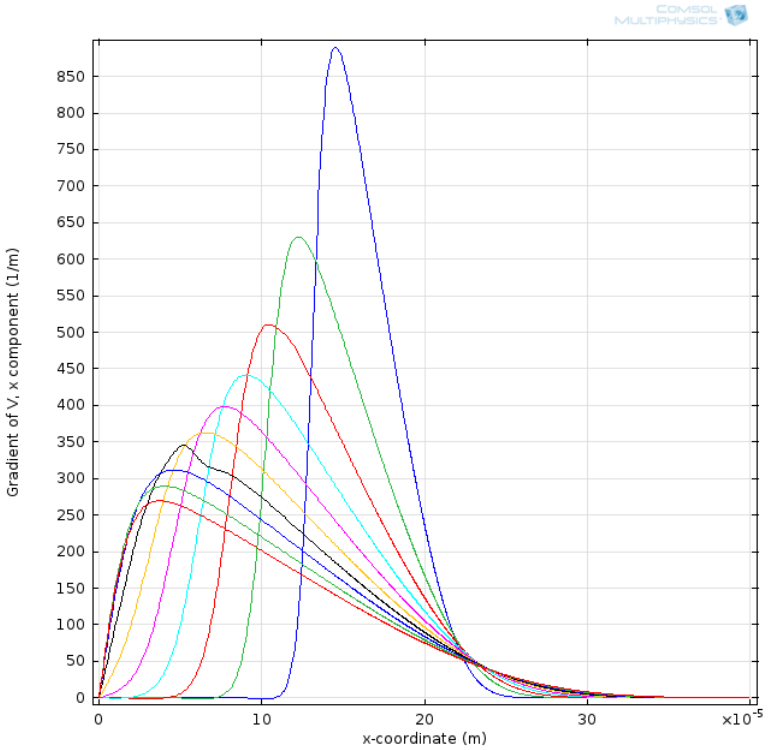

Figure 59: Electric field, at 100 ms intervals from 100 ms to 1 s, from the COMSOL model of 1 m NaCl in 0.13 mM AMPSO, pH 9.4. When species have diffused about 10 µm, the mean field strength predicted by Equation 16 is 472 V/m.

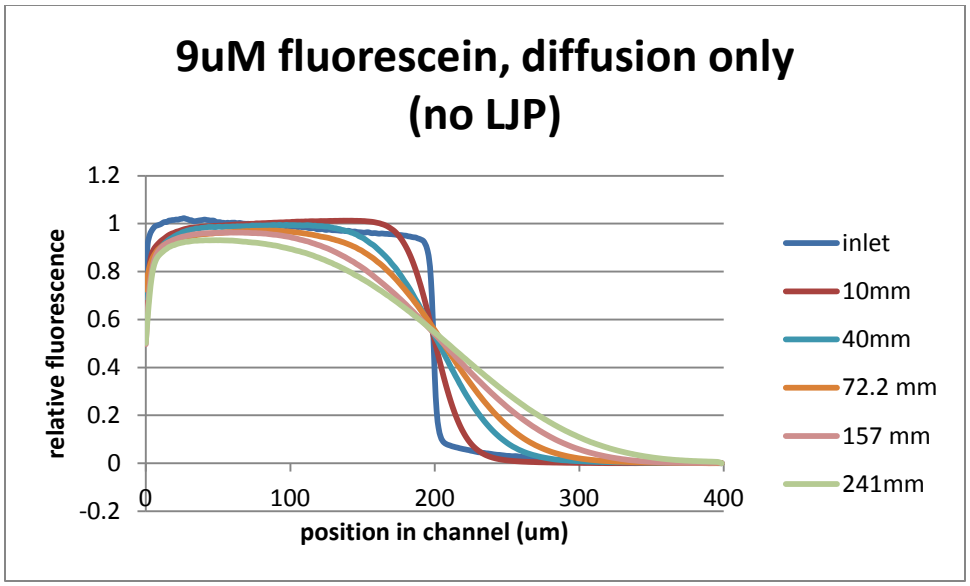

Figure 60: Diffusion of fluorescein in a 400 μm channel.

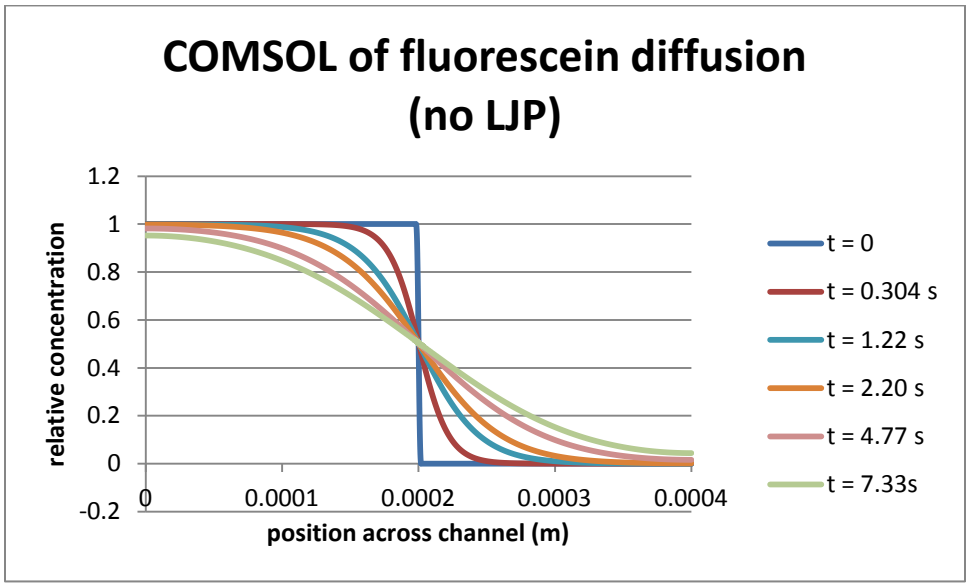

Figure 61: COMSOL model of fluorescein diffusion. Times correspond to data points from wet experiments.

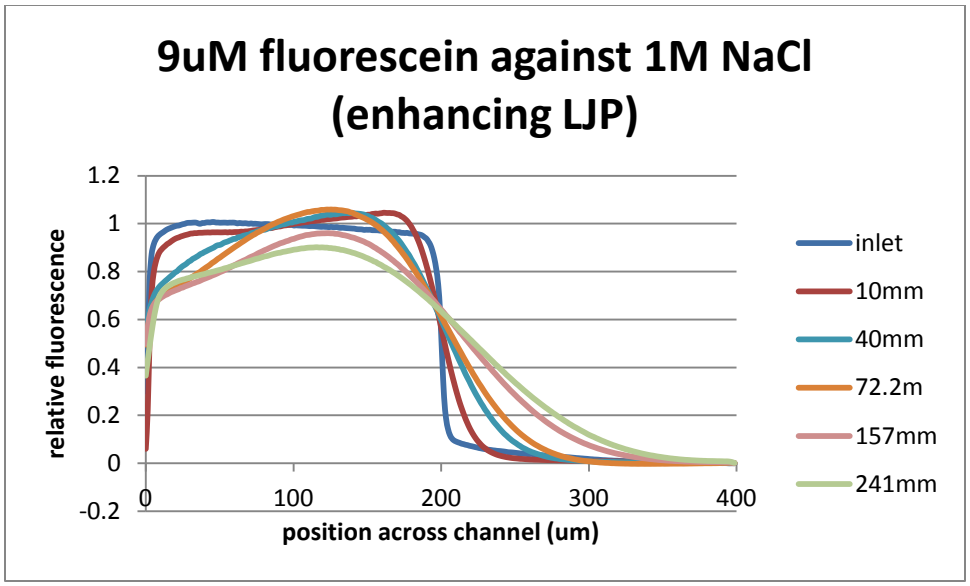

Figure 62: Experimental data of fluorescein transport in an enhancing LJP, generated by 1 M NaCl.

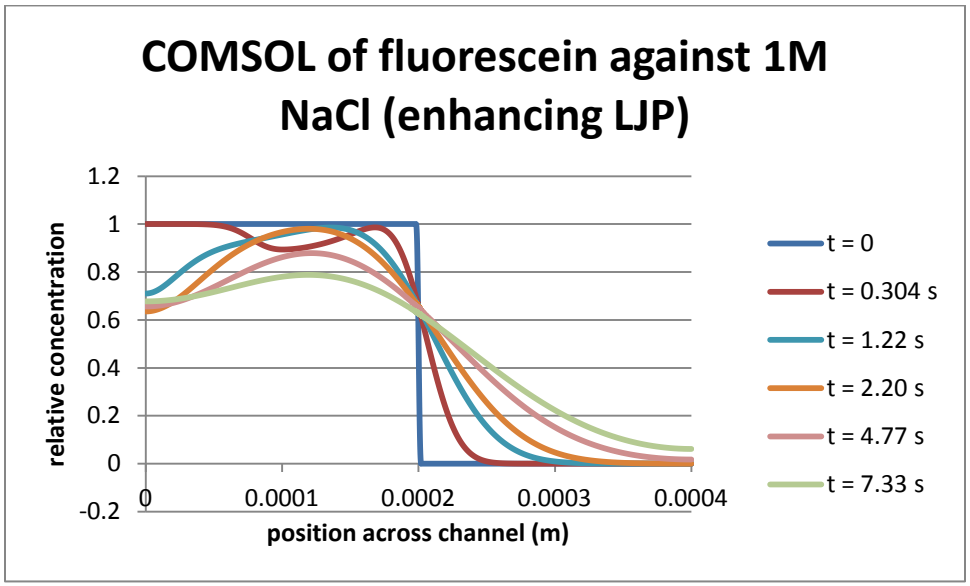

Figure 63: COMSOL model of fluorescein transport influenced by an LJP, generated by 1 M NaCl. Times match the data collection points of the experiments.

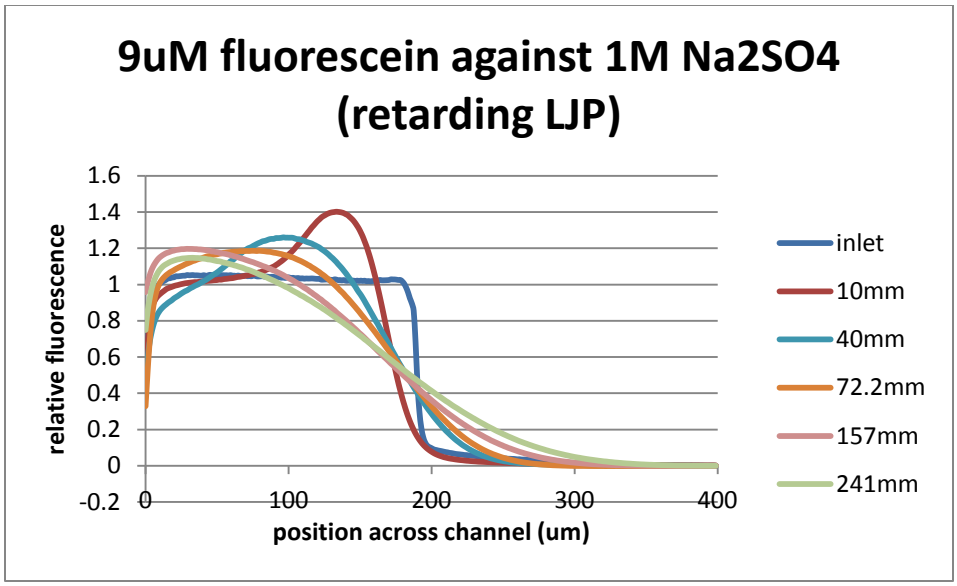

Figure 64: Experimental data of fluorescein transport in a retarding LJP generated by 1 m Na_2SO_4.

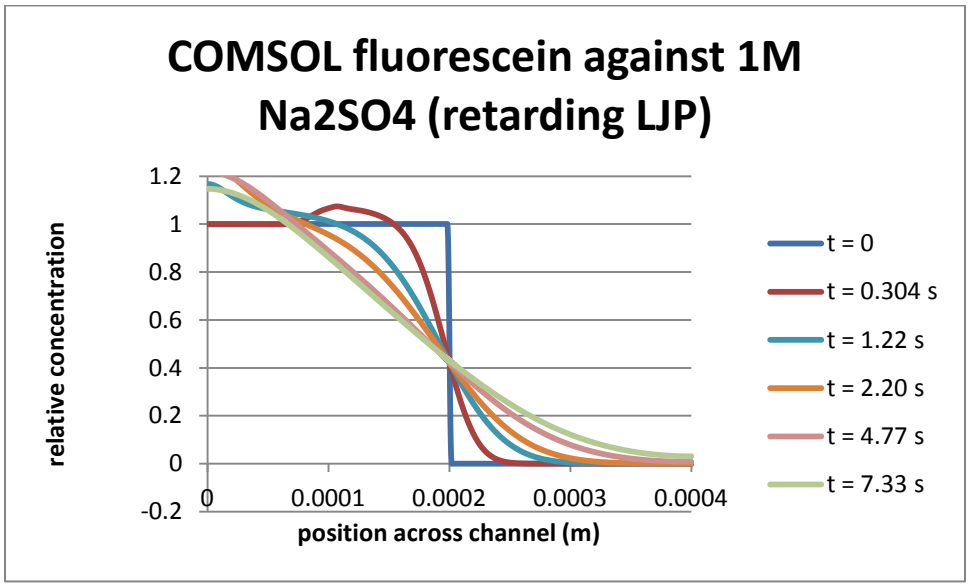

Figure 65: COMSOL model of fluorescein transport with a retarding LJP, generated by 1 m Na_2SO_4. The time points match the data collection points of the experiment.

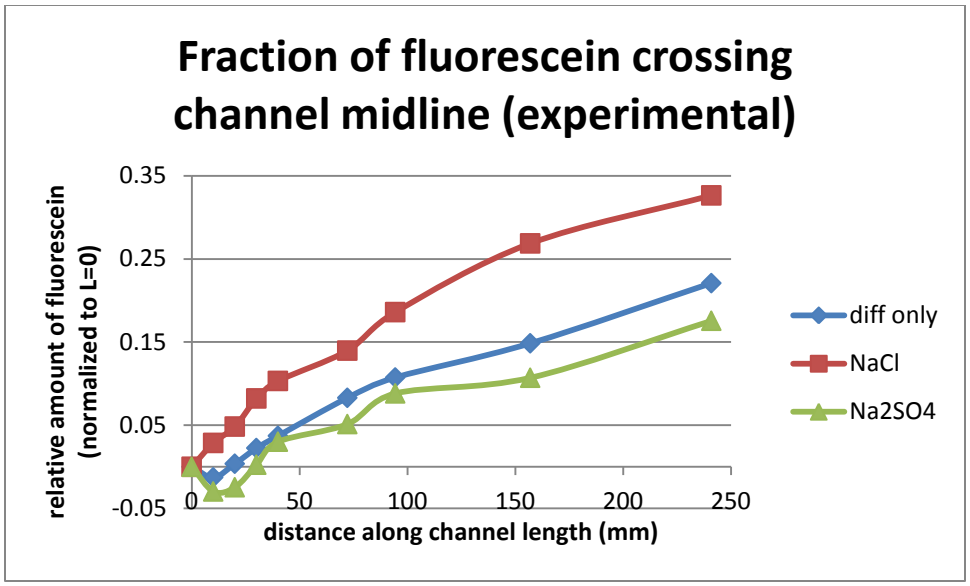

Figure 66: Fraction of fluorescein crossing the channel midline by diffusion, and under the influence of liquid junction potentials generated by 1 m NaCl or 1 m Na_2SO_4 on the other side of the channel.

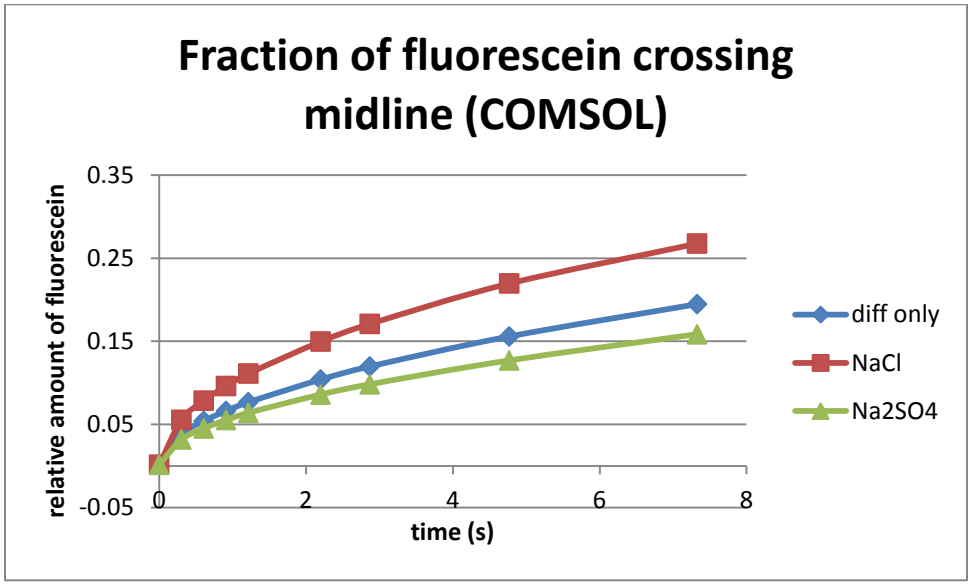

Figure 67: Fluorescein transport across midline in COMSOL models of diffusion, and of transport by liquid junction potentials. Times correspond to data collection points from wet experiments.

Given the differences between the experimental setup used by Munson, et al., and the one presented here, it was necessary to alter the COMSOL model to match that setup for proper comparison. With the lower presumed flow rate, the COMSOL model did differ somewhat from the one developed in MATLAB, matching the published results more closely. The

differences could be due to the electroneutrality assumption, not used in the COMSOL model, or, more likely, in the size and placement of the time steps of the model. Nonetheless, these results show that the COMSOL model is a good representation of the forces and behaviors caused by the LJP for systems of small ions.

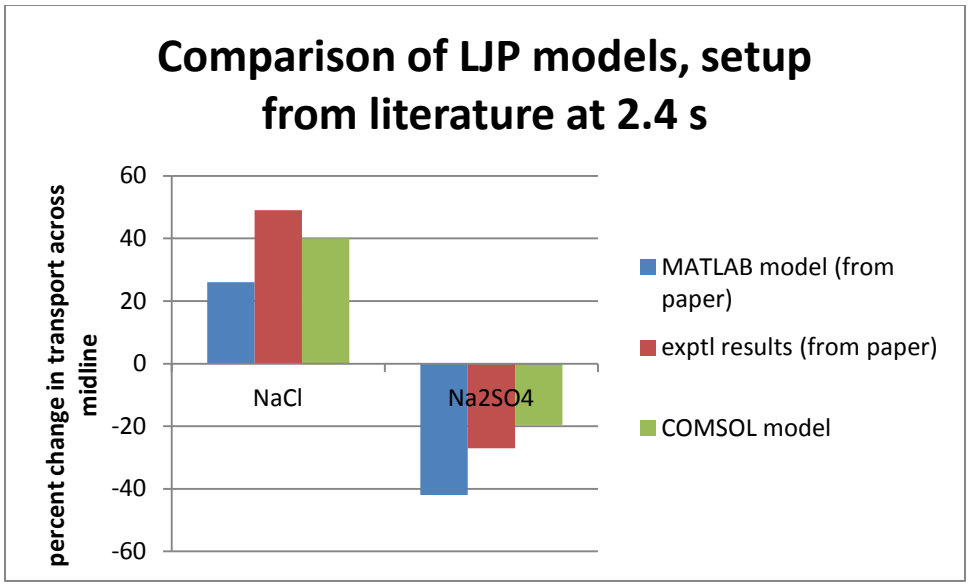

Figure 68: Comparison of LJP transport effects computed by MATLAB [279] and COMSOL models to published experiments.

Transport of polyelectrolytes: DNA

While the GHK and Poisson-Boltzmann equations are good descriptors of small electrolytes, large molecules such as DNA are considerably more complex. The equations provide a good starting point for examining the behavior of an LJP involving DNA, but using literature values for DNA mobility overstates transport considerably in the COMSOL model (not shown). Though there are a multitude of possible reasons why this system does not behave like a system of simple monovalent species, these hypotheses are beyond the scope of this investigation. The best way, then, to produce a functional model for the behavior of DNA in

an LJP is to experimentally observe such a system, and adjust the model to match. That model will then be an acceptable approximation of DNA transport in similar systems. Until the transient electrophoretic of DNA is better understood, this is the most practical approach.

The transport of both plasmid and oligo DNA was measured in a PDMS device with a channel 300 μm wide, 75 μm deep, and 250 cm long. 40 μg/ml DNA labeled with 5.3 μg/ml ethidium bromide, a concentration sufficiently low as to not significantly affect total charge, was flowed alongside blank buffer at 1 μL/s total flow rate. The buffers carrying the DNA and the blank stream were varied to create different potentials, but all were at pH 7.5.

	DNA carrier solution	Blank buffer
No LJP (diffusion only)	10 mM HEPES	10 mM HEPES
Enhancing LJP	10 mM HEPES	10 mM Tris
Retarding LJP	10 mM Tris	10 mM HEPES

Table 2: Experimental solution pairings to generate an LJP to affect transport of DNA.

DNA transport was substantially affected by the buffer-induced LJP, with the primary difference between oligo DNA and the larger plasmids being the lower magnitude of diffusion revealing a blunt interface for the larger plasmids, which is evidence of the relative magnitude of electrophoretic transport (Figure 69-Figure 71, Figure 77-Figure 79). Unlike the fluorescein experiments, the retarding setup (Table 2) moves the DNA away from the interface. Because little crosses the fluid interface or channel midline, a better measure of DNA transport is the spatial displacement of the DNA, considered here by monitoring the location of 50% of maximum initial intensity. The effects of the LJP were remarkably similar between oligo and plasmid DNA (Figure 75, Figure 83), though overall

transport induced by the LJP was slightly higher for plasmids, reflecting the higher electrophoretic mobility (Table 1).

Given that the steady-state electrophoretic mobilities of both plasmid and oligo DNA are well-characterized, including the effects of salt and many buffers [145-146], it is likely that the primary issues of modeling DNA transport in a transient electric field are time-dependent. However, attempts to modify the effective mobility within COMSOL to develop over a few hundred ms were not sufficient to match the experiments (not shown). However, it did improve the performance of the model for short times, without significantly affecting the solution over longer time scales (>500 ms), and was implemented for all further models. The effective transport in the experiments were best matched by a simple reduction in overall mobility by >50%, to 1.5 x $10^{-8}\frac{m^2}{sV}$ for both forms of DNA. With this modification, concentration profiles (Figure 72-Figure 74, Figure 80-Figure 82) qualitatively matched experiments, and the quantitative deflection of the interface (Figure 76, Figure 84) agreed as well.

As the typical time scales of any intramolecular and intermolecular interactions are ns - ms, it is unlikely that this apparent low mobility is the result of counterion shielding or intramolecular rearrangements [138, 144]. Instead, it is probably an artifact of the experiment setup and the geometric simplicity of the model. Though the flow is laminar (Re = 3.3), residence time in the channel is about 5 s, which implies that Taylor dispersion is likely significant [315]. Thus, a 2D model to take the Poiseuille flow profile into account would be a better reflection of the forces in the system. However, the challenges of modeling such a complex system restrict it to the simplified 1D system, and reducing the effective mobility based upon empirical results may adequately describe this, and similar systems.

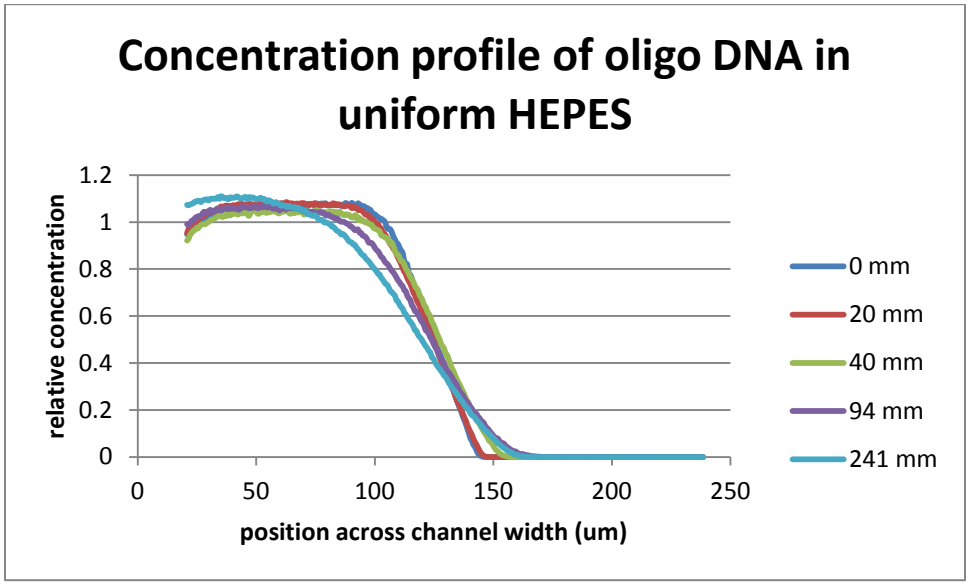

Figure 69: Diffusion of oligo DNA in uniform 10 mM HEPES, pH 7.5.

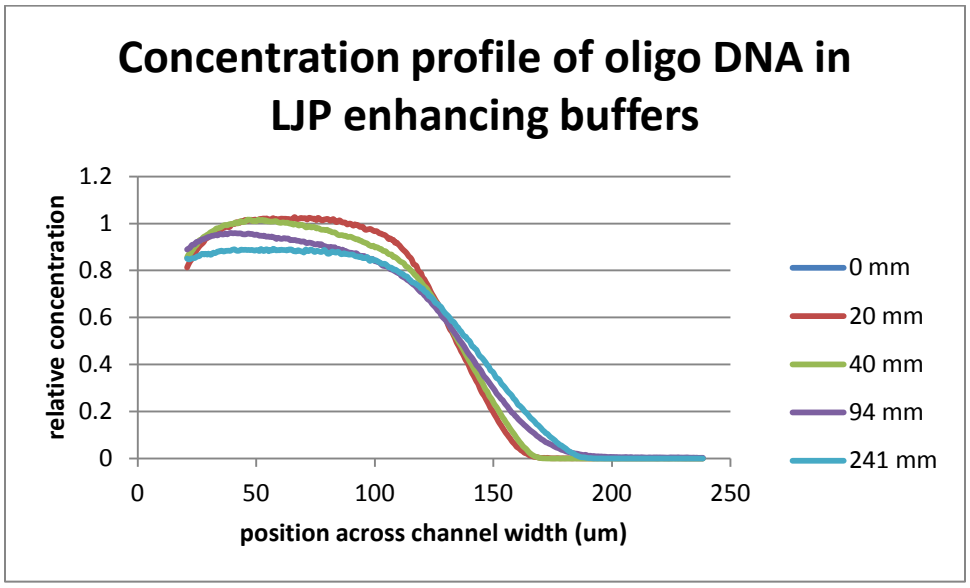

Figure 70: Transport of oligo DNA in enhancing LJP. DNA was in 10 mM HEPES, blank buffer was 10 mM Tris, both pH 7.5.

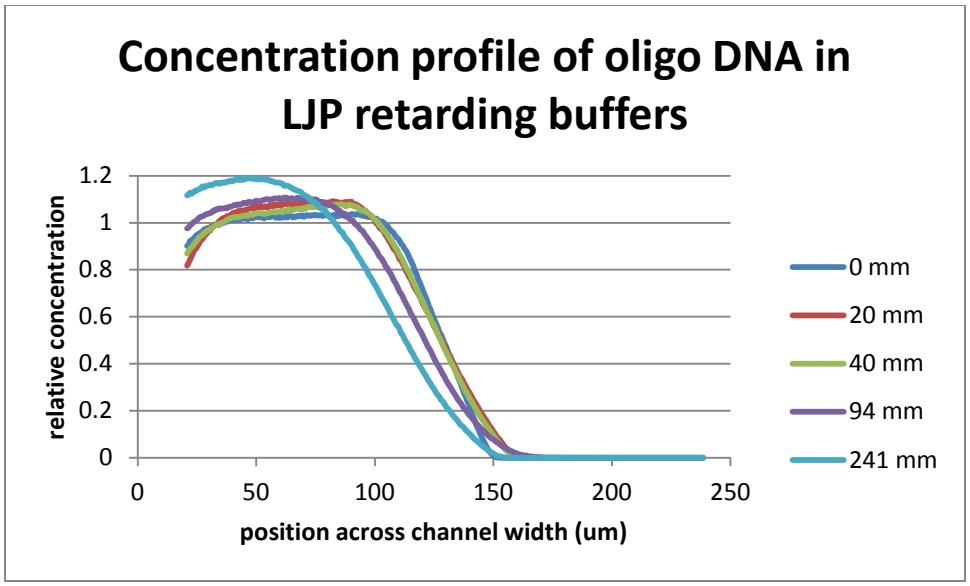

Figure 71: Transport of oligo DNA in retarding buffers. DNA was in 10 mM Tris buffer, and flowed alongside 10 mM HEPES.

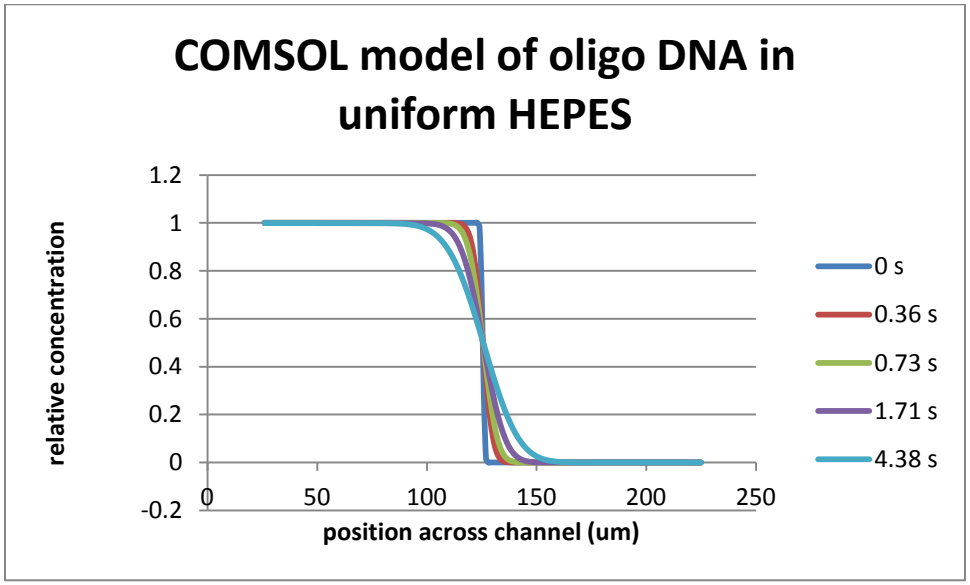

Figure 72: COMSOL model of oligo DNA diffusion in uniform 10 mM HEPES buffer, pH 7.5. Time points correspond to data collection points in wet experiments.

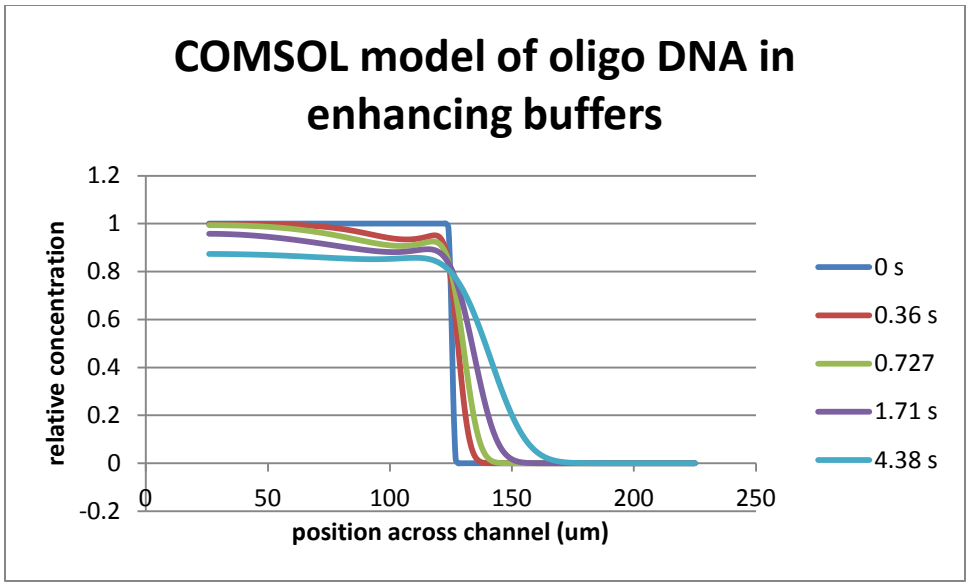

Figure 73: Transport of oligo DNA in LJP enhancing buffers. The simulation assumes the DNA is in 10 mM HEPES buffer, beside a flow of 10 mM Tris, pH 7.5. Times correspond to data intervals from wet experiments.

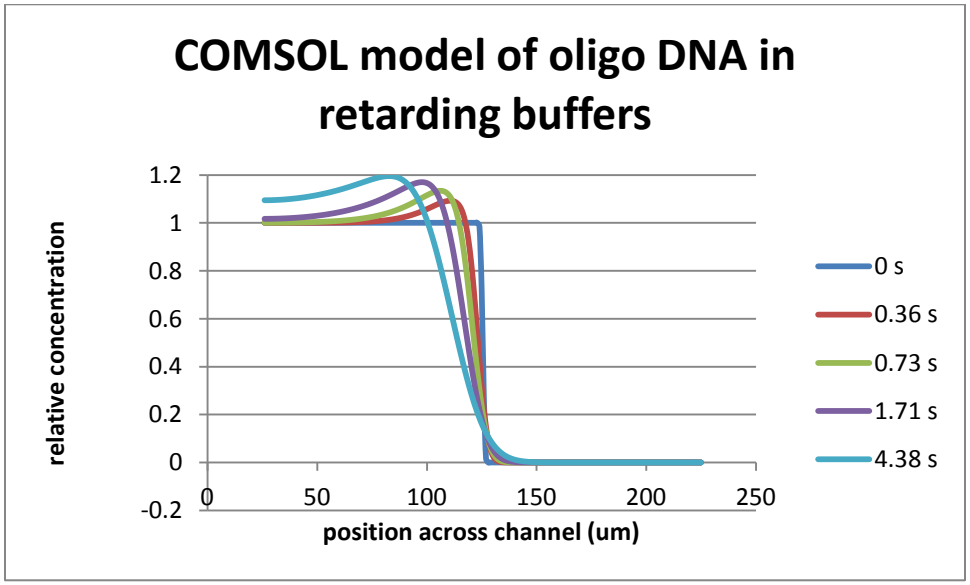

Figure 74: COMSOL model of oligo DNA transport in retarding buffers. The DNA is in 10 mM Tris, alongside a blank buffer flow of 10 mM HEPES, pH 7.5. Times selected match the locations of data collection in the wet experiments.

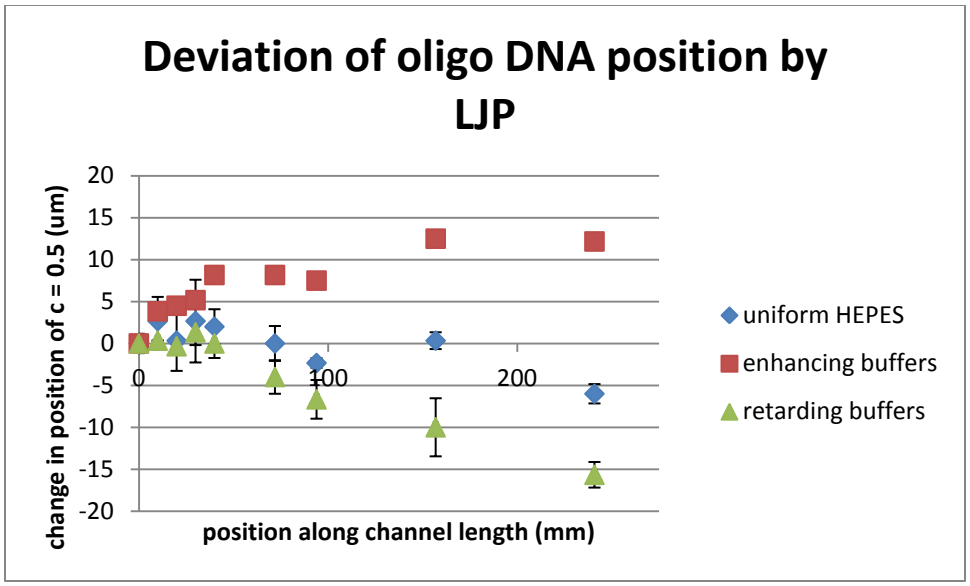

Figure 75: Change in position of the point where $c = 0.5c_{max}$ along the channel for oligo DNA under different LJP conditions. Error bars represent standard deviation (n = 3)

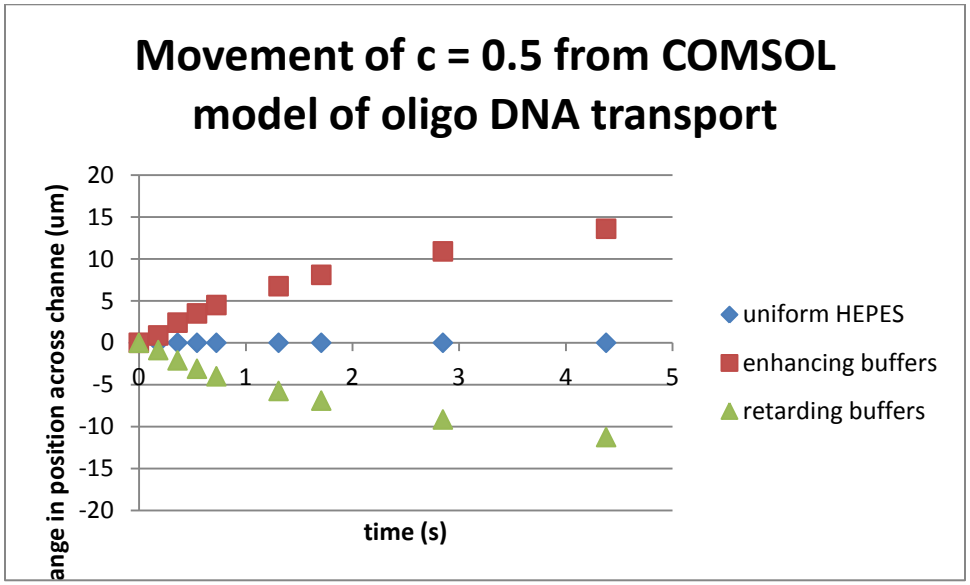

Figure 76: Deviation in the position of $c = 0.5c_{max}$ in the transport of oligo DNA in an LJP generated by 10 mM HEPES and Tris buffers.

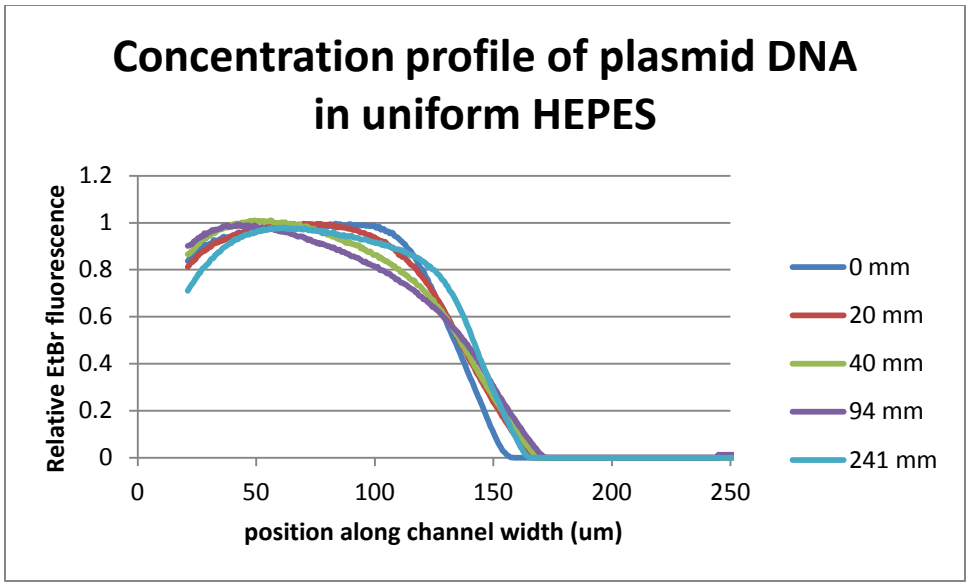

Figure 77: Transport of plasmid DNA by diffusion in uniform 10 mM HEPES, pH 7.5

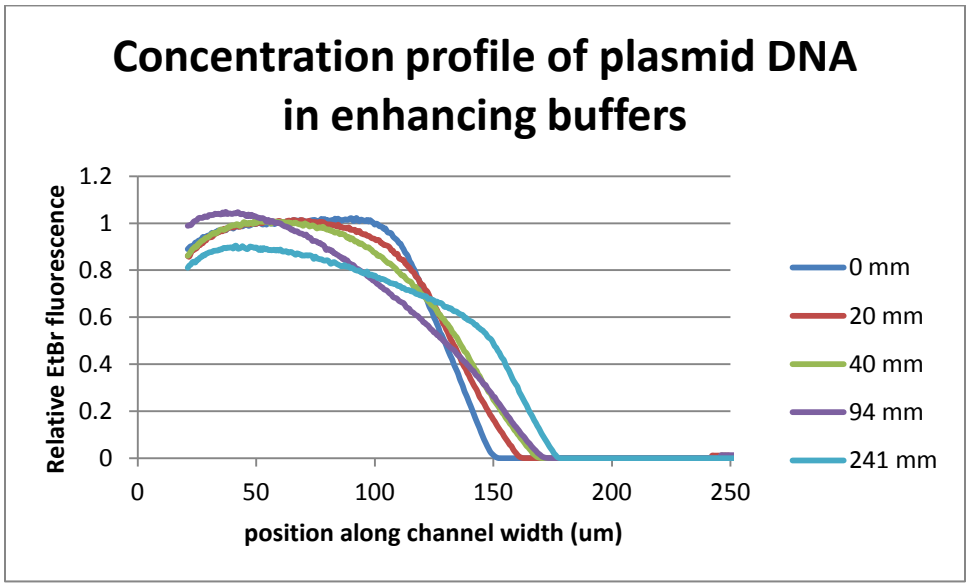

Figure 78: Transport of plasmid DNA in LJP enhancing buffers. The buffer carrying the DNA is 10 mM HEPES, while the blank fluid is 10 mM Tris, pH 7.5.

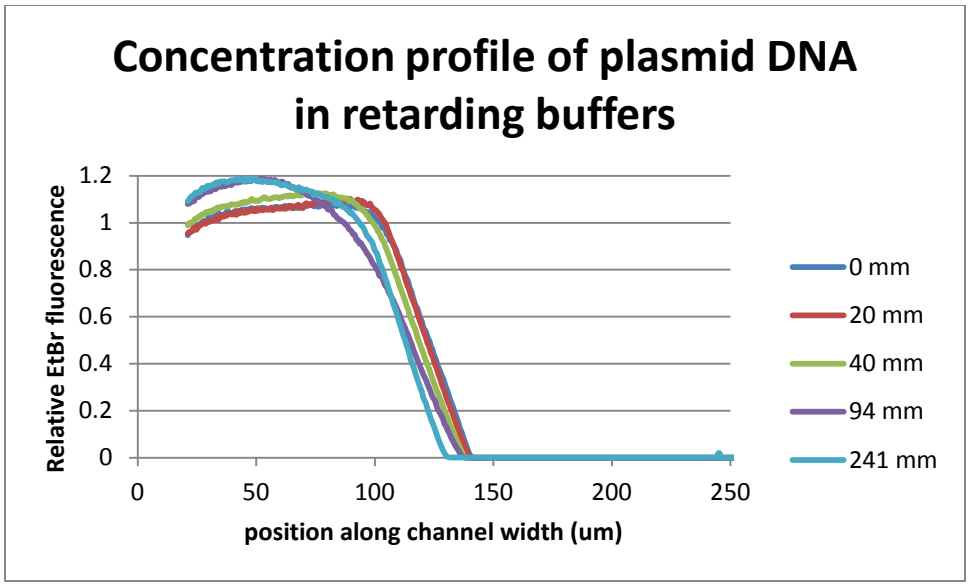

Figure 79: Transport of plasmid DNA in LJP retarding buffers. The DNA is in 10 mM Tris, flowing alongside 10 mM HEPES, pH 7.5.

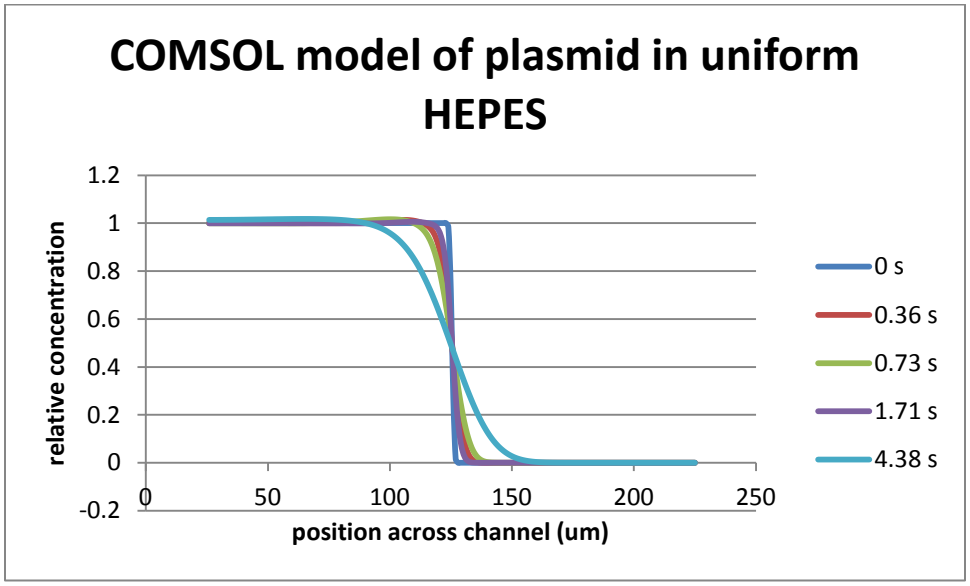

Figure 80: COMSOL model of plasmid DNA diffusion in uniform 10 mM HEPES buffer, pH 7.5. Times correspond to the location of data collection in the wet experiments.

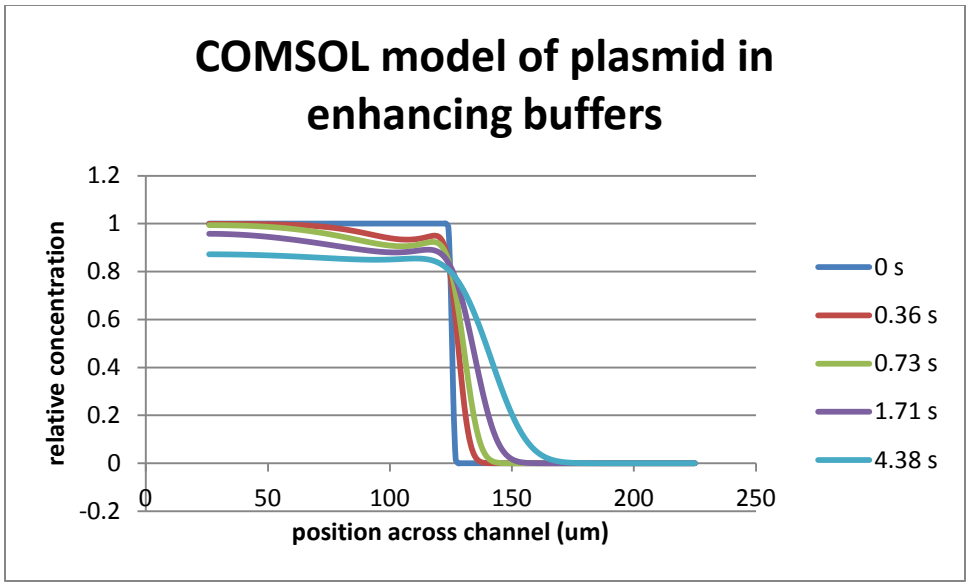

Figure 81: COMSOL model of LJP-enhanced transport of plasmid DNA. DNA is assumed to be in 10 mM HEPES buffer, next to 10 mM Tris, pH 7.5. Times correspond to data collection points in the wet experiments.

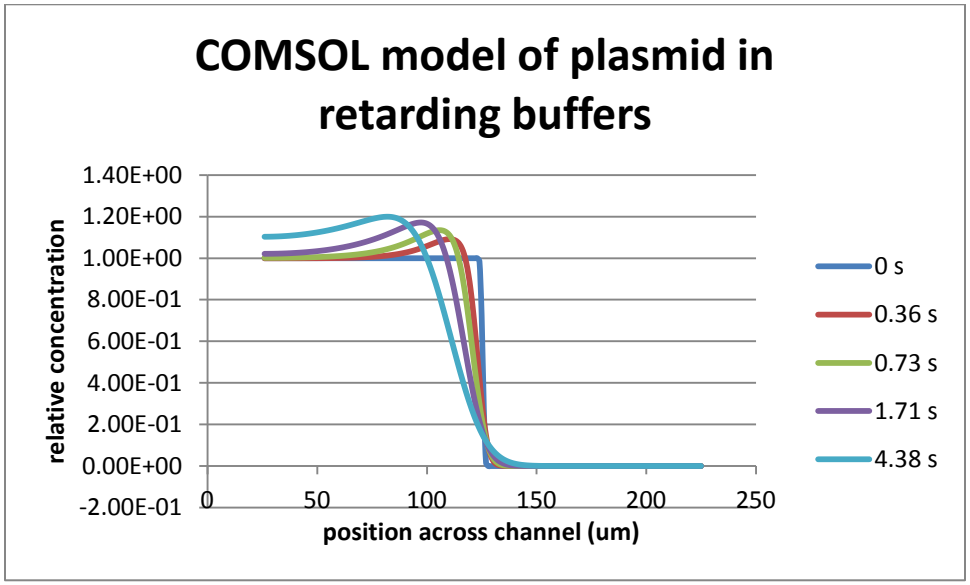

Figure 82: COMSOL model of the transport of plasmid DNA in a retarding LJP, generated by placing the DNA in 10 mM Tris buffer alongside 10 mM HEPES, pH 7.5. Times shown represent the locations of data collection from the wet experiments.

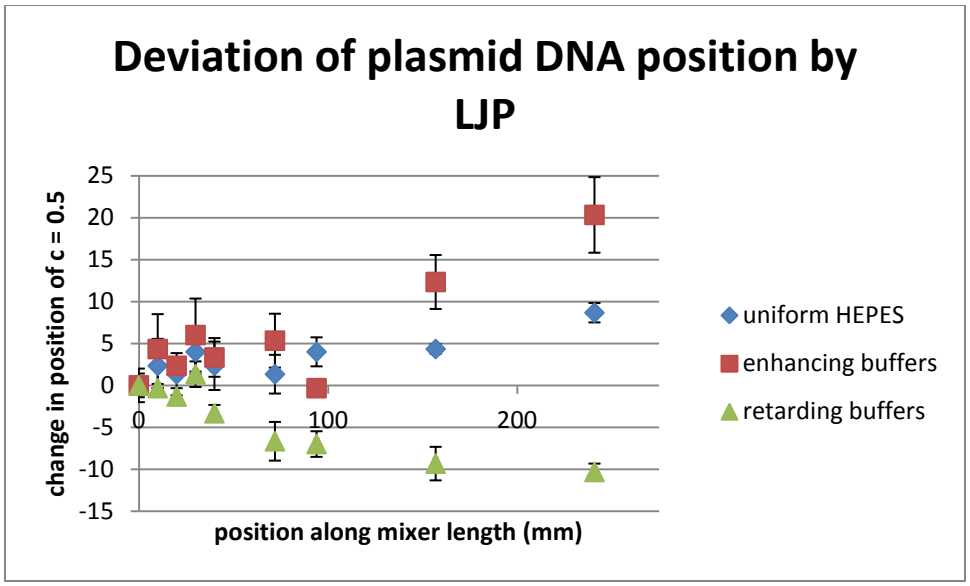

Figure 83: Change in the position of c = 0.5c_{max} for plamsid transport experiments. Error bars represent standard deviation (n = 3)

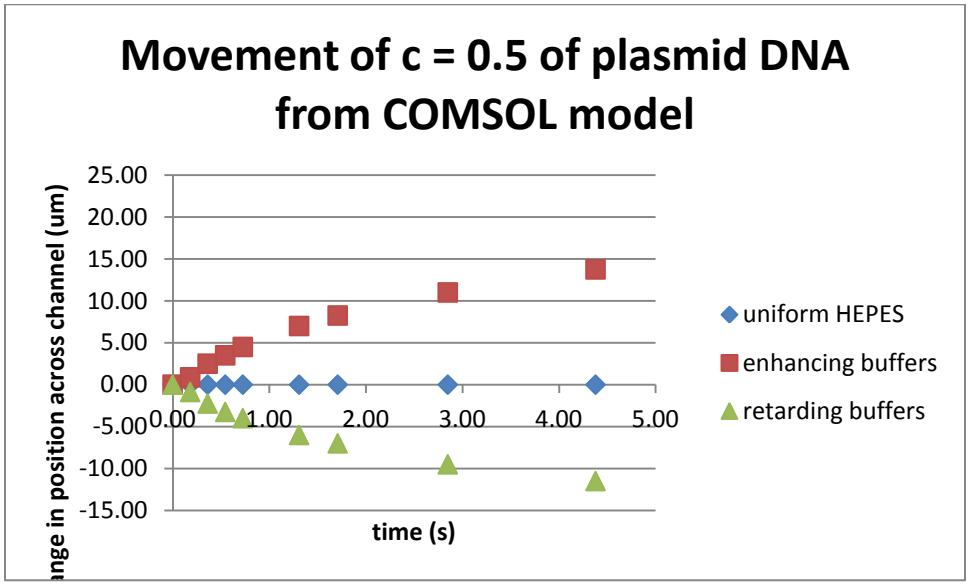

Figure 84: Change in the position of c = 0.5c_{max} from COMSOL models of plasmid transport in an LJP generated by 10 mM HEPES and Tris buffers. Time points correspond to locations in wet experiments.

The GHK estimate of potential from the buffers in the enhancing and retarding configurations was 13.5 mV, and neither form of DNA contributes substantially, due to the relative concentrations. It is interesting to note that, unlike the 4.72 mV LJP generated by 1 m salts which took about 100 ms to expand to 10 μm (Figure 59), the buffer-driven 13.5

mV field expanded to that scale in only 10 ms (Figure 86, Figure 85). This is due to the acceleration of transport of all species by the greater field strength, and the greater mobility imbalance between ion pairs. Furthermore, a slight asymmetry in the field, with greater expansion on the side containing Tris, reflects the slightly larger imbalance of diffusion (Table 1) and greater charge density of that solution. Moreover, the magnitude of peak field strength is slightly greater in the enhancing case than in the retarding case, indicating a small contribution by DNA not suggested by the GHK estimate.

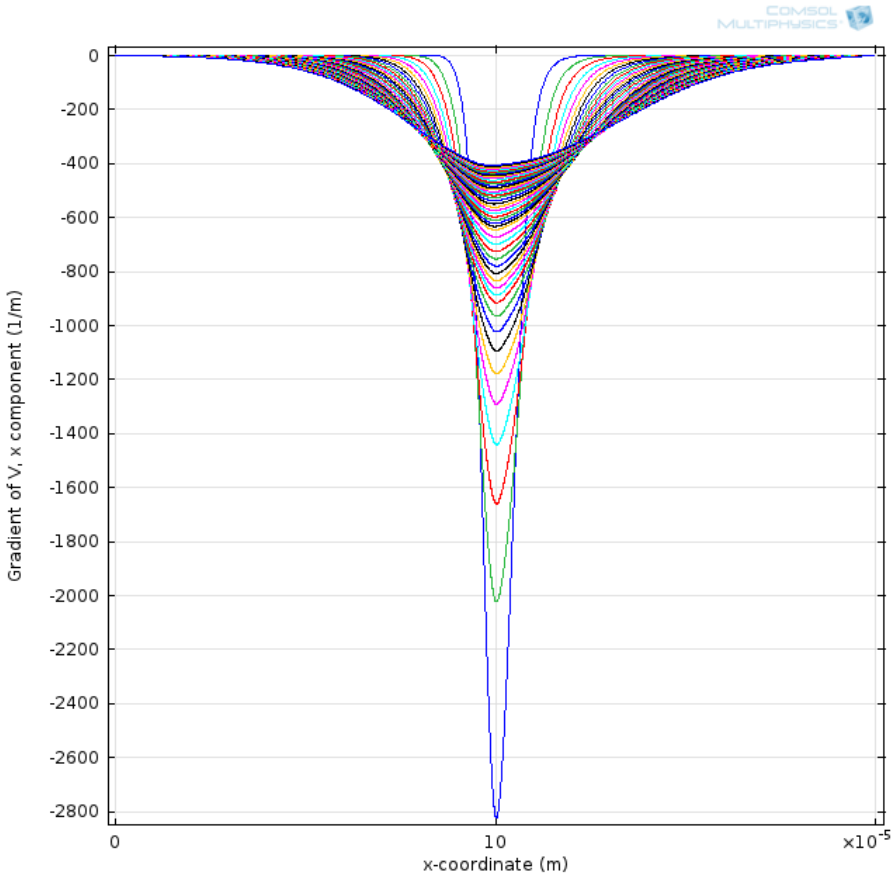

Figure 85: Electric field in the COMSOL model of plasmid DNA in an enhancing LJP. Traces represent 10 ms intervals from 10 ms to 500 ms.

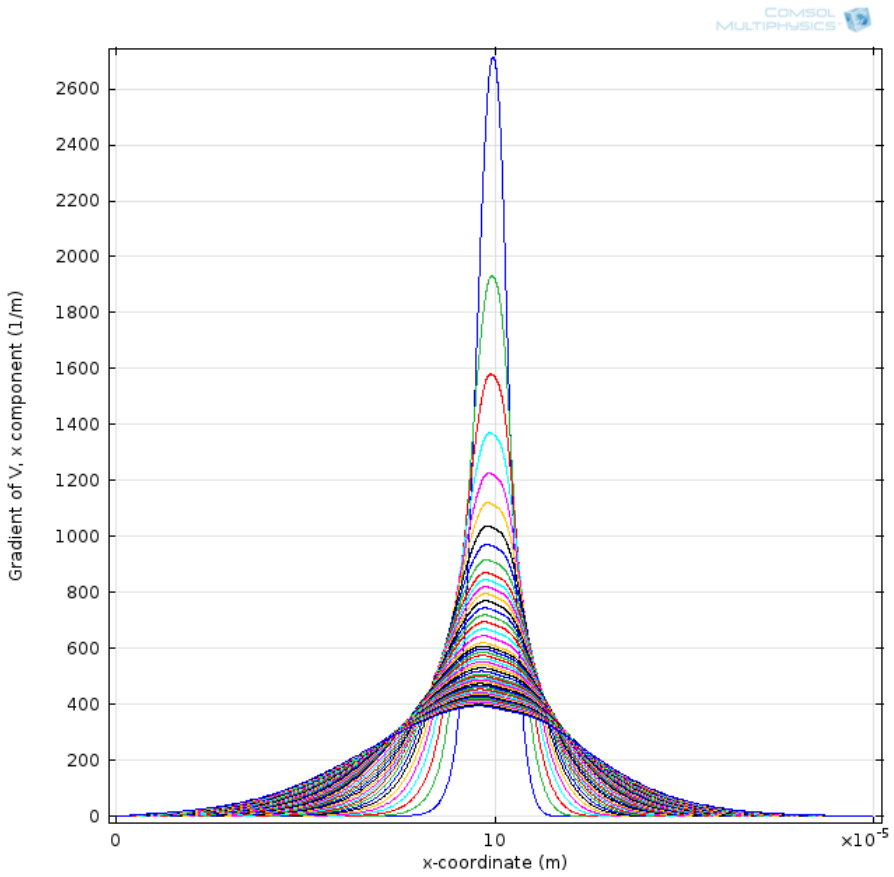

Figure 86: Electric field strength in COMSOL model of plasmid in a retarding LJP. Traces represent 10 ms intervals from t = 10 ms to t = 500 ms.

Impact of the LJP on DNA complexation

Given that the DNA/PEI complexation is transport-limited, use of the LJP to increase transport is a logical method to accelerate the interaction.

Because the LJP is most powerful over short length scales, it can be used to modify the performance of a mixer, in which length scales are reduced to homogenize concentrations. When the LJP of HEPES and Tris is combined with the advection of the SHM, a small, but measurable change in the mixing can be detected by fluorescence (Figure 87). Because the length scale within the mixer is reduced so rapidly, the complexation still takes place predominantly between 2 and 4 mixing cycles. It is interesting to note, however, the

difference in COV (Figure 88). From the inlet to beyond the first cycle of mixing, there is little difference between the three traces, as the fluid horizontal layers develop in the fluid to reduce the variation in fluorescence intensity, but overall, the mixing remains poor and little interaction occurs. However, as the mixing continues, the COV of the enhancing buffers increases, as the transport accelerates the complexation, reducing the fluorescence signal predominantly in the thin horizontal layers. The retarding buffers, on the other hand, allow advection while limiting the interaction between the DNA and PEI, keeping the COV lower until the length scales overcome transport away from the interfaces, permitting interaction. Nonetheless, the PEGylation of the PEI dominated the change in mixing speed and complexation conditions produced by the LJP in the SHM, and no significant difference in size or variability was observed (Figure 89).

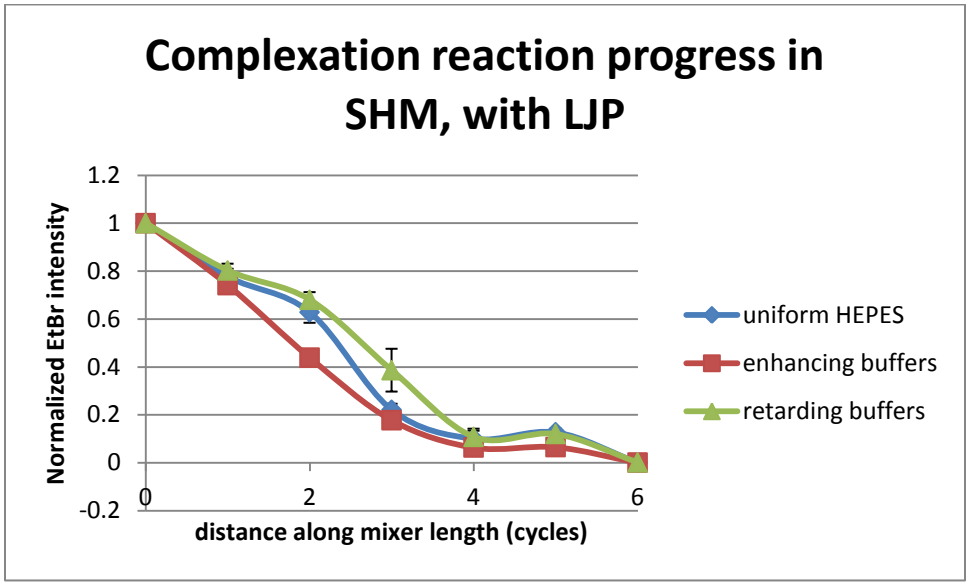

Figure 87: Impact of the LJP on DNA/PEI complexation in the SHM. The complexation was carried out at 20 µg/ml oligo DNA with PEG-PEI, N/P = 6, in 10 mM buffers, pH 7.5, and 1 µL/s flow in an SHM with a channel 300 µm wide. Error bars represent standard deviation (n = 3).

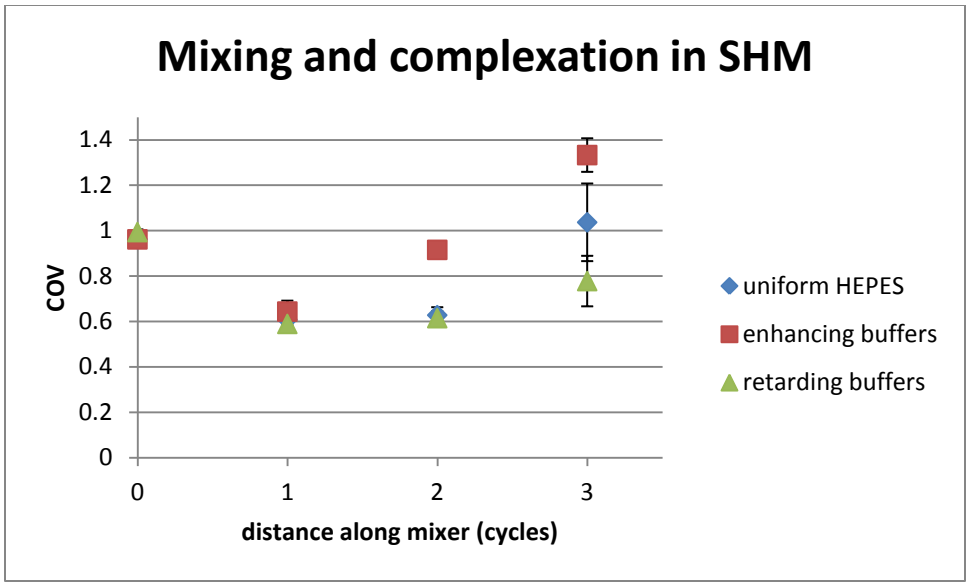

Figure 88: Coefficient of variation (COV) in the SHM, with oligo DNA complexing with PEG-PEI, and an LJP modified by HEPES and Tris buffering.

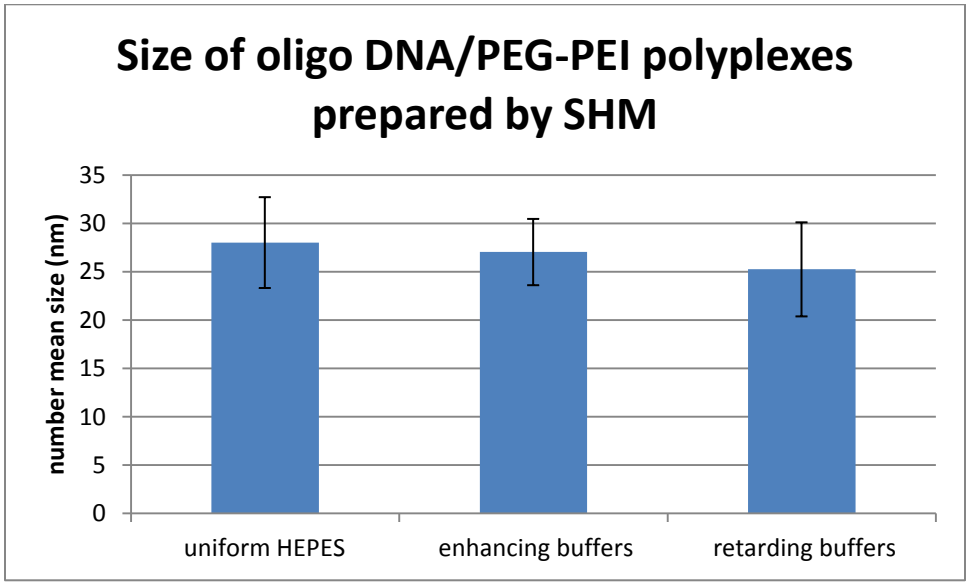

Figure 89: Number mean particle sizes of complexes of oligo DNA and PEG-PEI, prepared in an SHM with LJP-modifying buffers.

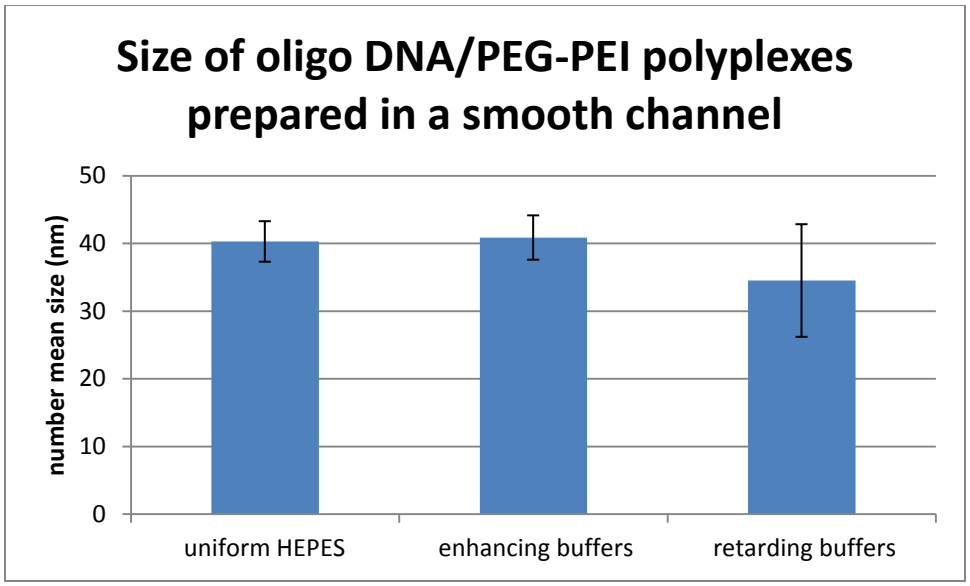

Figure 90: Number mean particle size of oligo/PEG-PEI complexes formed in a smooth channel with LJP-modifying HEPES and Tris buffers.

In Aim 1, the difference in particle size between SHM-prepared particles and those produced in a smooth channel device was hypothesized to be an indication of nucleation-growth kinetics. However, no significant difference was observed when the fraction of complexes formed in the channel versus the outlet was manipulated by LJP (Figure 90). This indicates that, though it may be a nucleation-growth system, for which a two-stage process produces nuclei upon which free material may deposit, a larger range of ratios between those first and second phases (e.g. complexation in the smooth channel and advective mixing in the outlet) may be necessary to detect it, as the PEGylated PEI is the dominant determinant of particle size.

Manipulation of the LJP by pH

Thus far, this work has emphasized the impact of the size ratio between an electrolyte and its counterion, and focused on a pair of buffers, HEPES and Tris, at a single pH and concentration to generate an LJP to move DNA. However, though both buffers are effective at regulating pH at 7.5, their differing pK_a values mean that, while HEPES is at maximal

buffering capacity with 50% of the total concentration ionized, Tris has a greater contribution to the LJP with 78% ionized. While typical buffers do not vary greatly in their asymmetry of diffusion, and there are far more acidic buffers than basic, there is a wide range of possible pK_a values, and, therefore, contributions to LJP at differing values of pH.

Table 3: Ionization state of different buffers over a range of pH. The sign indicates the direction of the charge, while the percentage corresponds to the ionized fraction.

pH	Tris	HEPES	AMPSO
6	99.1%	-3.2%	-0. 1%
6.5	97.3%	-9.5%	-0. 315%
7	91.8%	-24.9%	-0. 99%
7.5	78.0%	-51.2%	-3.1%
8	52.9%	-76.8%	-9.1
8.5	26.2%	-91.3%	-24.0%
9	10.1%	-97.1%	-50.0%
9.5	3.4%	-99.1%	-76.0%
10	1.1%	-99.7%	-90.9%

Because HEPES transitions from neutral to anionic at pH 7.5, Tris from cationic to neutral near pH 8.0, and AMPSO from neutral to anionic at pH 9.0, a combination of these three buffers can produce a broad range of potential differences over the pH range from 6.0 to 10.0. A mixture of 10 mM Tris and 15 mM HEPES, against 10 mM AMPSO was selected for the ability to reverse the direction of the LJP, then minimize it at pH is increased (Figure 91).

Experiments were carried out as before, and 75 μg/ml plasmid DNA labeled with 10 μg/ml ethidium bromide in the 10 mM Tris/15 mM HEPES buffer was flowed alongside 10 mM AMPSO in a smooth channel, and concentration profiles were assessed by fluorescence. The results show a trace nearly identical to the GHK estimates of potential (Figure 92), consistent with the hypothesis that the LJP-generated potential is the dominant transport force for plasmid DNA in this system.

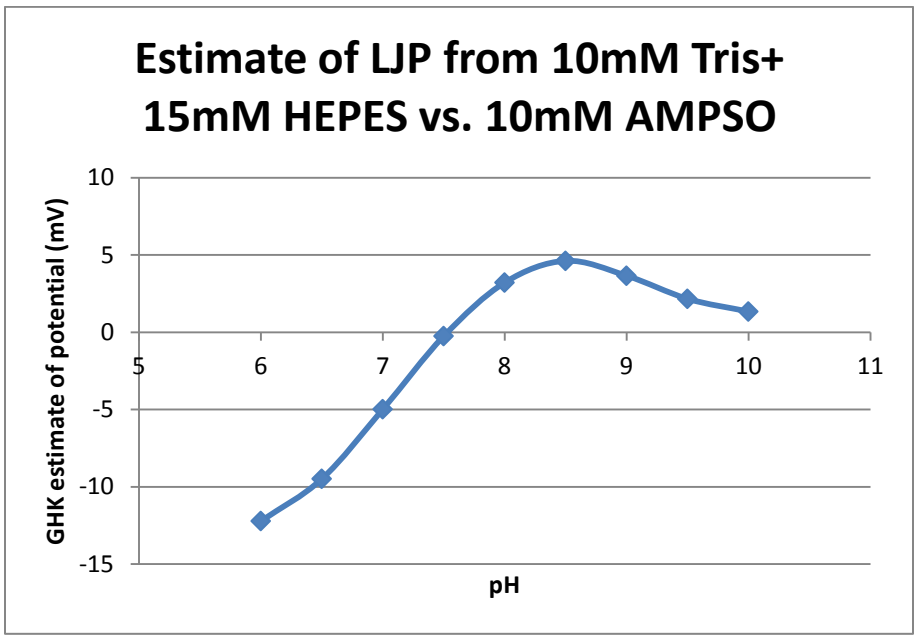

Figure 91: Magnitude of the potential difference between 10 mM Tris/15 mM HEPES and 10 mM AMPSO over a range of pH, as estimated using the modified GHK equation (Equation 16).

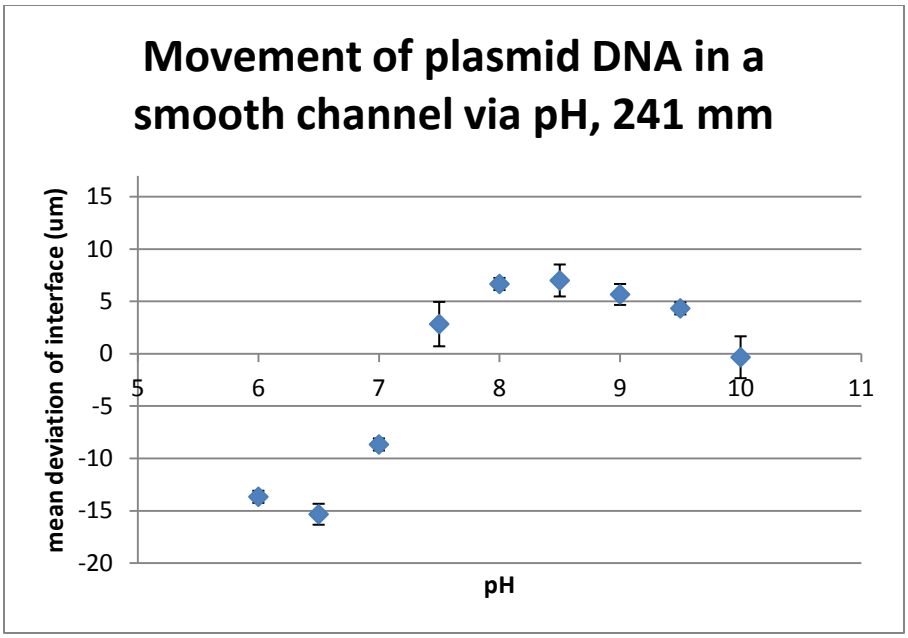

Figure 92: Mean deviation of DNA interface, measured as $c = 0.5c_{max}$ from pH-dependent LJP transport of plasmid DNA. Error bars represent standard deviation (n = 3).

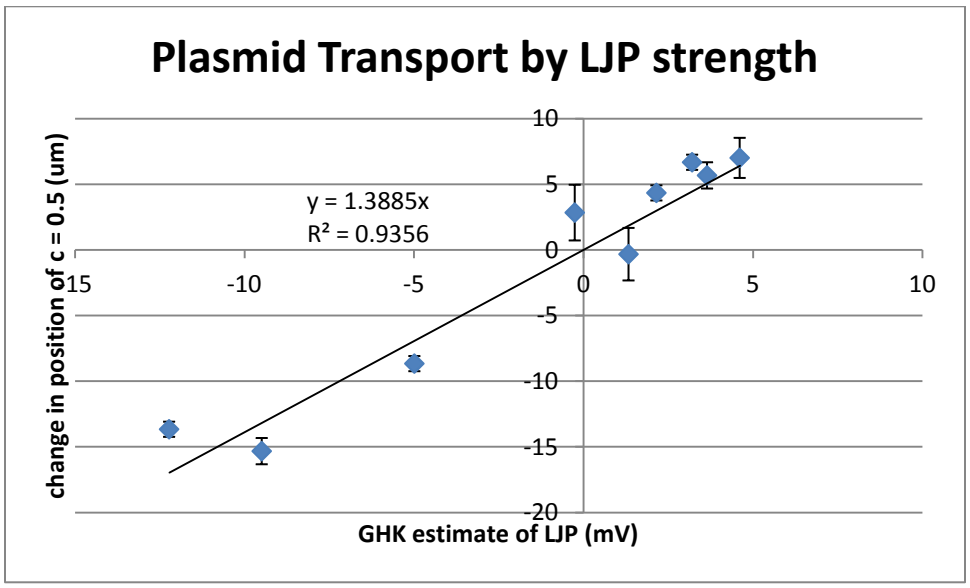

Figure 93: Relationship between field strength predicted by GHK, and measured change in the position of $c = 0.5c_{max}$ from plasmid transport experiments at 241 mm. Error bars indicate standard deviation (n = 3). Regression line was restricted to intercept at 0 to reflect that no mean transport is expected in the absence of electric field.

Transport of plasmid DNA exhibited a linear relationship with field strength (Figure 93), consistent with electrophoretic motion. Due to its low diffusivity, the transport of the plasmid in this system is dominated by electrophoretic mobility. Furthermore, the metric

chosen, change in position of $c = 0.5c_{max}$, only measures the direction and magnitude of bulk transport, such as electrophoresis. Diffusion at an interface is random, and therefore does not change the mean location of the solute. The slope of the regression line reflects the observed mobility in the system, including the transient nature of the field, the effects of Taylor dispersion in the flow conditions, and any polyelectrolyte or solvent interactions. This information could be used to more precisely control LJP motion by selectively tuning the field to produce or suppress an arbitrary direction and magnitude of motion.

Discussion

Due to its size, DNA is slow to diffuse, and processes involving it are frequently regarded as transport-limited. However, because it is a highly-charged polyelectrolyte, it is extremely sensitive to the ionic environment, and simple buffer and pH choice can dramatically impact its behavior. It is likely that, through mechanisms such as counterion shielding and intramolecular rearrangement, the electrophoretic mobility of DNA does develop over time, as might its contributions to the potential field, though these effects are more likely measured in ms than s, and the apparent reduced mobility is an effect of Taylor dispersion. A 2D model of the LJP would be interesting, but is beyond current capabilities. Even the addition of a third buffer equilibrium to simulate the pH-dependent setup destabilized the model sufficiently to preclude a solution. However, some information on the effects of dispersion might be obtained via confocal microcopy, or use of a wider, flatter channel with lower flow rate to reduce Taylor dispersion, and comparisons between fluorescein, a well-behaved electrolyte to evaluate the LJP, and ethidium-labeled DNA might reveal whether complex polyelectrolyte behavior has an impact over scales of ms and μm. Though nuances of DNA behavior may be better understood via molecule-level methods, such as nuclear magnetic resonance, fluorescence resonance energy transfer, surface probe microscopy, or

molecular dynamics simulations, or at least more rigorous determination of transient electrophoretic phenomena, this study demonstrates the impact of this behavior on the practical level of experimentation and fabrication.

The difference in size of oligo DNA/PEG-PEI polyplexes formed in a smooth channel versus the SHM in Aim 1 does suggest that nucleation/growth may be a factor in the formation of these nanoparticles, but the size of these particles is much more significantly regulated by the PEGylation of the PEI. To tease out further information would require a broader range of two-stage mixing ratios, and more sensitive size measurement, though a system with a larger dynamic range (e.g. unmodified PEI) may indicate a trend.

Another interesting application of the LJP might be to prevent aggregation within devices such as the SHM. Deposition of material is facilitated both by abundance of surface interactions within the efficient micromixer and by the shear environment around the grooves. However, a retarding LJP enables some degree of advection, reducing the length scales for diffusion of larger species, while keeping those species separate for some length of time. If an SHM were designed with the mixer only long enough to stir the solutions until the LJP collapsed, the complexation would only take place after the mixing unit, preventing buildup in the mixer, and only once the contents were somewhat stirred, producing a more even range of concentration ratios and a more uniform complexation.

Furthermore, this work demonstrates the power of electrostatics in any interaction of polyelectrolytes. Simple selection of buffers may enable acceleration or delays of transport, allowing temporal or spatial control within a device. Inclusion of certain species may aid in extraction or purification in an H-filter or similar setup. While the previous work on LJP transport in a microchannel relied upon concentrated salts, relatively dilute buffers are

sufficient to generate even larger potentials, tunable by pH, and considerably more practical and compatible with a broader range of systems.

Discussion and Future Work

Though the two devices presented here, the SHM and the SFD, do reveal much about the process of polyplex formation, neither is directly suitable for use for the production of nucleic acid therapeutics. The magnitude of surface interactions and shear lead to buildup on the walls of the SHM; reducing concentration further to lower the rate of accumulation would merely increase the run time necessary to produce a relevant quantity of nanoparticles. What is required to render the mixer useful is a method of preventing complexation during advection—which may be achievable by using a retarding LJP, and limiting the mixer length, though long residence times in the grooves may still lead to aggregate buildup and material loss. Nevertheless, the experiments do demonstrate a moderate dependence of size upon mixing time, and the sensitivity of the process to shear.

The SFD, on the other hand, produced nanoparticles of significantly smaller size, with no observable aggregation. The disadvantage of the device is that, though the engineering principle is simple, the actual fabrication and operation of the device is unnecessarily complex. For the setup used here, only 4 μg of DNA was complexed during a 5-minute pump cycle, and material in the device was subject to variable conditions during the pump refill. These flow rate and volume issues could be overcome with a simpler design, and use of pumps capable of longer continuous operation (e.g. those used for HPLC). With more stable flow, it might be possible to use higher concentrations, which would then enable the processing of a few hundred μg or more of DNA, which may be suitable for laboratory use. However, the device does not really lend itself to scaling up, and would still be inadequate for commercial production.

A biphasic strategy to confine the complexation to a low-shear zone of the device may be the best option to limit fouling and obtain small, uniform nanoparticles without wasting

material. A droplet micromixer is just such a device, and has shown improved polyplexes relative to bulk mixing [207]. However, a comparison to other mixing methods, such as an SHM or straight channel, would be necessary to establish if the improvement is due to the low shear, or merely the controlled introduction of fluids [26, 204, 209]. And, as with all microdevices, a scale-up strategy is necessary to have clinical relevance.

Though the PEGylated PEI was used primarily to limit fluorescent aggregation in the SHM, it clearly was a strong limiter of size. Given that it is known to both improve nanoparticle stability and circulation time, as well as reduce toxicity, it is clearly an excellent addition to polyplex formulations [29-30, 164]. However, by limiting the size, the DLS signal was reduced to the point that further variations in size and polydispersity were difficult to detect. As size is such a crucial determinant of behavior *in vivo*, improved methods and standards of size measurement are needed to better characterize nanoparticles [47, 127, 270, 272-273]. In the absence of a new, ultra-sensitive method, such formulations of small particles will need to be concentrated to obtain a sufficient signal to observe the impact of preparation on PEGylated systems. However, even modest improvements in size and variability, which may be achieved *via* microfluidic control, might result in a clinically relevant reduction in toxicity or increase in efficacy.

Lastly, control of mixing is essentially control of transport, and, while this is classically approached by mechanically reducing the length scale (i.e. advection or stirring), it can also be achieved by passive manipulation of transport. Given that the LJP has a substantial effect on transport over ~ 10 μm length scales, with only the use of 10 mM conventional buffers, it is not difficult to imagine other ways to put the principle into use. For instance, a retarding LJP could be used to concentrate a charged material of interest toward one side of the channel. Or a channel embedded in a charged hydrogel could more effectively restrict

material to the channel, while the buffer and smaller ions are exchanged in rapid dialysis. At the very least, it shows that the behavior of even dilute charged species is complex at the microscale.

Closure

The principles presented here for the improvement of polyplex assembly have the potential to improve the safety and efficacy of nucleic acid therapeutics. However, they are also applicable to the fabrication of any polymer or liposome-based nanomedicine. Traditional pharmaceuticals rely predominantly upon chemistry and specific interactions, but nanomedicine blurs the boundary between chemicals and materials. Size is a crucial determinant of *in vivo* behavior, and a parameter of nanomedicine that deserves greater attention. The minute details of physical interactions, over scales of nm - μm, and times of ms - s are not often considered, but, in the face of nanotechnology, these scales are of increasing importance. Such considerations will enable safer, more effective nanotherapies, with the possibility of faster development and reduced cost.

References

1. Häggström, M. *Surface anatomy of the heart*. 2009; Available from: http://en.wikipedia.org/wiki/File:Surface_anatomy_of_the_heart.png.
2. Goodsell, D. *Serum Albumin*. Moecule of the Month 2003; Available from: http://dx.doi.org/10.2210/rcsb_pdb/mom_2003_1.
3. Moghimi, S.M., A.C. Hunter, and J.C. Murray, *Nanomedicine: current status and future prospects.* Faseb Journal, 2005. **19**(3): p. 311-30.
4. Watson, A., X. Wu, and M. Bruchez, *Lighting up cells with quantum dots.* Biotechniques, 2003. **34**(2): p. 296-300, 302-3.
5. Gao, X., L.W. Chung, and S. Nie, *Quantum dots for in vivo molecular and cellular imaging.* Methods Mol Biol, 2007. **374**: p. 135-45.
6. Gao, X., et al., *In vivo cancer targeting and imaging with semiconductor quantum dots.* Nature Biotechnology, 2004. **22**(8): p. 969-76.
7. Zhang, J., R. Badugu, and J.R. Lakowicz, *Fluorescence Quenching of CdTe Nanocrystals by Bound Gold Nanoparticles in Aqueous Solution.* Plasmonics, 2008. **3**(1): p. 3-11.
8. Li, H., et al., *Selective quenching of fluorescence from unbound oligonucleotides by gold nanoparticles as a probe of RNA structure.* RNA, 2007. **13**(11): p. 2034-41.
9. Dousset, V., et al., *Comparison of ultrasmall particles of iron oxide (USPIO)-enhanced T2-weighted, conventional T2-weighted, and gadolinium-enhanced T1-weighted MR images in rats with experimental autoimmune encephalomyelitis.* AJNR Am J Neuroradiol, 1999. **20**(2): p. 223-7.
10. Perez, J.M., L. Josephson, and R. Weissleder, *Use of magnetic nanoparticles as nanosensors to probe for molecular interactions.* Chembiochem, 2004. **5**(3): p. 261-4.
11. Jokerst, J.V., et al., *Nanoparticle PEGylation for imaging and therapy.* Nanomedicine (Lond), 2011. **6**(4): p. 715-28.
12. Seip, R., et al., *Targeted ultrasound-mediated delivery of nanoparticles: on the development of a new HIFU-based therapy and imaging device.* IEEE Trans Biomed Eng, 2010. **57**(1): p. 61-70.
13. Zhang, L., et al., *Nanoparticles in medicine: therapeutic applications and developments.* Clin Pharmacol Ther, 2008. **83**(5): p. 761-9.
14. Parveen, S., R. Misra, and S.K. Sahoo, *Nanoparticles: a boon to drug delivery, therapeutics, diagnostics and imaging.* Nanomedicine, 2012. **8**(2): p. 147-66.
15. Schutz, C.A., et al., *Therapeutic nanoparticles in clinics and under clinical evaluation.* Nanomedicine, 2013. **8**(3): p. 449-467.
16. Foged, C., et al., *Particle size and surface charge affect particle uptake by human dendritic cells in an in vitro model.* Int J Pharm, 2005. **298**(2): p. 315-22.
17. Wermuth, C.G., *The practice of medicinal chemistry*. 3rd ed. 2011, Amsterdam ; London: Academic Press. xiv, 982 p.
18. Sahu, S.C. and D. Casciano, *Nanotoxicity : from in vivo and in vitro models to health risks*. 2009, Chichester, West Sussex, UK: John Wiley. xviii, 609 p., 4 p. of col. plates.
19. Moghimi, S.M., A.C. Hunter, and J.C. Murray, *Long-circulating and target-specific nanoparticles: theory to practice.* Pharmacol Rev, 2001. **53**(2): p. 283-318.
20. Aggarwal, P., et al., *Nanoparticle interaction with plasma proteins as it relates to particle biodistribution, biocompatibility and therapeutic efficacy.* Adv Drug Deliv Rev, 2009. **61**(6): p. 428-37.
21. *Veins*. Human Body [cited 2013 April 23]; Available from: http://dx.doi.org/10.2210/rcsb_pdb/mom_2003_1.

22. Kedmi, R., N. Ben-Arie, and D. Peer, *The systemic toxicity of positively charged lipid nanoparticles and the role of Toll-like receptor 4 in immune activation.* Biomaterials, 2010. **31**(26): p. 6867-75.
23. Deng, Z.J., et al., *Nanoparticle-induced unfolding of fibrinogen promotes Mac-1 receptor activation and inflammation.* Nat Nanotechnol, 2011. **6**(1): p. 39-44.
24. Bailon, P. and C.Y. Won, *PEG-modified biopharmaceuticals.* Expert Opin Drug Deliv, 2009. **6**(1): p. 1-16.
25. Garay, R.P. and J.P. Labaune, *Immunogenicity of Polyethylene Glycol (PEG).* The Open Conference Proceedings Journal, 2011. **2**: p. 104-107.
26. Endres, T., et al., *Optimising the self-assembly of siRNA loaded PEG-PCL-lPEI nano-carriers employing different preparation techniques.* Journal of Controlled Release, 2012. **160**(3): p. 583-591.
27. Hong, K., et al., *Stabilization of cationic liposome-plasmid DNA complexes by polyamines and poly(ethylene glycol)-phospholipid conjugates for efficient in vivo gene delivery.* FEBS Lett, 1997. **400**(2): p. 233-7.
28. Kursa, M., et al., *Novel shielded transferrin-polyethylene glycol-polyethylenimine/DNA complexes for systemic tumor-targeted gene transfer.* Bioconjugate Chemistry, 2003. **14**(1): p. 222-231.
29. Merdan, T., et al., *PEGylation of poly(ethylene imine) affects stability of complexes with plasmid DNA under in vivo conditions in a dose-dependent manner after intravenous injection into mice.* Bioconjugate Chemistry, 2005. **16**(4): p. 785-792.
30. Ogris, M., et al., *PEGylated DNA/transferrin-PEI complexes: reduced interaction with blood components, extended circulation in blood and potential for systemic gene delivery.* Gene Therapy, 1999. **6**(4): p. 595-605.
31. Dobrovolskaia, M.A., et al., *Preclinical studies to understand nanoparticle interaction with the immune system and its potential effects on nanoparticle biodistribution.* Mol Pharm, 2008. **5**(4): p. 487-95.
32. Sheftel, V.O., *Indirect Food Additives and Polymers: Migration and Toxicology*. 2000: CRC.
33. Decuzzi, P., et al., *A theoretical model for the margination of particles within blood vessels.* Annals of Biomedical Engineering, 2005. **33**(2): p. 179-190.
34. Caldorera-Moore, M., et al., *Designer nanoparticles: incorporating size, shape and triggered release into nanoscale drug carriers.* Expert Opin Drug Deliv, 2010. **7**(4): p. 479-95.
35. Canelas, D.A., K.P. Herlihy, and J.M. DeSimone, *Top-down particle fabrication: control of size and shape for diagnostic imaging and drug delivery.* Wiley Interdiscip Rev Nanomed Nanobiotechnol, 2009. **1**(4): p. 391-404.
36. Champion, J.A., Y.K. Katare, and S. Mitragotri, *Making polymeric micro- and nanoparticles of complex shapes.* Proc Natl Acad Sci U S A, 2007. **104**(29): p. 11901-4.
37. Decuzzi, P., et al., *Size and shape effects in the biodistribution of intravascularly injected particles.* Journal of Controlled Release, 2010. **141**(3): p. 320-7.
38. Euliss, L.E., et al., *Imparting size, shape, and composition control of materials for nanomedicine.* Chemical Society Reviews, 2006. **35**(11): p. 1095-104.
39. Pouton, C.W. and L.W. Seymour, *Key issues in non-viral gene delivery.* Advanced Drug Delivery Reviews, 2001. **46**(1-3): p. 187-203.
40. Nishikawa, M. and L. Huang, *Nonviral vectors in the new millennium: Delivery barriers in gene transfer.* Human Gene Therapy, 2001. **12**(8): p. 861-870.
41. Mukherjee, S., R.N. Ghosh, and F.R. Maxfield, *Endocytosis.* Physiol Rev, 1997. **77**(3): p. 759-803.
42. Zhang, S., et al., *Size-Dependent Endocytosis of Nanoparticles.* Advanced Materials, 2009. **21**: p. 419-424.

43. Conner, S.D. and S.L. Schmid, *Regulated portals of entry into the cell.* Nature, 2003. **422**(6927): p. 37-44.
44. Gaumet, M., et al., *Nanoparticles for drug delivery: the need for precision in reporting particle size parameters.* European Journal of Pharmaceutics and Biopharmaceutics, 2008. **69**(1): p. 1-9.
45. Miller, J., *Beyond biotechnology: FDA regulation of nanomedicine.* Columbia Sci Technol Law Rev, 2003. **4**: p. E5.
46. *Regulating nanomedicine.* Nat Mater, 2007. **6**(4): p. 249.
47. Eschenbach, A.C.v., *Nanotechnology: A Report of the U.S. Food and Drug Administration Nanotechnology Task Force*. 2007, Department of Health and Human Services: Rockville, MD. p. 36.
48. Vollmer, S. (2011) *Does the FDA ensure that nanotech medicines are safe?* Science in the Triangle.
49. *Center for Drug Evaluation and Research Nanotechnology Programs*. 2012 July 5, 2012 [cited 2013 March 29, 2013]; Available from: www.fda.gov/ScienceResearch/SpecialTopics/Nanotechnology/ucm309677.htm.
50. Prasher, D., R.O. Mccann, and M.J. Cormier, *Cloning and Expression of the Cdna Coding for Aequorin, a Bioluminescent Calcium-Binding Protein.* Biochemical and Biophysical Research Communications, 1985. **126**(3): p. 1259-1268.
51. Thompson, J.F., L.S. Hayes, and D.B. Lloyd, *Modulation of Firefly Luciferase Stability and Impact on Studies of Gene-Regulation.* Gene, 1991. **103**(2): p. 171-177.
52. Hammer, R.E., et al., *Spontaneous inflammatory disease in transgenic rats expressing HLA-B27 and human beta 2m: an animal model of HLA-B27-associated human disorders.* Cell, 1990. **63**(5): p. 1099-112.
53. Keffer, J., et al., *Transgenic mice expressing human tumour necrosis factor: a predictive genetic model of arthritis.* Embo Journal, 1991. **10**(13): p. 4025-31.
54. Miller, W.L. and J.D. Baxter, *Recombinant DNA--a new source of insulin.* Diabetologia, 1980. **18**(6): p. 431-6.
55. Baxter, J.D., *Recombinant DNA and medical progress.* Hosp Pract, 1980. **15**(2): p. 57-67.
56. Clark, S.C. and R. Kamen, *The human hematopoietic colony-stimulating factors.* Science, 1987. **236**(4806): p. 1229-37.
57. Miller, A.D., *Human gene therapy comes of age.* Nature, 1992. **357**(6378): p. 455-60.
58. Dachs, G.U., et al., *Targeting gene therapy to cancer: a review.* Oncol Res, 1997. **9**(6-7): p. 313-25.
59. Ginn, S.L., et al., *Gene therapy clinical trials worldwide to 2012 - an update.* Journal of Gene Medicine, 2013. **15**(2): p. 65-77.
60. Remy, J.S., et al., *Gene transfer with lipospermines and polyethylenimines.* Advanced Drug Delivery Reviews, 1998. **30**(1-3): p. 85-95.
61. Herzog, R.W., O. Cao, and A. Srivastava, *Two Decades of Clinical Gene Therapy - Success Is Finally Mounting.* Discovery Medicine, 2010. **45**: p. 105-111.
62. Stephenson, M.L. and P.C. Zamecnik, *Inhibition of Rous sarcoma viral RNA translation by a specific oligodeoxyribonucleotide.* Proc Natl Acad Sci U S A, 1978. **75**(1): p. 285-8.
63. Dominski, Z. and R. Kole, *Restoration of correct splicing in thalassemic pre-mRNA by antisense oligonucleotides.* Proc Natl Acad Sci U S A, 1993. **90**(18): p. 8673-7.
64. Nyce, J.W. and W.J. Metzger, *DNA antisense therapy for asthma in an animal model.* Nature, 1997. **385**(6618): p. 721-5.
65. Vickers, T.A., et al., *Fully modified 2' MOE oligonucleotides redirect polyadenylation.* Nucleic Acids Research, 2001. **29**(6): p. 1293-9.

66. Volloch, V., B. Schweitzer, and S. Rits, *Inhibition of pre-mRNA splicing by antisense RNA in vitro: effect of RNA containing sequences complementary to introns.* Biochem Biophys Res Commun, 1991. **179**(3): p. 1600-5.
67. Achenbach, T.V., B. Brunner, and K. Heermeier, *Oligonucleotide-based knockdown technologies: antisense versus RNA interference.* Chembiochem, 2003. **4**(10): p. 928-35.
68. Mulamba, G.B., et al., *Human cytomegalovirus mutant with sequence-dependent resistance to the phosphorothioate oligonucleotide fomivirsen (ISIS 2922).* Antimicrob Agents Chemother, 1998. **42**(4): p. 971-3.
69. *Annual Report Pursuant to Section 13 or 15(d) of the securities Exchange Act of 1934*. 2008, Isis Pharmaceuticals, Inc.: Carlsbad, CA.
70. Ecker, J.R. and R.W. Davis, *Inhibition of gene expression in plant cells by expression of antisense RNA.* Proc Natl Acad Sci U S A, 1986. **83**(15): p. 5372-6.
71. Fire, A., et al., *Potent and specific genetic interference by double-stranded RNA in Caenorhabditis elegans.* Nature, 1998. **391**(6669): p. 806-11.
72. Fire, A.Z. and C.C. Mello. *Advanced Information on The Nobel Prize in Physiology or Medicine 2006: RNA Interference*. 2006 [cited 2013; Available from: http://web.archive.org/web/20070120113455/http://nobelprize.org/nobel_prizes/medicine/laureates/2006/adv.html.
73. Alexopoulou, L., et al., *Recognition of double-stranded RNA and activation of NF-kappaB by Toll-like receptor 3.* Nature, 2001. **413**(6857): p. 732-8.
74. Doench, J.G., C.P. Petersen, and P.A. Sharp, *siRNAs can function as miRNAs.* Genes Dev, 2003. **17**(4): p. 438-42.
75. Pushparaj, P.N., et al., *RNAi and RNAa--the yin and yang of RNAome.* Bioinformation, 2008. **2**(6): p. 235-7.
76. Timmerman, L. (2010) *Merck's Alan Sachs, on RNAi's Big Challenge: Delivery, Delivery, Delivery*. 5.
77. Haussecker, D., *The business of RNAi therapeutics.* Human Gene Therapy, 2008. **19**(5): p. 451-62.
78. Haussecker, D., *The Business of RNAi Therapeutics in 2012.* Mol Ther Nucleic Acids, 2012. **1**: p. e8.
79. Crowe, S., *Suppression of chemokine receptor expression by RNA interference allows for inhibition of HIV-1 replication, by Martinez et al.* AIDS, 2003. **17 Suppl 4**: p. S103-5.
80. Mallanna, S.K., et al., *Inhibition of Anatid Herpes Virus-1 replication by small interfering RNAs in cell culture system.* Virus Res, 2006. **115**(2): p. 192-7.
81. Sah, D.W., *Therapeutic potential of RNA interference for neurological disorders.* Life Sci, 2006. **79**(19): p. 1773-80.
82. Diamond, P.F., *Making Sense of Antisense and Its Rebound Potential*, in *Genetic Engineering & Biotechnology News*. 2009.
83. Lane, L., *Antisense and Sensibility in RNA Therapeutics*, in *The Scientist*. 2005, LabX Media Group.
84. Pushpendra, S., P. Arvind, and B. Anil, *Nucleic Acids as Therapeutics*, in *From Nucleic Acids Sequences to Molecular Medicine*, V.A. Erdmann and J. Barciszewski, Editors. 2012, Springer-Verlag: Berlin. p. 19-45.
85. Ellington, A.D. and J.W. Szostak, *In vitro selection of RNA molecules that bind specific ligands.* Nature, 1990. **346**(6287): p. 818-22.
86. Irvine, D., C. Tuerk, and L. Gold, *SELEXION. Systematic evolution of ligands by exponential enrichment with integrated optimization by non-linear analysis.* J Mol Biol, 1991. **222**(3): p. 739-61.
87. Ng, E.W., et al., *Pegaptanib, a targeted anti-VEGF aptamer for ocular vascular disease.* Nat Rev Drug Discov, 2006. **5**(2): p. 123-32.

88. Di Giusto, D.A. and G.C. King, *Construction, stability, and activity of multivalent circular anticoagulant aptamers.* Journal of Biological Chemistry, 2004. **279**(45): p. 46483-9.
89. Lara, A.R. and O.T. Ramirez, *Plasmid DNA production for therapeutic applications.* Methods Mol Biol, 2012. **824**: p. 271-303.
90. Sinha, N.D., et al., *Polymer support oligonucleotide synthesis XVIII: use of beta-cyanoethyl-N,N-dialkylamino-/N-morpholino phosphoramidite of deoxynucleosides for the synthesis of DNA fragments simplifying deprotection and isolation of the final product.* Nucleic Acids Research, 1984. **12**(11): p. 4539-57.
91. *Oligo Manufacturing Puts Emphasis on RNA*, in *Genetic Engineering & Biotechnology News*. 2005, Mary Ann Liebert, Inc.
92. Wilkinson, D., *Oligo Factory*, in *The Scientist*. 1999, LabX.
93. Hardee, G.E., *Oral delivery of nucleic acid-based therapeutics.* Ther Deliv, 2012. **3**(2): p. 143-5.
94. Perry, C.M. and J.A. Balfour, *Fomivirsen.* Drugs, 1999. **57**(3): p. 375-80; discussion 381.
95. Rossi, J.J., *RNAi therapeutics: SNALPing siRNAs in vivo.* Gene Therapy, 2006. **13**(7): p. 583-4.
96. Bernhard, B. and J. Kohler, *Drugs to treat macular degeneration vary widely in price*, in *St. Louis Post-Dispatch*. 2010: St. Louis, MO.
97. Glaser, V., *Improving Yields in Oligo Maunfacturing*, in *Genetic Engineering & Biotechnology News*. 2007.
98. Wang, X., D. Gou, and S.Y. Xu, *Polymerase-endonuclease amplification reaction (PEAR) for large-scale enzymatic production of antisense oligonucleotides.* Plos One, 2010. **5**(1): p. e8430.
99. Marshall, E., *Gene therapy death prompts review of adenovirus vector.* Science, 1999. **286**(5448): p. 2244-5.
100. Thomas, C.E., A. Ehrhardt, and M.A. Kay, *Progress and problems with the use of viral vectors for gene therapy.* Nat Rev Genet, 2003. **4**(5): p. 346-58.
101. Edelstein, M.L., M.R. Abedi, and J. Wixon, *Gene therapy clinical trials worldwide to 2007--an update.* Journal of Gene Medicine, 2007. **9**(10): p. 833-42.
102. Remaut, K., et al., *Influence of plasmid DNA topology on the transfection properties of DOTAP/DOPE lipoplexes.* Journal of Controlled Release, 2006. **115**(3): p. 335-43.
103. Adamczyk, Z., et al., *Characterization of poly(ethylene imine) layers on mica by the streaming potential and particle deposition methods.* Journal of Colloid and Interface Science, 2007. **313**(1): p. 86-96.
104. Goodsell, D. *Adenovirus*. Molecule of the Month 2010 [cited 2013 May 1]; Available from: http://www.rcsb.org/pdb/101/motm.do?momID=132.
105. Zinchenko, A.A. and N. Chen, *Compaction of DNA on nanoscale three-dimensional templates.* Journal of Physics-Condensed Matter, 2006. **18**(28): p. R453-R480.
106. Felgner, P.L., et al., *Lipofection: a highly efficient, lipid-mediated DNA-transfection procedure.* Proc Natl Acad Sci U S A, 1987. **84**(21): p. 7413-7.
107. Al-Dosari, M.S. and X. Gao, *Nonviral Gene Delivery: Principle, Limitations, and Recent Progress.* Aaps Journal, 2009. **11**(4): p. 671-681.
108. Luo, D. and W.M. Saltzman, *Synthetic DNA delivery systems.* Nature Biotechnology, 2000. **18**(1): p. 33-37.
109. De Smedt, S.C., J. Demeester, and W.E. Hennink, *Cationic polymer based gene delivery systems.* Pharmaceutical Research, 2000. **17**(2): p. 113-126.
110. Wong, T.K. and E. Neumann, *Electric-Field Mediated Gene-Transfer.* Biochemical and Biophysical Research Communications, 1982. **107**(2): p. 584-587.
111. Vijayanathan, V., T. Thomas, and T.J. Thomas, *DNA nanoparticles and development of DNA delivery vehicles for gene therapy.* Biochemistry, 2002. **41**(48): p. 14085-14094.

112. Curiel, D.T. and J.T. Douglas, eds. *Vector Targeting for Therapeutic Gene Delivery*. 2003, John Wiley & Sons, Inc.
113. Murphy, R.F., S. Powers, and C.R. Cantor, *Endosome pH measured in single cells by dual fluorescence flow cytometry: rapid acidification of insulin to pH 6.* J Cell Biol, 1984. **98**(5): p. 1757-62.
114. Cho, Y.W., J.D. Kim, and K. Park, *Polycation gene delivery systems: escape from endosomes to cytosol.* J Pharm Pharmacol, 2003. **55**(6): p. 721-34.
115. Glover, D.J., et al., *The efficiency of nuclear plasmid DNA delivery is a critical determinant of transgene expression at the single cell level.* Journal of Gene Medicine, 2010. **12**(1): p. 77-85.
116. Akira, S. and K. Takeda, *Toll-like receptor signalling.* Nat Rev Immunol, 2004. **4**(7): p. 499-511.
117. Barton, G.M., J.C. Kagan, and R. Medzhitov, *Intracellular localization of Toll-like receptor 9 prevents recognition of self DNA but facilitates access to viral DNA.* Nat Immunol, 2006. **7**(1): p. 49-56.
118. Zhao, H., et al., *Contribution of Toll-like receptor 9 signaling to the acute inflammatory response to nonviral vectors.* Molecular Therapy, 2004. **9**(2): p. 241-8.
119. Grigsby, C.L. and K.W. Leong, *Balancing protection and release of DNA: tools to address a bottleneck of non-viral gene delivery.* Journal of the Royal Society Interface, 2010. **7**: p. S67-S82.
120. Wiewrodt, R., et al., *Size-dependent intracellular immunotargeting of therapeutic cargoes into endothelial cells.* Blood, 2002. **99**(3): p. 912-22.
121. Volcke, C., et al., *Influence of DNA condensation state on transfection efficiency in DNA/polymer complexes: An AFM and DLS comparative study.* Journal of Biotechnology, 2006. **125**(1): p. 11-21.
122. Prabha, S., et al., *Size-dependency of nanoparticle-mediated gene transfection: studies with fractionated nanoparticles.* Int J Pharm, 2002. **244**(1-2): p. 105-15.
123. Ogris, M., et al., *The size of DNA/transferrin-PEI complexes is an important factor for gene expression in cultured cells.* Gene Therapy, 1998. **5**(10): p. 1425-33.
124. Meyer, M., et al., *Pharmacokinetics of Viral and Non-Viral Gene Delivery Vectors*, in *Pharmacokinetics and Pharmacodynamics of Biotech Drugs: Principles and Case Studies*, B. Meibohm, Editor. 2006, WILEY-VCH Verlag GmbH & Co. KGaA: WEinheim. p. 121-144.
125. Zimmermann, T.S., et al., *RNAi-mediated gene silencing in non-human primates.* Nature, 2006. **441**(7089): p. 111-4.
126. Guillem, V.M. and S.F. Aliño, *Transfection pathways of nonspecific and targeted PEI-polyplexes.* Gene Therapy and Molecular Biology, 2004. **8**: p. 369-384.
127. Shekunov, B.Y., et al., *Particle size analysis in pharmaceutics: principles, methods and applications.* Pharm Res, 2007. **24**(2): p. 203-27.
128. Van Holde, K.E., W.C. Johnson, and P.S. Ho, *Principles of physical biochemistry*. Physical biochemistry ed. 1998, Upper Saddle River, N.J.: Prentice Hall. xii, 657 p.
129. Larson, J.W., et al., *Single DNA molecule stretching in sudden mixed shear and elongational microflows.* Lab on a Chip, 2006. **6**(9): p. 1187-1199.
130. Shrewsbury, P.J., S.J. Muller, and D. Liepmann, *Effect of Flow on Complex Biological Macromolecules in Microfluidic Devices.* Biomedical Microdevices, 2001. **3**(3): p. 225-238.
131. Narayana, N. and M.A. Weiss, *Crystallographic analysis of a sex-specific enhancer element: sequence-dependent DNA structure, hydration, and dynamics.* J Mol Biol, 2009. **385**(2): p. 469-90.
132. Watson, J.D. and F.H. Crick, *The structure of DNA.* Cold Spring Harb Symp Quant Biol, 1953. **18**: p. 123-31.
133. Vardevanyan, P.O., et al., *The binding of ethidium bromide with DNA: interaction with single- and double-stranded structures.* Exp Mol Med, 2003. **35**(6): p. 527-33.

134. Draper, D.E., *A guide to ions and RNA structure.* RNA, 2004. **10**(3): p. 335-43.
135. Lehninger, A.L., D.L. Nelson, and M.M. Cox, *Lehninger principles of biochemistry*. 5th ed. 2008, New York: W.H. Freeman. 1 v. (various pagings).
136. Savelyev, A., C.K. Materese, and G.A. Papoian, *Is DNA's Rigidity Dominated by Electrostatic or Nonelectrostatic Interactions?* Journal of the American Chemical Society, 2011. **133**(48): p. 19290-19293.
137. Stellwagen, N.C., Y.J. Lu, and B. Weers, *DNA persistence length revisited.* Biophysical Journal, 2002. **82**(1): p. 127a-127a.
138. Baker-Jarvis, J., C.A. Jones, and B. Riddle, *NIST Technical Note 1509: Electrical Properties and Dielectric Relaxation of DNA in Solution*, U.D.o. Commerce, et al., Editors. 1998: Boulder, CO. p. 66.
139. Manning, G.S., *Counterion Binding in Polyelectrolyte Theory.* Quarterly Reviews of Biophysics, 1978. **11**(179): p. 443-449.
140. Ross, P.D. and R.L. Scruggs, *Electrophoresis of DNA .2. Specific Interactions of Univalent and Divalent Cations with DNA.* Biopolymers, 1964. **2**(1): p. 79-89.
141. Aubouy, M., E. Trizac, and L. Bocquet, *Effective charge versus bare charge: an analytical estimate for colloids in the infinite dilution limit.* Journal of Physics a-Mathematical and General, 2003. **36**(22): p. 5835-5840.
142. Fischer, S., A. Naji, and R.R. Netz, *Salt-induced counterion-mobility anomaly in polyelectrolyte electrophoresis.* Phys Rev Lett, 2008. **101**(17): p. 176103.
143. Li, A.Z., et al., *A gel electrophoresis study of the competitive effects of monovalent counterion on the extent of divalent counterions binding to DNA.* Biophysical Journal, 1998. **74**(2 Pt 1): p. 964-73.
144. Manning, G.S., *Limiting Laws and Counterion Condensation in Poly-Electrolyte Solutions .7. Electrophoretic Mobility and Conductance.* Journal of Physical Chemistry, 1981. **85**(11): p. 1506-1515.
145. Stellwagen, E. and N.C. Stellwagen, *Probing the electrostatic shielding of DNA with capillary electrophoresis.* Biophysical Journal, 2003. **84**(3): p. 1855-1866.
146. Stellwagen, N.C., et al., *DNA and buffers: Are there any noninteracting, neutral pH buffers?* Analytical Biochemistry, 2000. **287**(1): p. 167-175.
147. Auffinger, P. and E. Westhof, *Water and ion binding around r(UpA)12 and d(TpA)12 oligomers--comparison with RNA and DNA (CpG)12 duplexes.* J Mol Biol, 2001. **305**(5): p. 1057-72.
148. Auffinger, P. and E. Westhof, *Water and ion binding around RNA and DNA (C,G) oligomers.* J Mol Biol, 2000. **300**(5): p. 1113-31.
149. Yonetani, Y., et al., *Comparison of DNA hydration patterns obtained using two distinct computational methods, molecular dynamics simulation and three-dimensional reference interaction site model theory.* Journal of Chemical Physics, 2008. **128**(18): p. 185102.
150. Boussif, O., et al., *A versatile vector for gene and oligonucleotide transfer into cells in culture and in vivo: polyethylenimine.* Proc Natl Acad Sci U S A, 1995. **92**(16): p. 7297-301.
151. von Harpe, A., et al., *Characterization of commercially available and synthesized polyethylenimines for gene delivery.* Journal of Controlled Release, 2000. **69**(2): p. 309-22.
152. Suh, J., H.J. Paik, and B.K. Hwang, *Ionization of Poly(ethylenimine) and Poly(allylamine) at Various pH's.* Bioorganic Chemistry, 1994. **22**(3): p. 318-327.
153. Akinc, A., et al., *Exploring polyethylenimine-mediated DNA transfection and the proton sponge hypothesis.* Journal of Gene Medicine, 2005. **7**(5): p. 657-63.
154. Moghimi, S.M., et al., *A two-stage poly(ethylenimine)-mediated cytotoxicity: implications for gene transfer/therapy.* Molecular Therapy, 2005. **11**(6): p. 990-5.
155. Lv, H., et al., *Toxicity of cationic lipids and cationic polymers in gene delivery.* Journal of Controlled Release, 2006. **114**(1): p. 100-9.

156. Lungwitz, U., et al., *Polyethylenimine-based non-viral gene delivery systems.* European Journal of Pharmaceutics and Biopharmaceutics, 2005. **60**(2): p. 247-266.
157. Werth, S., et al., *A low molecular weight fraction of polyethylenimine (PEI) displays increased transfection efficiency of DNA and siRNA in fresh or lyophilized complexes.* Journal of Controlled Release, 2006. **112**(2): p. 257-270.
158. Chen, T., et al., *Polyethylenimine-DNA solid particles for gene delivery.* J Drug Target, 2007. **15**(10): p. 714-20.
159. Pun, S.H., et al., *Cyclodextrin-modified polyethylenimine polymers for gene delivery.* Bioconjug Chem, 2004. **15**(4): p. 831-40.
160. Urban-Klein, B., et al., *RNAi-mediated gene-targeting through systemic application of polyethylenimine (PEI)-complexed siRNA in vivo.* Gene Therapy, 2005. **12**(5): p. 461-466.
161. Bloomfield, V.A., *Condensation of DNA by Multivalent Cations: Considerations on Mechanism.* Biopolymers, 1991. **31**(13): p. 1471-1481.
162. Bloomfield, V.A., *DNA condensation by multivalent cations.* Biopolymers, 1997. **44**(3): p. 269-82.
163. Park, S.Y., D. Harries, and W.M. Gelbart, *Topological defects and the optimum size of DNA condensates.* Biophysical Journal, 1998. **75**(2): p. 714-720.
164. Sharma, V.K., M. Thomas, and A.M. Klibanov, *Mechanistic studies on aggregation of polyethylenimine-DNA complexes and its prevention.* Biotechnology and Bioengineering, 2005. **90**(5): p. 614-620.
165. Allison, S.A., J.C. Herr, and J.M. Schurr, *Structure of viral phi 29 DNA condensed by simple triamines: a light-scattering and electron-microscopy study.* Biopolymers, 1981. **20**(3): p. 469-88.
166. Braun, C.S., et al., *The structure of DNA within cationic lipid/DNA complexes.* Biophysical Journal, 2003. **84**(2): p. 1114-1123.
167. Conwell, C.C. and N.V. Hud, *Evidence that both kinetic and thermodynamic factors govern DNA toroid dimensions: Effects of magnesium(II) on DNA condensation by hexammine cobalt(III).* Biochemistry, 2004. **43**(18): p. 5380-5387.
168. Conwell, C.C., I.D. Vilfan, and N.V. Hud, *Controlling the diameter and thickness of toroidal DNA condensates.* Biophysical Journal, 2003. **84**(2): p. 181a-181a.
169. Conwell, C.C., I.D. Vilfan, and N.V. Hud, *Controlling the size of nanoscale toroidal DNA condensates with static curvature and ionic strength.* Proceedings of the National Academy of Sciences of the United States of America, 2003. **100**(16): p. 9296-9301.
170. Hud, N.V., C. Conwell, and I. Vilfan, *Controlling the size of nanoscale toroidal DNA condensates with static curvature and ionic strength.* Abstracts of Papers of the American Chemical Society, 2003. **226**: p. U337-U337.
171. Boeckle, S., et al., *Purification of polyethylenimine polyplexes highlights the role of free polycations in gene transfer.* Journal of Gene Medicine, 2004. **6**(10): p. 1102-1111.
172. Monteserin, M., et al., *How to change the aggregation in the DNA/surfactant/cationic conjugated polyelectrolyte system through the order of component addition: anionic versus neutral surfactants.* Langmuir, 2010. **26**(14): p. 11705-14.
173. Martin, A.L., et al., *Observation of DNA-polymer condensate formation in real time at a molecular level.* Febs Letters, 2000. **480**(2-3): p. 106-112.
174. Moret, I., et al., *Stability of PEI-DNA and DOTAP-DNA complexes: effect of alkaline pH, heparin and serum.* Journal of Controlled Release, 2001. **76**(1-2): p. 169-81.
175. Lai, E. and J.H. van Zanten, *Monitoring DNA/poly-L-lysine polyplex formation with time-resolved multiangle laser light scattering.* Biophysical Journal, 2001. **80**(2): p. 864-73.
176. Lai, E. and J.H. van Zanten, *Real time monitoring of lipoplex molar mass, size and density.* Journal of Controlled Release, 2002. **82**(1): p. 149-58.

177. Stukan, M.R., et al., *Stability of toroid and rodlike globular structures of a single stiff-chain macromolecule for different bending potentials.* Physical Review E, 2006. **73**(5): p. -.
178. Vilfan, I.D., et al., *Time study of DNA condensate morphology: implications regarding the nucleation, growth, and equilibrium populations of toroids and rods.* Biochemistry, 2006. **45**(26): p. 8174-83.
179. Hagan, M.F., O.M. Elrad, and R.L. Jack, *Mechanisms of kinetic trapping in self-assembly and phase transformation.* Journal of Chemical Physics, 2011. **135**(10).
180. Johnson, B.K. and R.K. Prud'homme, *Mechanism for rapid self-assembly of block copolymer nanoparticles.* Physical Review Letters, 2003. **91**(11).
181. Lim, I.I.S., et al., *Kinetic and thermodynamic assessments of the mediator-template assembly of nanoparticles.* Journal of Physical Chemistry B, 2005. **109**(7): p. 2578-2583.
182. Mehta, A. (2011) *Thermodynamoc Product vs Kinetic Product -- with example of enolate formation of 2-methylcyclohexanone*.
183. Zhang, L.F. and A. Eisenberg, *Thermodynamic vs kinetic aspects in the formation and morphological transitions of crew-cut aggregates produced by self-assembly of polystyrene-b-poly(acrylic acid) block copolymers in dilute solution.* Macromolecules, 1999. **32**(7): p. 2239-2249.
184. Hud, N.V. and I.D. Vilfan, *Toroidal DNA condensates: unraveling the fine structure and the role of nucleation in determining size.* Annu Rev Biophys Biomol Struct, 2005. **34**: p. 295-318.
185. Zhao, Q.Q., et al., *N/P ratio significantly influences the transfection efficiency and cytotoxicity of a polyethylenimine/chitosan/DNA complex.* Biol Pharm Bull, 2009. **32**(4): p. 706-10.
186. Hou, S., et al., *Formation and structure of PEI/DNA complexes: quantitative analysis.* Soft Matter, 2011. **7**(15): p. 6967-6972.
187. Mann, A., R. Richa, and M. Ganguli, *DNA condensation by poly-L-lysine at the single molecule level: role of DNA concentration and polymer length.* Journal of Controlled Release, 2008. **125**(3): p. 252-62.
188. Cubillas, P. and M.W. Anderson, *Synthesis Mechanism: Crystal Growth and Nucleation*, in *Zeolites and Catalysis, Synthesis, Reactions and Applications.* , J. Cejka, A. Corma, and S. Jones, Editors. 2010, Wiley-VCH Verlag GmbH & Co. KGaA: Weinheim.
189. Stevens, M.J., *Simple simulations of DNA condensation.* Biophysical Journal, 2001. **80**(1): p. 130-139.
190. Clamme, J.P., J. Azoulay, and Y. Mely, *Monitoring of the formation and dissociation of polyethylenimine/DNA complexes by two photon fluorescence correlation spectroscopy.* Biophysical Journal, 2003. **84**(3): p. 1960-1968.
191. He, S.Q., P.G. Arscott, and V.A. Bloomfield, *Condensation of DNA by multivalent cations: Experiment studies of condensation kinetics.* Biopolymers, 2000. **53**(4): p. 329-341.
192. Tecle, M., M. Preuss, and A.D. Miller, *Kinetic study of DNA condensation by cationic peptides used in nonviral gene therapy: Analogy of DNA condensation to protein folding.* Biochemistry, 2003. **42**(35): p. 10343-10347.
193. Elimelech, M., et al., *Particle Deposition & Aggregation*. Colloid and Surface Engineering Series. 1995, Woburn, MA: Butterworth-Henemann.
194. Bird, R.B., W.E. Stewart, and E.N. Lightfoot, *Transport Phenomena*. 2nd edition ed. 2002, New York, NY: John Wiley & Sons, Inc.
195. Aris, R., *On the Dispersion of a Solute in a Fluid Flowing through a Tube.* Proceedings of the Royal Society of London Series a-Mathematical and Physical Sciences, 1956. **235**(1200): p. 67-77.
196. Kamholz, A.E. and P. Yager, *Molecular diffusive scaling laws in pressure-driven microfluidic channels: deviation from one-dimensional Einstein approximations.* Sensors and Actuators B-Chemical, 2002. **82**(1): p. 117-121.

197. Jahn, A., et al., *Microfluidic directed formation of liposomes of controlled size.* Langmuir, 2007. **23**(11): p. 6289-6293.
198. Frenz, L., et al., *Droplet-based microreactors for the synthesis of magnetic iron oxide nanoparticles.* Angewandte Chemie-International Edition, 2008. **47**(36): p. 6817-6820.
199. Khan, S.A., et al., *Microfluidic synthesis of colloidal silica.* Langmuir, 2004. **20**(20): p. 8604-8611.
200. Lee, W.B., et al., *Biomedical microdevices synthesis of iron oxide nanoparticles using a microfluidic system.* Biomedical Microdevices, 2009. **11**(1): p. 161-171.
201. Marre, S. and K.F. Jensen, *Synthesis of micro and nanostructures in microfluidic systems.* Chemical Society Reviews, 2010. **39**(3): p. 1183-1202.
202. Sounart, T.L., et al., *Spatially-resolved analysis of nanoparticle nucleation and growth in a microfluidic reactor.* Lab on a Chip, 2007. **7**(7): p. 908-915.
203. Chen, D., et al., *Rapid discovery of potent siRNA-containing lipid nanoparticles enabled by controlled microfluidic formulation.* Journal of the American Chemical Society, 2012. **134**(16): p. 6948-51.
204. Debus, H., M. Beck-Broichsitter, and T. Kissel, *Optimized preparation of pDNA/poly(ethylene imine) polyplexes using a microfluidic system.* Lab on a Chip, 2012. **12**(14): p. 2498-2506.
205. Endres, T., et al., *Optimising the self-assembly of siRNA loaded PEG-PCL-lPEI nano-carriers employing different preparation techniques.* Journal of Controlled Release, 2012. **160**(3): p. 583-91.
206. Ho, Y.P., et al., *Tuning physical properties of nanocomplexes through microfluidics-assisted confinement.* Nano Lett, 2011. **11**(5): p. 2178-82.
207. Ho, Y.-P., C. Grigsby, and K.W. Leong. *Unexpected Propertirs of Polymeris DNA-Nanocomplexes Synthesized in Picoliter Droplets*. in *6ths IEEE Intersational Conference on Nano/Microengineered and Molecular Systems*. 2011. Kaohsiung, Taiwan: IEEE.
208. Koh, C.G., et al., *Delivery of Polyethylenimine/DNA Complexes Assembled in a Microfluidics Device.* Molecular Pharmaceutics, 2009. **6**(5): p. 1333-1342.
209. Yu, B., et al., *Microfluidic Assembly of Lipid-based Oligonucleotide Nanoparticles.* Anticancer Research, 2011. **31**(3): p. 771-776.
210. Beebe, D.J., G.A. Mensing, and G.M. Walker, *Physics and applications of microfluidics in biology.* Annu Rev Biomed Eng, 2002. **4**: p. 261-86.
211. McDonald, J.C., et al., *Fabrication of microfluidic systems in poly(dimethylsiloxane).* Electrophoresis, 2000. **21**(1): p. 27-40.
212. Arkles, B., *Hydrophobicity, Hydrophilicity, and Silane Surface Modification*. 2011, Gelest, Inc.: Morrisville, PA.
213. Dou, Y.H., et al., *Separation of proteins on surface-modified poly(dimethylsiloxane) microfluidic devices.* Electrophoresis, 2004. **25**(17): p. 3024-3031.
214. Esso, C., *Modifying Polydimethylsiloxane (PDMS) surfaces*. 2007, Maladalen University: Uppsala, Sweden. p. 1-33.
215. Lee, H., et al., *Mussel-inspired surface chemistry for multifunctional coatings.* Science, 2007. **318**(5849): p. 426-430.
216. Seo, J. and L.P. Lee, *Effects on wettability by surfactant accumulation/depletion in bulk polydimethylsiloxane (PDMS).* Sensors and Actuators B-Chemical, 2006. **119**(1): p. 192-198.
217. Sui, G., et al., *Solution-phase surface modification in intact poly(dimethylsiloxane) microfluidic channels.* Analytical Chemistry, 2006. **78**(15): p. 5543-51.
218. Vickers, J.A., M.M. Caulum, and C.S. Henry, *Generation of hydrophilic poly(dimethylsiloxane) for high-performance microchip electrophoresis.* Analytical Chemistry, 2006. **78**(21): p. 7446-7452.
219. Wong, I. and C.M. Ho, *Surface molecular property modifications for poly(dimethylsiloxane) (PDMS) based microfluidic devices.* Microfluidics and Nanofluidics, 2009. **7**(3): p. 291-306.

220. Zhou, J., A.V. Ellis, and N.H. Voelcker, *Recent developments in PDMS surface modification for microfluidic devices.* Electrophoresis, 2010. **31**(1): p. 2-16.
221. Chau, K.N., et al., *Dependence of the quality of adhesion between poly(dimethylsiloxane) and glass surfaces on the composition of the oxidizing plasma.* Microfluidics and Nanofluidics, 2011. **10**(4): p. 907-917.
222. Kim, J., M.K. Chaudhury, and M.J. Owen, *Hydrophobicity loss and recovery of silicone HV insulation.* Ieee Transactions on Dielectrics and Electrical Insulation, 1999. **6**(5): p. 695-702.
223. Kakuta, M., F.G. Bessoth, and A. Manz, *Microfabricated devices for fluid mixing and their application for chemical synthesis.* Chem Rec, 2001. **1**(5): p. 395-405.
224. Niu, X.Z. and Y.K. Lee, *Efficient spatial-temporal chaotic mixing in microchannels.* Journal of Micromechanics and Microengineering, 2003. **13**(3): p. 454-462.
225. Yang, Z., et al., *Active micromixer for microfluidic systems using lead-zirconate-titanate(PZT)-generated ultrasonic vibration.* Electrophoresis, 2000. **21**(1): p. 116-119.
226. Hardt, S., et al., *Passive micromixers for applications in the microreactor and mu TAS fields.* Microfluidics and Nanofluidics, 2005. **1**(2): p. 108-118.
227. Hardt, S., H. Pennemann, and F. Schonfeld, *Theoretical and experimental characterization of a low-Reynolds number split-and-recombine mixer.* Microfluidics and Nanofluidics, 2006. **2**(3): p. 237-248.
228. Howell, P.B., et al., *Design and evaluation of a Dean vortex-based micromixer.* Lab on a Chip, 2004. **4**(6): p. 663-669.
229. Kim, D.S., et al., *A barrier embedded Kenics micromixer.* Journal of Micromechanics and Microengineering, 2004. **14**(10): p. 1294-1301.
230. Schonfeld, F., V. Hessel, and C. Hofmann, *An optimised split-and-recombine micro-mixer with uniform 'chaotic' mixing.* Lab on a Chip, 2004. **4**(1): p. 65-69.
231. Song, H., D.L. Chen, and R.F. Ismagilov, *Reactions in droplets in microfluidic channels.* Angew Chem Int Ed Engl, 2006. **45**(44): p. 7336-56.
232. *"chaos"*, in *The American Heritage Science Dictionary*, Houghton Mifflin Company.
233. Franjione, J.G. and J.M. Ottino, *Stretching in Duct Flows.* Physics of Fluids a-Fluid Dynamics, 1991. **3**(11): p. 2819-2821.
234. Ottino, J.M. and S. Wiggins, *Introduction: mixing in microfluidics.* Philosophical Transactions of the Royal Society of London Series a-Mathematical Physical and Engineering Sciences, 2004. **362**(1818): p. 923-935.
235. Aref, H., *The development of chaotic advection.* Physics of Fluids, 2002. **14**(4): p. 1315-1325.
236. Ottino, J.M. and S. Wiggins, *Applied physics - Designing optimal micromixers.* Science, 2004. **305**(5683): p. 485-486.
237. Stremler, M.A., F.R. Haselton, and H. Aref, *Designing for chaos: applications of chaotic advection at the microscale.* Philosophical Transactions of the Royal Society a-Mathematical Physical and Engineering Sciences, 2004. **362**(1818): p. 1019-1036.
238. Wiggins, S. and J.M. Ottino, *Foundations of chaotic mixing.* Philosophical Transactions of the Royal Society of London Series a-Mathematical Physical and Engineering Sciences, 2004. **362**(1818): p. 937-970.
239. Hessel, V., H. Lowe, and F. Schonfeld, *Micromixers - a review on passive and active mixing principles.* Chemical Engineering Science, 2005. **60**(8-9): p. 2479-2501.
240. MacInnes, J.M., A. Vikhansky, and R.W.K. Allen, *Numerical characterisation of folding flow microchannel mixers.* Chemical Engineering Science, 2007. **62**(10): p. 2718-2727.
241. Stroock, A.D., et al., *Chaotic mixer for microchannels.* Science, 2002. **295**(5555): p. 647-651.
242. Gambin, Y., et al., *Ultrafast microfluidic mixer with three-dimensional flow focusing for studies of biochemical kinetics.* Lab on a Chip, 2010. **10**(5): p. 598-609.
243. Golden, J.P., et al., *Multi-wavelength microflow cytometer using groove-generated sheath flow.* Lab on a Chip, 2009. **9**(13): p. 1942-1950.

244. Yu, B., et al., *Microfluidic assembly of lipid-based oligonucleotide nanoparticles.* Anticancer Research, 2011. **31**(3): p. 771-6.
245. Besteman, K., et al., *Influence of charged surfaces on the morphology of DNA condensed with multivalent ions.* Biopolymers, 2007. **87**(2-3): p. 141-148.
246. Sitterberg, J., et al., *Utilising atomic force microscopy for the characterisation of nanoscale drug delivery systems.* European Journal of Pharmaceutics and Biopharmaceutics, 2010. **74**(1): p. 2-13.
247. Berne, B.J. and R. Pecora, *Dynamic light scattering: with applications to chemistry, biology, and physics*. 2000, Mineola, NY: Dover Publications, Inc.
248. Braun, C.S., et al., *A stopped-flow kinetic study of the assembly of nonviral gene delivery complexes.* Biophysical Journal, 2005. **88**(6): p. 4146-4158.
249. LePecq, J.B. and C. Paoletti, *A fluorescent complex between ethidium bromide and nucleic acids. Physical-chemical characterization.* J Mol Biol, 1967. **27**(1): p. 87-106.
250. Wiethoff, C.M., et al., *A fluorescence study of the structure and accessibility of plasmid DNA condensed with cationic gene delivery vehicles.* Journal of Pharmaceutical Sciences, 2003. **92**(6): p. 1272-1285.
251. Mott, D.R., et al., *Toolbox for the design of optimized microfluidic components.* Lab on a Chip, 2006. **6**(4): p. 540-549.
252. Stroock, A.D. and G.J. McGraw, *Investigation of the staggered herringbone mixer with a simple analytical model.* Philosophical Transactions of the Royal Society of London Series a-Mathematical Physical and Engineering Sciences, 2004. **362**(1818): p. 971-986.
253. Wang, H.Z., et al., *Numerical investigation of mixing in microchannels with patterned grooves.* Journal of Micromechanics and Microengineering, 2003. **13**(6): p. 801-808.
254. Xia, H.M., et al., *Numerical and experimental observation of chaotic mixing in microfluidic mixer.* Journal of Visualization, 2005. **8**(4): p. 291-291.
255. Ulasov, A.V., et al., *Properties of PEI-based Polyplex Nanoparticles That Correlate With Their Transfection Efficacy.* Molecular Therapy, 2011. **19**(1): p. 103-112.
256. Lengsfeld, C.S. and T.J. Anchordoquy, *Shear-induced degradation of plasmid DNA.* Journal of Pharmaceutical Sciences, 2002. **91**(7): p. 1581-1589.
257. Hassell, D.G. and W.B. Zimmerman, *Investigation of the convective motion through a staggered herringbone micromixer at low Reynolds number flow.* Chemical Engineering Science, 2006. **61**(9): p. 2977-2985.
258. Howell, P.B., et al., *A microfluidic mixer with grooves placed on the top and bottom of the channel.* Lab on a Chip, 2005. **5**(5): p. 524-530.
259. Johnson, T.J. and L.E. Locascio, *Characterization and optimization of slanted well designs for microfluidic mixing under electroosmotic flow.* Lab on a Chip, 2002. **2**(3): p. 135-140.
260. Sato, H., et al., *PDMS microchannels with slanted grooves embedded in three walls to realize efficient spiral flow.* Sensors and Actuators a-Physical, 2005. **119**(2): p. 365-371.
261. Williams, M.S., K.J. Longmuir, and P. Yager, *A practical guide to the staggered herringbone mixer.* Lab on a Chip, 2008. **8**(7): p. 1121-1129.
262. Yang, J.T., K.J. Huang, and Y.C. Lin, *Geometric effects on fluid mixing in passive grooved micromixers.* Lab on a Chip, 2005. **5**(10): p. 1140-1147.
263. Lee, H.Y. and J. Voldman, *Optimizing micromixer design for enhancing dielectrophoretic microconcentrator performance.* Analytical Chemistry, 2007. **79**(5): p. 1833-9.
264. Aubin, J., D.F. Fletcher, and C. Xuereb, *Design of micromixers using CFD modelling.* Chemical Engineering Science, 2005. **60**(8-9): p. 2503-2516.
265. Scheuerman, T.R., A.K. Camper, and M.A. Hamilton, *Effects of substratum topography on bacterial adhesion.* Journal of Colloid and Interface Science, 1998. **208**(1): p. 23-33.
266. Rusconi, R., et al., *Secondary flow as a mechanism for the formation of biofilm streamers.* Biophysical Journal, 2011. **100**(6): p. 1392-9.

267. Kursa, M., et al., *Novel shielded transferrin-polyethylene glycol-polyethylenimine/DNA complexes for systemic tumor-targeted gene transfer.* Bioconjug Chem, 2003. **14**(1): p. 222-31.
268. Burke, R.S. and S.H. Pun, *Extracellular barriers to in Vivo PEI and PEGylated PEI polyplex-mediated gene delivery to the liver.* Bioconjug Chem, 2008. **19**(3): p. 693-704.
269. Edel, J.B., et al., *Microfluidic routes to the controlled production of nanoparticles.* Chem Commun (Camb), 2002(10): p. 1136-7.
270. Pettitt, M.E. and J.R. Lead, *Minimum physicochemical characterisation requirements for nanomaterial regulation.* Environ Int, 2013. **52**: p. 41-50.
271. Richman, E.K. and J.E. Hutchison, *The nanomaterial characterization bottleneck.* Acs Nano, 2009. **3**(9): p. 2441-6.
272. Stefaniak, A.B., et al., *Nanoscale reference materials for environmental, health and safety measurements: needs, gaps and opportunities.* Nanotoxicology, 2012.
273. Troiber, C., et al., *Comparison of four different particle sizing methods for siRNA polyplex characterization.* European Journal of Pharmaceutics and Biopharmaceutics, 2012.
274. Montes-Burgos, I., et al., *Characterisation of nanoparticle size and state prior to nanotoxicological studies.* J Nanopart Res, 2010. **12**: p. 47-53.
275. Thangawng, A.L., et al., *A simple sheath-flow microfluidic device for micro/nanomanufacturing: fabrication of hydrodynamically shaped polymer fibers.* Lab on a Chip, 2009. **9**(21): p. 3126-3130.
276. Hashemi, N., et al., *Dynamic reversibility of hydrodynamic focusing for recycling sheath fluid.* Lab on a Chip, 2010.
277. Howell, P.B., Jr., et al., *Two simple and rugged designs for creating microfluidic sheath flow.* Lab on a Chip, 2008. **8**(7): p. 1097-103.
278. Neher, E., *Correction for Liquid Junction Potentials in Patch Clamp Experiments.* Methods in Enzymology, 1992. **207**: p. 123-131.
279. Munson, M.S., C.R. Cabrera, and P. Yager, *Passive electrophoresis in microchannels using liquid junction potentials.* Electrophoresis, 2002. **23**(16): p. 2642-2652.
280. Goldman, D.E., *Potential, impedance, and rectification in membranes.* Journal of General Physiology, 1944. **27**(1): p. 37-60.
281. Debye, P. and E. Huckel, *The theory of electrolytes I. The lowering of the freezing point and related occurrences.* Physikalische Zeitschrift, 1923. **24**: p. 185-206.
282. Gouy, *On the constitution of the electric charge at the surface of an electrolyte.* Comptes Rendus Hebdomadaires Des Seances De L Academie Des Sciences, 1909. **149**: p. 654-657.
283. AlvarezRamirez, J., R. Martinez, and E. DiazHerrera, *Solution of the Poisson-Boltzmann equation through the use of pseudo-dynamic simulation method.* Chemical Physics Letters, 1997. **266**(3-4): p. 375-382.
284. Bowen, R.W. and A.O. Sharif, *Adaptive finite-element solution of the nonlinear Poisson-Boltzmann equation: A charged spherical particle at various distances from a charged cylindrical pore in a charged planar surface.* Journal of Colloid and Interface Science, 1997. **187**(2): p. 363-374.
285. Cortis, C.M. and R.A. Friesner, *Numerical solution of the Poisson-Boltzmann equation using tetrahedral finite-element meshes.* Journal of Computational Chemistry, 1997. **18**(13): p. 1591-1608.
286. Holst, M., N. Baker, and F. Wang, *Adaptive multilevel finite element solution of the Poisson-Boltzmann equation I. Algorithms and examples.* Journal of Computational Chemistry, 2000. **21**(15): p. 1319-1342.
287. Holst, M., et al., *Protein Electrostatics - Rapid Multigrid-Based Newton Algorithm for Solution of the Full Nonlinear Poisson-Boltzmann Equation.* Journal of Biomolecular Structure & Dynamics, 1994. **11**(6): p. 1437-1445.

288. Holst, M.J. and F. Saied, *Numerical-Solution of the Nonlinear Poisson-Boltzmann Equation - Developing More Robust and Efficient Methods.* Journal of Computational Chemistry, 1995. **16**(3): p. 337-364.
289. Huber, A., *An Algebraic Approach for Solving Time-Dependent Potentials.* Match-Communications in Mathematical and in Computer Chemistry, 2011. **66**(1): p. 205-217.
290. Hwang, C.O. and M. Mascagni, *Efficient modified "walk on spheres" algorithm for the linearized Poisson-Bolzmann equation.* Applied Physics Letters, 2001. **78**(6): p. 787-789.
291. Jasielec, J.J., et al., *Computer simulations of electrodiffusion problems based on Nernst-Planck and Poisson equations.* Computational Materials Science, 2012. **63**: p. 75-90.
292. Kato, M., *Numerical analysis of the Nernst-Planck-Poisson system.* Journal of Theoretical Biology, 1995. **177**(3): p. 299-304.
293. Koehl, P., *Electrostatics calculations: latest methodological advances.* Current Opinion in Structural Biology, 2006. **16**(2): p. 142-151.
294. Lindgren, E.R., R.R. Rao, and B. Finlayson. *Numerical Simulation of Electrokinetic Phenomena*. in *Emerging Technologies in Hazardous Waste Management V (ACS Symposium Series)*. 1993. Atlanta, GA: American Chemical Society.
295. Lu, B.Z., et al., *AFMPB: An adaptive fast multipole, Poisson-Boltzmann solver for calculating electrostatics in biomolecular systems.* Computer Physics Communications, 2010. **181**(6): p. 1150-1160.
296. Lu, B.Z., et al., *Electrodiffusion: A continuum modeling framework for biomolecular systems with realistic spatiotemporal resolution.* Journal of Chemical Physics, 2007. **127**(13).
297. Luty, B.A., M.E. Davis, and J.A. Mccammon, *Solving the Finite-Difference Nonlinear Poisson-Boltzmann Equation.* Journal of Computational Chemistry, 1992. **13**(9): p. 1114-1118.
298. Nicholls, A. and B. Honig, *A Rapid Finite-Difference Algorithm, Utilizing Successive over-Relaxation to Solve the Poisson-Boltzmann Equation.* Journal of Computational Chemistry, 1991. **12**(4): p. 435-445.
299. Shi, X.W. and P. Koehl, *The geometry behind numerical solvers of the Poisson-Boltzmann equation.* Communications in Computational Physics, 2008. **3**(5): p. 1032-1050.
300. Xiang, Z.X., Y.Y. Shi, and Y.W. Xu, *Solving the Finite-Difference, Nonlinear, Poisson-Boltzmann Equation under a Linear-Approach.* Journal of Computational Chemistry, 1995. **16**(2): p. 200-206.
301. Zhang, J.F., et al., *A simple and practical approach to implement the general Poisson-Boltzmann equation of symmetric and asymmetric electrolytes for electrical double layer interactions.* Colloids and Surfaces a-Physicochemical and Engineering Aspects, 2004. **242**(1-3): p. 189-193.
302. Zhou, Z.X., et al., *Finite-difference solution of the Poisson-Boltzmann equation: Complete elimination of self-energy.* Journal of Computational Chemistry, 1996. **17**(11): p. 1344-1351.
303. Feldberg, S.W., *On the dilemma of the use of the electroneutrality constraint in electrochemical calculations.* Electrochemistry Communications, 2000. **2**(7): p. 453-456.
304. Liao, W.C., et al., *Conformation dependence of DNA electrophoretic mobility in a converging channel.* Electrophoresis, 2010. **31**(16): p. 2813-2821.
305. Fixman, M., *Poisson-Boltzmann Equation and Its Application to Polyelectrolytes.* Journal of Chemical Physics, 1979. **70**(11): p. 4995-5005.
306. Ander, P., L. Leunglouie, and F. Silvestri, *Polycations .1. Sodium, Calcium, and Sulfate Ion Diffusion-Coefficients in Aqueous Salt-Solutions Containing Ionene Bromides.* Macromolecules, 1979. **12**(6): p. 1204-1207.
307. Wang, J.H., *Tracer-Diffusion in Liquids .3. The Self-Diffusion of Chloride Ion in Aqueous Sodium Chloride Solutions.* Journal of the American Chemical Society, 1952. **74**(6): p. 1612-1615.

308. Li, W.B., et al., *Accurate Formula Weight Determination in Physically Separated Systems by Diffusion Coefficient-Formula Weight Correlation.* Organometallics, 2010. **29**(6): p. 1309-1311.
309. Kovbasnjuk, O.N., P.M. Bungay, and K.R. Spring, *Diffusion of small solutes in the lateral intercellular spaces of MDCK cell epithelium grown on permeable supports.* Journal of Membrane Biology, 2000. **175**(1): p. 9-16.
310. Kunkel, J.G. *Utilities for estimating the diffusion coefficients of weak electrolytes*. 2000 [cited 2013; Available from: http://www.bio.umass.edu/biology/kunkel/probe/buffers/.
311. Periasamy, N. and A.S. Verkman, *Analysis of fluorophore diffusion by continuous distributions of diffusion coefficients: Application to photobleaching measurements of multicomponent and anomalous diffusion.* Biophysical Journal, 1998. **75**(1): p. 557-567.
312. Stellwagen, N.C., C. Gelfi, and P.G. Righetti, *The free solution mobility of DNA.* Biopolymers, 1997. **42**(6): p. 687-703.
313. Wang, S., et al., *Instantaneous DNA Electrophoretic Mobiliy*, The Ohio State University.
314. Stellwagen, E. and N.C. Stellwagen, *Determining the electrophoretic mobility and translational diffusion coefficients of DNA molecules in free solution.* Electrophoresis, 2002. **23**(16): p. 2794-2803.
315. Dorfman, K.D. and H. Brenner, *Comment on "Taylor dispersion of a solute in a microfluidic channel" [J. Appl. Phys. 89, 4667 (2001)].* Journal of Applied Physics, 2001. **90**(12): p. 6553-6554.